Simulation and Experimental Results of an Absorbent-Enhanced Ammonia Synthesis Reactor

Wenchan Qi

St Cross College

University of Oxford

A thesis submitted for the degree of

Doctor of Philosophy

Department of Engineering Science

Trinity 2020

Declaration

I declare that this thesis is entirely my own work, and except where otherwise stated, describes my own research.

Wenchan Qi,

St Cross College

Dedication

I dedicate this project to God Almighty my creator, my strong pillar, my source of inspiration, wisdom, knowledge and understanding. He has been the source of my strength throughout this program and on His wings only have I soared.

Acknowledgements

I would like to express my sincere gratitude to my supervisor Dr. René Bañares-Alcántara for his guidance, suggestions and encouragement throughout my DPhil student life at University of Oxford. Besides, I dedicate my appreciation to my co-supervisor Professor S. C. Edman Tsang, for his valuable advice on my scientific research and kind help in laboratory work over the last four years.

Secondly, I am very thankful to all the members of the Tsang group, who have provided much collaboration, help and support, in particular to Mr Simson Wu, for his magnificent cooperation in providing data of XRD and STEM characterisation of catalysts. Furthermore, I would like to thank Dr. Jianwei Zheng, Dr. Tugce Ayvali, and Miss Kirsty Purchase for their expert supervision in the laboratory.

I would especially like to thank Ms Wilfride Petnga for all her hard work in proofreading this thesis.

I am deeply grateful to all my family members and friends for their love and trust. Their encouragement helped me through all the difficulties I encountered throughout the past four years.

Last but not least, I would like to praise and thank God, the almighty, who has granted countless blessing, knowledge, and opportunity to me, so that I have been finally able to accomplish the thesis.

Table of Contents

List of Nomenclatures

Symbol	Units	Description
a_k	[-]	Activity of component k
A	[m^2]	Surface area of the absorbent pellet
A_{cat}	[m^2]	Cross sectional area of the catalyst bed
A_{column}	[m^2]	Flank area of the catalyst bed
Abs	[-]	Absorbent bed
c	[mol/m^3]	Concentration in the bulk fluid
$c_{a,j}$	[mol/m^3]	Concentration of ammonia in cell j in the absorbent packed bed
$c_{r,i}$	[mol/m^3]	Concentration of ammonia in cell i in the catalyst packed bed
c_F	[mol/m^3]	Concentration at inlet of absorbent bed
c^*	[mol/m^3]	Concentration of ammonia at equilibrium
Cat	[-]	Catalyst bed
C_f	[J/K]	Volumetric heat capacity of fluid phase
C_{pk}	[J/K]	Heat capacity of component k
C_s	[J/K]	Volumetric heat capacity of solid phase
C_{pre}	[-]	Prescribed matrices
d	[m]	Internal diameter of absorbent bed
D	[m^2/s]	Diffusion coefficient
$D_{k,m}$	[m^2/s]	Mass diffusivity for species k in the mixture

D_L	[m^2/s]	Axial dispersion coefficient
D_e	[m^2/s]	Effective diffusion coefficient
D_{pre}	[-]	Prescribed matrices
E	[J/kg]	Energy
F	[N]	External body force
f_k	[Pa]/[bar]	Fugacity of component k in mixture
F_k	[mol/s]	Flowrate of component k
h	[W/(m^2*K)]	Overall heat transfer coefficient between absorbent particle and ambient fluid
h_e	[J/kg]	Enthalpy of species
h_w	[W/(m^2*K)]	Overall heat transfer coefficient at column wall
H	[g/(atm·m^3)]	Partition coefficient
ΔH	[kJ/mol]	Enthalpy of ammonia absorption
I	[-]	Unit tensor
J	[kg/(m^2s)]	Diffusion flux of species
k^*	[-]	Parameter of Ru catalyst synthesis rate
k_{a1-a3}	[-]	Experimentally determined constants
K	[-]	Absorption equilibrium constant
k_f	[m/s]	Mass transfer coefficient in absorbent bed
k_2	[-]	Reverse reaction rate constant
K_a	[-]	Reaction equilibrium constant

l	[m]	Reactor length
L	[m]	Absorbent bed length
p	[bar]	Pressure
p_a	[bar]	Partial pressure of ammonia
p_h	[bar]	Partial pressure of hydrogen
p_n	[bar]	Partial pressure of nitrogen
p^*	[bar]	Equilibrium pressure of ammonia absorption
p^0	[bar]	Reference pressure (1 bar)
q	[m^3/g]	Absorbate loading per unit mass
$\dot{q}$	[m^3/s]	Volume flow rate in the BCM
$\bar{q}$	[m^3/g]	Volume-average absorbate loading per unit mass
q^*	[m^3/g]	Absorbate loading in equilibrium
r	[m]	Radial coordinate of catalyst/absorbent pellet
R	[J/(mol*K)]	Gas constant
R_s	[m^3/s]	Hypothetical recycle stream amount
R_p	[m]	Radius of absorbent pellet
R_k	[mol/s]	Net rate of production of each species by chemical reaction
$R_{a,k}$	[mol/(m^3s)]	Absorption rate of component k
$R_{r,k}$	[mol/(m^3s)]	Reaction rate of component k
S_h	[J/s]	Heat source term
t	[s]	Time

T	[K]	Temperature
T_0	[K]	Initial temperature of fluid or absorbent pellet
T_f	[K]	Temperature of fluid
T_s	[K]	Temperature of solid
T_w	[K]	Temperature of column wall
T_{cm}	[K]	Critical temperature
u	[m/s]	Fluid velocity
V	[m^3]	Vessel volume
V_{Tot}	[m^3/s]	Volumetric flowrate of all components (forward direction)
V_{cm}	[m^3/mol]	Critical volume
$V_{a,c}$	[m^3]	Volume of absorbent in the absorbent packed bed
$V_{a,f}$	[m^3]	Volume of fluid in the absorbent packed bed
$V_{r,c}$	[m^3]	Volume of catalyst in the catalyst packed bed
$V_{r,f}$	[m^3]	Volume of fluid in the catalyst packed bed
x_{Ru}	[-]	Parameter of Ru catalyst synthesis rate
X	[1]	Reaction conversion
y_{Ru}	[-]	Parameter of Ru catalyst synthesis rate
y_k	[1]	Molar fraction of component k
Y_k	[1]	Mass fraction of component k
z	[m]	Distance in the catalyst bed or absorbent bed
z_{Ru}	[-]	Parameter of Ru catalyst synthesis rate

Greek letters

Symbol	Units	Description
α	[1]	Reaction exponent constant (between 0.5 and 0.75)
β	[1]	Backflow fraction
ε	[1]	Catalyst bed void fraction
ϵ_b	[1]	Absorbent bed void fraction
$\bar{\bar{\tau}}$	[N/m^2]	Stress tensor
ρ	[kg/m^3]	Density of the fluid
ρ_{cat}	[kg/m^3]	Density of catalyst pellet
μ	[m^2/s]	Dynamic viscosity (also called coefficient of molecular viscosity)
ϕ_k	[-]	Fugacity coefficient
λ_L	[W/(m·K)]	Effective axial thermal conductivity

Subscripts

Symbol	Description
0	Entrance of reactor (initial value)
$1, 2, ...$	Cell/stage number in absorbent bed/catalyst bed
eff	Effective
i, m, j, n	Cell/stage number in absorbent bed/catalyst bed

j'	Component of coordinate
k	Numerator for component
mix	Mixture
N-1, N	Stage number in the catalyst bed
Tot	Total fluid

List of Abbreviations

SEM	Scanning Electron Microscopy
STEM	Scanning transmission electron microscope
TEM	Transmission Electron Microscopy
TPR	Temperature Programmed Reduction
XRD	X-ray Powder Diffraction
XPS	X-ray Photoelectron Spectroscopy

Abstract

This thesis investigates the design and performance of absorbent-enhanced ammonia synthesis reactors. The per-pass conversion of ammonia can be improved by the sequencing of ammonia synthesis catalyst and ammonia-selective absorbent beds in the reactor. A new perspective includes adjacent coupling and multi-bed coupled absorptive reactors which contributes to the exciting area of ammonia synthesis improvement. This type of reactors enable operation under conditions milder than those used in a traditional Haber-Bosch reactor. As part of the work a novel Ru catalyst with polar metallic oxide support was developed to meet the requirements of mild operating conditions of the absorptive reactor. An experimental unit was built to perform the synthesis of ammonia in a fixed-bed absorptive reactor, and an increased per-pass conversion was observed from experimental data. Mathematical models were also developed to provide insights into the reasons for the conversion improvement in the absorptive reactor. Our simulations of these two kinds of absorption-enhanced ammonia synthesis reactors contribute to their understanding and confirm the enhancement of their per-pass conversion. A preliminary mathematical model study of the adjacent coupling absorptive reactor was carried out first in which the influence of absorption on the per-pass ammonia conversion was linked to a hypothetical recycle stream. Based on the result of this preliminary model, a more detailed transient backflow cell model was developed to simulate the behaviour of the adjacent coupling absorptive reactor. Given the complexity of the reacting fluid through the fixed bed, a computational fluid dynamics simulation via ANSYS Fluent was also generated and resulted in similar results to those of the transient backflow cell model. On this basis, an improved absorptive reactor, i.e. the multi-bed absorptive reactor, was proposed and modelled in Fluent, achieving close to 100% per-pass conversion. This research improved the per-pass conversion of ammonia synthesis reactors and enabled milder operating conditions for process. Furthermore, a theoretical framework was provided through mathematical modelling for optimisation purposes.

Chapter 1. Introduction

1.1 Context and motivation

Ammonia is a chemical that is essential to human society. The main reason for ammonia's significance is that it is the feedstock for the synthesis of nitrogen-compound fertilisers [1]. Moreover, with a high hydrogen density, ammonia has also been regarded as a potential hydrogen carrier, which is a clean energy source and is carbon-free, as opposed to hydrocarbons and alcohols [2]. The demand for synthetic fertilisers has substantially increased along with the development of humanity. Therefore, ammonia synthesis through the Haber-Bosch process is widely recognised as one of the most significant industrial applications [3]. The Haber-Bosch process is the most commonly used process for ammonia synthesis today. It takes place in large-scale chemical plants, which use a hydrocarbon feedstock, such as natural gas, in a steam methane reforming process to produce hydrogen. Hydrogen is then combined with nitrogen, obtained from an air separation unit, in a catalytic packed bed reactor operating at high pressure (150–250 bar) and high temperature (400–500°C). Given the low per-pass conversion in the reactor (15–25%), the unconverted reactants have to be recycled to achieve a high process conversion [4]. This recycle consumes large amounts of energy to separate ammonia through condensing and to reheat hydrogen and nitrogen to the synthesis temperature level.

The conventional Haber-Bosch process dominates current industrial ammonia production nowadays [5]. However, with growing global market demands for ammonia, the adaptation of ammonia synthesis technology to have higher per-pass conversion and be less energy-intensive has attracted much attention. An efficient, affordable energy process for the production of ammonia would be one of the most important technologies of the future.

The low per-pass conversion of ammonia synthesis is mainly caused by the reversible nature of the ammonia synthesis reaction:

$$3H_2 + N_2 \rightleftarrows 2NH_3$$

Fast and efficient removal of ammonia from the gas stream can tilt the reaction balance, and therefore, promote the synthesis progression. The main objective of this thesis is the study of an innovative and less energy-intensive process for ammonia production by combining reaction and in-situ separation of ammonia to promote reactor performance. Ammonia absorption has been considered as an efficient separation approach accomplished by adding absorbent into the reactor. This thesis focuses on an absorption-enhanced reaction process to displace the chemical equilibrium to the products side and therefore lead to a higher per-pass conversion. In the conventional synthesis process ammonia needs to be chilled to about −20 °C to condense. The remaining nitrogen, hydrogen, and ammonia vapour are heated back at the reactor temperature, which involves a high energy expenditure. As ammonia is separated by using absorbent, these required energy can be eliminated. Meanwhile, as the per-pass conversion is improved, the energy for recycling the unreacted reactants to synthesis can also be decreased.

Multifunctional reactors are essential components of process intensification, which integrate reaction and at least another function into a single unit operation. This research proposes a new perspective of the multifunctional reactor regarding the performance of the reaction-absorption process for ammonia synthesis: adjacent coupling (one bed of catalyst followed by one bed of absorbent), and multi-bed coupled (multi-beds of catalyst and absorbent) absorptive reactors with both functionalities (reaction and separation) in a single unit. This mode of operation increases the driving force of the reaction and reduces the constraint imposed by the reversible reaction, therefore, improving per-pass reaction conversion.

A sketch of the adjacent coupling configuration is presented in Figure 1.1. In this case, the absorbent bed immediately follows the catalyst bed, and the reaction and absorption take place sequentially in two separate beds without recirculation. The adjacent coupling absorptive reactor contains only one bed of catalyst bed with one bed of absorbent bed. In the experimental part of this research the catalyst and absorbent were placed in a single vessel while running at different temperatures. The catalyst and absorbent are separated from each

other using quartz wool, and the ammonia production amount was recorded. In this thesis, the concept of ‘backflow’ is first proposed as an explanation of the absorption-enhanced ammonia conversion in the adjacent coupling absorptive reactor.

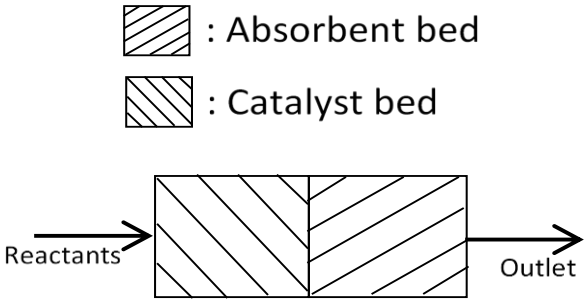

Figure 1.1. Schematic of the adjacent coupling absorptive reactor configuration.

The multi-bed coupled absorptive reactor is depicted in Figure 1.2. There are more than two beds of catalyst and absorbent beds. The number of beds and the length of each bed have been designed to improve the reactor performance. In this configuration, the operating temperature is uniform through the reactor. Catalyst in the multi-bed absorptive reactor needs to work under lower temperature than the conventional Haber-Bosch reactor to match the operating temperature of the absorbent. Therefore, a novel catalyst that can perform well even under mild conditions is necessary to be synthesised.

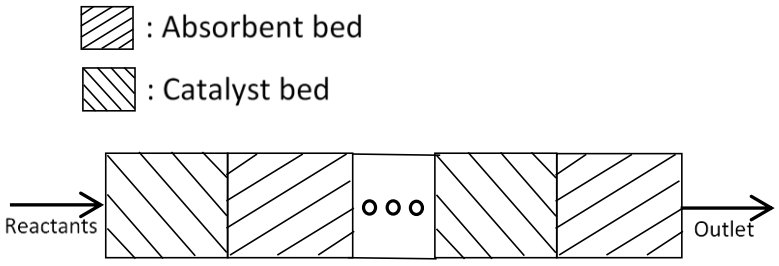

Figure 1.2. Schematic of the multi-bed coupled absorptive reactor configuration.

It was noted that adjacent coupling and multi-bed coupled can improve the per-pass conversion continuously in an ammonia synthesis reactor. Once the absorbent is saturated in

one vessel, the reactants will be switched to another vessel configured identically. Moreover, the saturated absorbent can be regenerated through high temperature and low pressure at the same time. For the adjacent coupling configuration, the reaction per-pass conversion can be improved by coupling with the absorption, which was discussed in Chapters 3, 4 and 5. For the multi-bed coupled configuration, each absorbent bed before the catalyst bed will drive the reaction to the right in the next catalyst bed. Therefore, the per-pass conversion of the reactor will increase, and the critical point for this configuration is then to find the improved reactor design.

There has been little research of reaction-absorption processes conducted for ammonia synthesis. The group of Prof E. L. Cussler investigated a reaction vessel for ammonia synthesis under batch [6] or semi-batch [7] regimes. For example, the batch reactor simultaneously contained the catalyst and an absorbent [6], where the reaction and absorption occurred at a single temperature in the same piece of process equipment. However, these processes could not be operated continuously, which will limit the speed and the yield of ammonia in industry scale. In this research, the adjacent coupling and multi-bed coupled absorptive reactors were proposed to produce ammonia continuously. Furthermore, relatively little attention has been paid to the simulation of ammonia absorptive reactors to guide the future development, which was also involved in this thesis.

The main contributions of this work can be summarised in the following items:

- Our new perspective of adjacent coupling and multi-bed coupled absorptive reactors contribute to the exciting area of ammonia synthesis optimisation, specifically through the use of absorbent for rapid separation.
- Our simulation of these two kinds of absorptive reactor contributes to the understanding of the absorption-enhanced ammonia synthesis reactors. Furthermore, our simulations confirm the enhancement of the per-pass conversion in both the adjacent coupling and multi-bed coupled absorptive reactors.
- A novel catalyst is proposed giving a feasible direction of improvement for ammonia synthesis catalysis.

1.2 Outline of the thesis

This thesis is outlined as follows.

Chapter 2 contains a literature review on the development of ammonia synthesis processes, catalysts, and recent research study on the absorptive reactors as well as numerical methods.

In Chapter 3 a tentative model of the adjacent coupling absorptive reactor is addressed. The adjacent coupling reactor was tested in a lab-scale reactor, and a fixed-bed model with a hypothetical recycle stream was developed to simulate the higher performance of the absorptive reactor with respect to a conventional reactor.

In Chapter 4 a more detailed model, the transient backflow cell model, was studied for the adjacent coupling absorptive reactor. The reasons for the improvement of conversion are identified in this chapter. The absorption effect is identified and the optimal absorbent amount is determined for the more efficient absorptive reactor.

Chapter 5 deals with the simulation of an adjacent coupling absorptive reactor using ANSYS Fluent as computational fluid dynamics tool that can better represent the flows between the catalyst and absorbent beds in the absorptive reactor. Using this model, a multi-bed coupled absorptive reactor is designed and simulated in Chapter 6.

Based on the design of a multi-bed coupled absorptive reactor, catalysts that can maintain a high production rate at low operation temperatures are needed. Therefore, Chapter 7 focuses on the development of a novel catalyst that can operate under milder conditions, especially lower temperatures.

The final chapter presents the conclusions of the DPhil research and some suggestions for future work.

Chapter 2. Literature review

In this chapter, previous studies in the development of ammonia synthesis process and of ammonia synthesis catalysts are reviewed. The sorption-enhanced ammonia synthesis reactor is one way to improve the reactor performance, which is specifically presented. Furthermore, the numerical simulation methods are also mentioned in this literature review.

2.1 Developments of ammonia synthesis

In industry, the per-pass conversion of ammonia synthesis is only about 15% conducted at pressures above 100 bar and between 400 and 500 °C, but any unreacted gases are recycled, and finally an overall conversion of 97% can be achieved [8]. This conventional Haber-Bosch process, requiring high temperatures and pressures, is energy-intensive and releases a large amount of CO_2, while the per-pass conversion is still low. Therefore, numerous studies have been carried out in the pursuit of highly efficient ammonia production with lower energy consumption as well as a higher per-pass conversion.

In recent years, the specific energy consumption for the overall ammonia plant has been reduced by approximately 30% [5], and about 30% can still potentially be gained before the theoretical minimum energy consumption is reached. Meanwhile, electric power generated from renewable energy sources, such as wind, solar, and tidal, has become more technically and economically viable for smaller units of ammonia synthesis. It has been suggested that such an integrated, electrically powered process would facilitate the miniaturisation of ammonia synthesis to enable local-scale, distributed energy storage [9]. Similarly, different cooling methods of ammonia synthesis reactor had been modelled and compared to find the most efficient one and therefore reduce energy consumption [10]. However, the majority of this gain will most likely be achieved in the synthesis gas generation part of the plant (pinch technology), rather than in the ammonia synthesis itself. The operating conditions for ammonia synthesis are still energy-intensive.

Current technologies for ammonia production under mild conditions largely include electrochemical synthesis [11], photochemical synthesis [12], chemical looping process [13], and sorption-enhanced ammonia synthesis [14], which are emphatically reviewed in this chapter.

2.1.1 Electrochemical ammonia synthesis

It is particular attractive to reduce nitrogen to ammonia via renewable electricity power. The electrochemical N_2 reduction reaction through a proton-coupled electron transfer process has been established under mild conditions, especially at room temperature and ambient pressure [15]. Water is a ubiquitous and sustainable source of protons and electrons for the hydrogenation of nitrogen to ammonia. Electrochemical systems employ H_2O and N_2 as feedstock to produce NH_3 by converting H_2O to O_2 ($N_2 + 3H_2O \rightarrow 2NH_3 + 1.5O_2$) [16]. This electro-synthetic cell for ammonia production could allow NH_3 to be generated sustainably in small, low-cost devices [17]. An efficient electrochemical system under ambient conditions was reported in [18] with enhanced NH_3 production rates. Employing electro-catalysts is an effective strategy to enhance intrinsic reactivity and selectivity toward N_2 reduction.

Density functional theory calculations identify that Rh and Ru could be possible cathodic electrocatalysts for electrochemical ammonia synthesis [15]. Besides, the tetrahexahedral gold nanorods was also used as a heterogeneous electrocatalyst for the electrocatalytic nitrogen reduction reaction under mild conditions [19]. Mo-based catalysts were prepared and investigated [20], which enhanced the activity of nitrogen reduction due to the active surface provided by Mo. Another non-noble metal electrocatalyst is the use of porous Ni as electrode, which was in favour of ammonia electro-synthesis [21]. Furthermore, there are also little researches focused on the single-atom electrocatalysts for nitrogen reduction reaction to maximum atomic usage and improve activities of catalysts [22]. Recently, metal-free electrocatalysts have also been focused on as promising alternatives to the traditional metal based catalysts. For example, carbonaceous electrocatalysts have shown the good electrocatalytic activities for nitrogen reduction reaction at ambient conditions [23].

The latest development of Haldor Topsøe electrochemical production of ammonia has attracted substantial interests. Haldor Topsøe has greatly focused on green ammonia by using a solid oxide electrolysis cell to produce ammonia from air, water, and renewable electricity [24]. However, the design of an electrochemical system with both high catalytic activity and high selectivity under ambient conditions is still very challenging [25].

2.1.2 Photochemical ammonia synthesis

The photochemical N_2 reduction uses solar energy directly to drive the reaction. Generally, the photochemical N_2 reduction involves light absorption to generate photo-excited charge carriers, separation and migration of the electron-hole pairs to the surface reactive sites, and the reaction of photo-induced electrons with N_2 to form NH_3 with the uptake of water-derived protons [26]. Photoexcitation is the first stage of nitrogen photo-reduction. This stage generate the photo-induced holes in the valence band and electrons in the conduction band of semiconductor nanoparticles. The charge separation and the migration of photo-induced carriers are the second stage. In the final stage, the electrons transfer across the bulk and the surface of photocatalysts. The electrons reach the active sites. These sites adsorb nitrogen molecules and reduce them to ammonia by the electrons, while water is oxidized by holes and oxygen is produced [27]. A rather negative electrode potential position is required for this reduction of nitrogen molecules. Therefore, the significant point is to develop suitable semiconductor-based nanocatalysts for photo-driven nitrogen reduction reaction to produce ammonia.

The photocatalysts' efficiencies have been improved through heteroatom doping [28], crystal facet engineering [29] and surface plasmon modification [30]. Inspired by the widespread application of TiO_2 in the photolysis of water, the TiO_2-based catalyst is the focal system for a photochemical N_2 reduction reaction [31]. The photoelectrochemical assessment of bismuth oxyhalides (BiOCl, BiOBr, or BiOI) has been reported, which have high photocatalytic activities [32]. Meanwhile, transition metals are also utilized to enhance photochemical efficiency in [33]. A photoelectron-chemical reaction cell through a strontium titanate photo-electrode loaded with

gold nanoparticles has been developed [34]. Solar-driven N_2 fixation, if realised, would provide sustainable and distributed processes to exploit clean and unlimited sunlight for producing renewable fertiliser and controlling the global nitrogen cycle [35].

2.1.3 Chemical looping process for ammonia synthesis

The chemical looping process, with the advantage of atmospheric pressure operation, high product selectivity and energy efficiency, has been extensively investigated in the field of carbonaceous fuel conversion, such as chemical looping combustion, reforming and gasification processes [36]. Herein, a two-step cyclic process for ammonia synthesis were discussed in [37], consisting of an endothermic carbo-reduction of Al_2O_3 in a nitrogen atmosphere, followed by exothermic hydrolysis to produce ammonia. The ammonia synthesis was separated into two reaction steps to design the catalyst not been limited by strong correlations between activation energies and adsorption energies of reaction intermediates [38]. The alkali and alkaline earth metal imides were reported to produce ammonia via a two-step chemical looping process operating under mild conditions [39]. Solar thermochemical ammonia synthesis is another potential route to produce NH_3 from air, water, and concentrated sunlight. This process involves the chemical looping of an active redox pair that cycles between a metal nitride and its complementary metal-oxide to yield NH_3 [40].

2.1.4 Sorption-enhanced ammonia synthesis

Among the current technologies, thermochemical synthesis is still the most economic and widely employed for ammonia production. It is a well-established large-scale technology producing above 200 million tons per year of ammonia [41]. However, recycling the unreacted hydrogen and nitrogen in conventional thermochemical synthesis does not fundamentally solve the problems of the particularly low per-pass conversion, 15-25% [4]. To accomplish an increase in per-pass conversion, the thermochemical synthesis can be modified to include

ammonia capture. This thesis focuses on the absorption-enhanced ammonia synthesis process, a technology that could improve the per-pass conversion of the reactor.

Multifunctional reactors are essential components of process intensification, which integrate reaction and at least another function into a single unit operation. The concept of 'sorptive reactor' (absorptive or adsorptive), in which a sorption function is incorporated into the traditional reactor, is similar to the reactor design in this thesis and can substantially improve reactant conversion [42]. The sorptive reactor is one kind of the multifunctional reactors, integrating reaction and separation function into a single unit operation resulting in higher reactor performance. Many studies have focused on adsorptive reactors, while few have focused on absorptive reactors. Adsorption refers to the physical bond between adsorbate molecules and a solid surface. Adsorbent materials that display this mechanism have a much lower potential capacity, which is limited by surface area, are inherently less selective, and have a lower binding energy than absorbent materials. Absorbents, such as the materials discussed in ammonia absorption, selectively incorporate molecules into the crystal lattice and offer a higher capacity, higher selectivity, and are more stable at high temperatures. The adsorptive reactor concept was proposed for the steam methane reforming process, in which the sorbent and catalyst were well mixed [43]. Kodde et al. addressed the use of this kind of packed bed (well-mixed sorbent and catalyst) operated in a pressure-swing mode, which led to a near triple improvement in productivity compared with a pressure-swing separation and a plug-flow reactor in series [44]. Meanwhile, an isothermal sorptive reactor has also been studied, which is sequentially subdivided into three segments: catalyst bed, sorbent bed, and catalyst bed [45]. Gas-phase sorption would seem to be an especially appropriate separation process to enhance heterogeneously catalysed gas-phase reactions [46].

For ammonia synthesis, few research studies have investigated using the absorptive reactor. The sorption-enhanced ammonia synthesis was proposed and the optimal conditions for the cyclic uptake and release of ammonia from the absorbents were discussed in [47]. M. J. Palys created a dynamic model of the absorbent-enhanced process using gPROMS ModelBuilder [48]. Ammonia selective absorbent was used to synthesis ammonia at low pressure driven by

wind energy [49]. For example, calcium chloride was chosen as the selective absorbent for a wind-generated ammonia synthesis process [50]. Smith et al. studied the reaction and absorption at a single temperature in the same piece of process equipment, as illustrated in Figure 2.1 [6]. In their absorptive batch process, ammonia is rapidly and reversibly absorbed to increase the production rate of the catalyst, thus shifting the equilibrium of the catalyst system. Such absorption can occur at considerably higher temperatures than most adsorptions and can also be much more selective than adsorption. Also, the absorption-based process can remove the ammonia more completely than condensation does. In principle, the combination of reaction and absorption can achieve a higher ammonia conversion than the conventional Haber-Bosch reactor. If the absorbent is fully mixed with the catalyst, then there is a chance to increase the conversion and always suppress the reverse reaction continuously by separating ammonia. However, the separation of catalyst and absorbent would be difficult and therefore, it would be hard to regenerate the absorbent or replace the deactivated catalyst. Furthermore, this batch reactor cannot perform continuously. Therefore, arranging the catalyst and absorbent in beds could be a solution. The adjacent coupling and multi-bed coupled absorptive reactors in this thesis are possible ways to improve it.

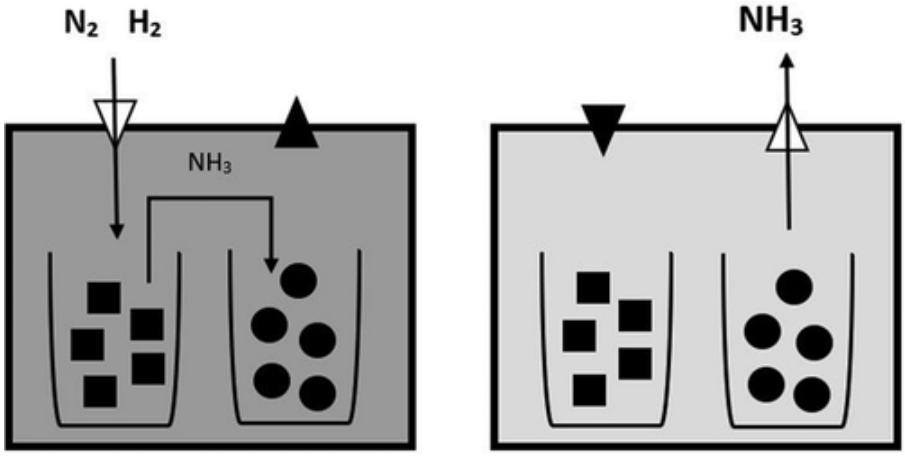

Figure 2.1. Constant temperature process for ammonia synthesis (The squares represent catalyst pellets while the circles absorbent pellets). The left image illustrates the absorbent quickly absorbing in a high-pressure step, in which ammonia is synthesised over the catalyst. The right image displays the regeneration step at low pressure [6].

As for absorbent materials, solid-state materials, such as metal hydrides, metal halides and metal borohydrides, have been investigated to store ammonia with high efficiency at moderate temperatures and pressures [51]. Some elements, especially belonging to groups I−IV, can form metal hydrides. These materials (LiH, NaH, KH, MgH_2, and CaH_2) can easily react with ammonia to form nitrides and amides/imides ($LiNH_2$, $NaNH_2$, KNH_2, $Mg(NH_2)_2$, and $Ca(NH_2)_2$, respectively) [52]. Another approach is to use metal halides as a media to remove ammonia [53]. The alkaline earth metal halides was studied on ammonia absorption−desorption behaviour to develop for ammonia storage [54]. The transition metal halide and ammonia could form hexa-ammine complexes [55]. Suitable metal halides can absorb a large amount of ammonia, and the volumetric hydrogen densities of ammine complexes are almost comparable with that of liquid ammonia [56]. More recently, NH_3 absorption properties of several kinds of alkaline earth metal halides ($MgCl_2$, $CaCl_2$, $CaBr_2$, $SrCl_2$, and $SrBr_2$) have been studied at low pressures [57]. The reactivity of the metal chlorides was also verified after ten cycles of absorption and desorption [58]. The thermodynamic properties for ammonia absorption of metal halides were also systematically investigated in [59].

The thermodynamic equilibrium for ammonia absorption with metal halides can be determined by the Clapeyron equation.

$$\ln p_{NH_3} = -\frac{\Delta H^0}{RT} + \frac{\Delta S^0}{R}$$

where p_{NH_3} is the partial pressure of ammonia, ΔH^0 and ΔS^0 are the standard enthalpy and entropy changes when complexing a molecular unit of ammonia, R is the universal gas constant, and T is the temperature. The equilibrium pressures for metal halide-ammonia has been studied and listed in [60]. Generally, a thermogravimetry apparatus would be used to identify the thermodynamic properties of ammonia sorption. For example, the thermodynamic parameters for ammonia sorption on $SrCl_2$ were obtained including the reaction enthalpy and entropy [61]. The ammonia sorption equilibrium for composite sorbents has also been investigated, based on a binary salt system ($BaCl_2$ + $BaBr_2$) [62].

Actually, physical adsorption, due to Van der Waals forces, has a larger effective distance between the molecules of ammonia and metal halides than that of chemical absorption. Therefore, physical adsorption occurs before chemisorption (absorption) [63]. If this distance is reduced, the activation energy of absorption could decrease, then it could be easier to transit from physical adsorption to chemical absorption [63].

The kinetic models for metal halide-ammonia have been analysed and discussed to explain the absorption mechanisms. Lebrun and Spinner classified the kinetic model of chemisorption into two categories: phenomenological and analogical models [64]. The phenomenological models are based on the physico-chemical properties, which require the detailed reaction mechanisms. However, the analogical approach does not involve detailed reaction mechanisms and only describes the overall performance and effect of solid sorbents [64]. Several kinetic models for chemisorption have been applied recently. A Sudden Vector Projection model has been proposed to describe the water dissociative chemisorption on several metal surfaces [65]. Later, a quantum model for methane dissociative chemisorption on metal surfaces was presented [66] to predict the reaction behaviour. This quantum model was also used to study the hydrogen sorption on a Cu surface [67].

2.2 Developments of ammonia synthesis catalyst

It has been over 100 years since Haber and Bosch invented an ammonia synthesis catalyst. The ammonia synthesis reaction is reversible and limited by equilibrium under all practical conditions. Thermodynamic equilibrium favours low temperature and high pressure, ranging from 350 to 480 °C and 8 to 20 MPa, respectively, to yield a per-pass conversion of 15–25% in industrial practice [68]. Until the early 2000s, ammonia synthesis plants with daily production capabilities of 1,000 or 2,200 tonnes were universal [68]. The nitrogen molecule is one of the most difficult substances to activate because the dissociation energy of the N≡N triple bond is 942 kJ/mol [69]. The very stable N≡N bonding is the main restriction in ammonia synthesis, which has led to the development of heterogeneous catalysis for industrial applications, such

as Fe- [70] and Ru-based [71] ones. Since the strong thermodynamic barrier of the nitrogen triple bond dissociation limit ammonia rates under such mild conditions, a more efficient catalyst to achieve high ammonia production rate is required.

Heterogeneous catalysts for ammonia synthesis are composed of three parts: the active phase, promoter and support. The active phase is responsible for catalytic activity, which must exist in the catalyst. The promoter is applied to substances that are not intrinsically catalytically active to allow the active phase to function at its maximum capacity [72]. The catalyst support is the carrier for the active phase and any promoters that may be present. It can maximise the surface area of the active phase by providing a large area, over which it may be spread, as well as allowing the active phase and the promoters to form the particles suitable for use in fixed-bed reactors [72]. The development of ammonia synthesis catalysts is mainly focused on the improvements of the catalyst composition, which is examined in detail in the following sections.

2.2.1 Development of the active phase in a catalyst

The active phase of the ammonia synthesis catalyst has come through several development periods such as iron-based catalysts, ruthenium-based catalysts, and the Co-Mo-N system [69]. From 1909 to 1911, Haber and other scientists vigorously explored catalysts, and 2,500 different catalysts were tested. Over 5,000 different catalyst systems had been tried during catalyst selection by 1922 [69]. Iron has been known as an effective catalyst for ammonia synthesis since 1905. Until now, the fused iron catalysts still occupy a preeminent position in the industry. Meanwhile, the Co-containing catalyst was a significant development for the traditional Fe_3O_4-based fused iron catalyst, such as the cobalt-iron catalyst [69]. The $Fe_{1-x}O$-based ammonia synthesis catalyst was then invented, which improves the performance of the fused iron catalyst, and is the most active fused iron catalyst in the world [73]. In 1972, a catalyst system with ruthenium (Ru) as the active phase, potassium as the metal promoter, and carbon as the catalyst support was found to have high activity [74]. Ru-based catalysts

have demonstrated higher performance in milder conditions (370–400 ˚C and <50 bar) than the industrially used Fe-based catalysts (usually 400–500 ˚C and >100 bar) [75]. A mesoporous carbon-supported Ru catalyst with Cs promoter (Cs-Ru/MPC) was prepared and used for sustainable ammonia synthesis under mild reaction conditions [76]. The Cs-Ru/MPC catalyst demonstrated high activity and stability in a wide range of reaction temperatures. Most scientists have shifted their main research direction to the study of the ruthenium-based catalyst [5].

Figure 2.2 is a volcano plot of the ammonia synthesis activity against the number of electrons in the *d* orbital for Group VIII metals. It is worth noting that the three most active metals have the same seven electrons in their *d* orbital. Among these metals, the most commonly used catalyst is magnetite, due to its lower cost and greater availability in comparison to ruthenium and osmium [77]. However, it has been reported that the ruthenium catalyst exhibits five times higher activity under the same temperature. Therefore, a more efficient Ru catalyst to achieve high ammonia production rate is necessary, desirably requiring a small amount of Ru to control costs.

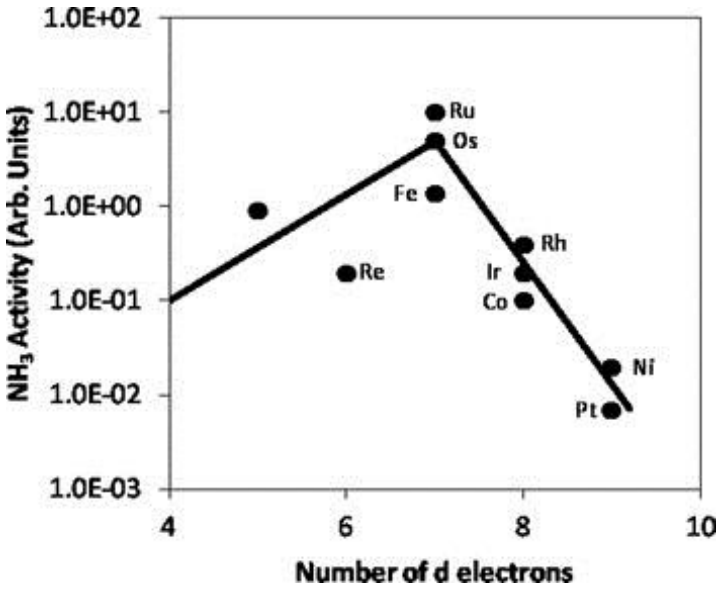

Figure 2.2. Volcano plot of ammonia synthesis catalysts [77].

2.2.2 Development of the catalyst support

Ru-based catalyst is one of the most active monometallic ammonia synthesis catalysts, and its catalytic performance is strongly influenced by the support. Many conventional and nanostructured materials, such as carbon [78], metal oxide (MgO, CaO, Al_2O_3, TiO_2) [79], and zeolites [80], have been investigated as supports for Ru-based catalysts in ammonia synthesis. British Petroleum (BP) was responsible for loading ruthenium carbonyl compounds on graphite carbon carriers to create a new carbon-supported Ru (Ru/C) catalyst. With ten years of joint efforts, the Kellogg Company successfully developed a new ammonia synthesis process that applied to the Ru/C catalyst and was adopted by industry [9].

Some recent progress focus on choosing rare earth oxides as the catalyst support, such as CeO_2 [82], La_2O_3 [83], $La_{0.5}Ce_{0.5}O_{1.75}$ [84]. Ru/$La_{0.5}Ce_{0.5}O_{1.75}$ catalysed ammonia synthesis exhibits particularly high rates under mild conditions, specifically at a reaction temperature of 350 ˚C [84]. Similarly, the Ru/$La_{0.5}Pr_{0.5}O_{1.75}$ catalyst also performed with high NH_3 synthesis rates under mild conditions. The synthesis rate was equivalent to the most active oxide-supported Ru catalysts [85]. Three different morphologies of CeO_2 in the Ru/CeO_2 catalysts (i.e. cube spheres, microspheres, and nanorods) were evaluated in terms of their effect on ammonia synthesis activity. According to the results from transmission electron microscopy, the dispersion of active metal Ru was affected by the morphology of CeO_2. Ru nanoparticles in Ru/CeO_2 were more electron-rich and thus more capable of back-donating electrons to adsorbed N_2 and subsequently activating it. It was indicated that the morphology effect of the CeO_2 supports on the Ru/CeO_2 catalyst was related to their pore size distribution and surface oxygen vacancies [86].

In recent years, inorganic electrides have also been actively explored as support, such as C12A7:e−. An electride is an ionic compound, in which electrons serve as anions. C12A7:e^- is composed of the abundant oxides CaO and Al_2O_3 and has exhibits high chemical and thermal stability [87]. As the rate-determining step of ammonia synthesis is the dissociation of N_2, it can be significantly promoted by having electrons donated to Ru [75]. The stable electride

C12A7:e^- works as a prime electron donor to enhance the catalytic activity for ammonia synthesis [87].

2.2.3 Development of the catalyst promoter

The catalytic performance is also strongly influenced by the promoter. Alkali, alkali earth, and rare-earth metals are the most commonly studied promoters for Ru-based catalysts in ammonia synthesis, such as Li, Na, K, Rb and Cs [88]. Alkali metal hydrides, such as LiH, NaH, KH, CaH_2 and BaH_2, have been especially explored as efficient promoters, and have a high potential for low-temperature ammonia synthesis. The usage of LiH on transition metals creates an energy-efficient pathway for ammonia synthesis under mild conditions [89]. In other words, LiH provides negatively charged hydrogen atoms that remove activated nitrogen atoms from the transition metal and binds nitrogen atoms to form $LiNH_2$. CaH_2 is also one simple hydride, which exhibits catalytic performance with Ru comparable to $Ru/Ca_2N:e^-$. $Ru/Ca_2N:e^-$, a two-dimensional electride combined with ruthenium nanoparticles, exhibits efficient and stable catalytic activity down to 200 °C [90].

2.2.4 Nano-materials employment

The employment of nano-materials to obtain more active synthesis catalysts is also a novel approach in catalyst formulation. Reducing the size to nanoscales significantly increases the surface area, which, in turn, increases the level of catalytic activity [91]. It was found that the best performance for ammonia synthesis is provided by Ru catalyst with an average size of 2.1 nm [92]. Reducing the Ru crystallite (microscopic crystal) size could also increase the density of highly active B_5 sites and therefore improve catalytic activity. B_5 sites are the exposed three-fold hollow sites, acting as catalytic centres and thus dominating the reaction rate [92][93]. They were recognised as being responsible for a strong physical adsorption of nitrogen. The B_5 site of the Ru surface has been proposed for the activation of the dinitrogen

molecule to nitrogen atoms [94], while other surface ruthenium atoms may also be active for nitrogen activation [95].

However, competitive adsorption exists between H_2 and N_2 at the active sites. Due to the high activation energy barrier for dissociative nitrogen, H_2 molecules, in contrast to N_2 molecules, can easily adsorb. As a consequence, hydrogen preferentially blocks the sites for nitrogen dissociation, which triggers the H_2 poisoning effect in the presence of the un-promoted Ru catalyst [96]. The surface poisoning of Ru sites by competitive H_2 adsorption limits the overall rate of ammonia production. Therefore, the improved catalyst in this project attempted to minimise the effect of hydrogen poisoning on the ammonia synthesis reaction.

2.3 Numerical Simulation

A steady-state, one-dimensional mathematical model of an ammonia synthesis reactor coupling with absorption was implemented using MATLAB [97]. In that MATLAB model, the absorbents were introduced as a fluidised solid phase in the catalyst bed. Therefore, the mathematical model included the material and energy balances for the reactants (hydrogen and nitrogen) and product (ammonia) in the gas phase, the material and energy balances for the product in the fluidised solid phase (absorbents) [97]. Dashti et al. also modelled an industrial ammonia synthesis reactor, in which the differential equations were solved using 4^{th} order Runge Kutta method [98]. According to their mathematical model results, the bottlenecks were found and better technological condition was determined [98].

Similarly, in this thesis, the mathematical models for the simulation of the adjacent coupling and multi-bed coupled absorptive reactor were solved numerically using MATLAB. Ordinary differential equations (ODEs) and partial differential equations (PDEs) are the main problems needed to be solved for mass, energy and momentum balances. The numerical solution of ordinary differential equation mainly consists of the Euler method and Runge-Kutta method [99]. The Runge-Kutta-Fehlberg method, a 4th-order adaptive step-method, is used to solve this system of ordinary differential equations. Numerical solution of partial differential equations

[100] emphasis on finite difference methods, finite volume methods, finite volume method, spectral method and method of lines. The numerical method of lines is used to solve this system of partial differential equations in Chapter 3. Meanwhile, in Chapters 5 and 6, the finite volume method is applied in the Fluent simulation of the adjacent coupling and multi-bed absorptive reactor.

Over the last few decades, CFD simulation has developed rapidly with the ever-increasing computing power and has become an essential tool in fluid research, especially reacting flows. ANSYS Fluent, as one CFD software, was chosen as the tool to simulate the ammonia synthesis reactor and specify the effect of absorbent in this chapter, based on the convection-diffusion model. Many researchers had chosen Fluent to simulate industrial processes due to its efficient and flexible workflows and robust capabilities in geometry modelling and meshing [101][102]. For example, a tubular electrochemical reactor was modelled through Fluent to describe the process of convective mass transfer [103]. Fluent can handle not only complex flow conditions but also reacting flows. A membrane-based reformer-combustor reactor for hydrogen generation was developed through Fluent to improve the overall thermal efficiency in [104]. Simulation of the hydrogen separation process in a membrane reactor was developed in Fluent [105]. Rabbani et al. modelled a trickle-bed reactor with filtration using Fluent in [106]. A rotor-stator spinning disk reactor for intensified biodiesel synthesis was described and numerically simulated via Fluent in [107]. To simulate with detailed chemical mechanisms, two sub-grid extinction models for eddy dissipation combustion were implemented in Fluent [108]. Moreover, a study of a cooling system via Fluent to optimise heat transfer parameters for higher reactor power levels was conducted in [109]. Even for ammonia synthesis, one analysis for magnetic induction in the monolithic channel was modelled through Fluent to improve the yield of ammonia [110]. However, for ammonia absorptive reactors, there has been paid relatively little attention on the CFD simulation, which would be involved in this study.

The aim of the present work is enhancing the Haber-Bosch reactor performance through the addition of an absorbent. Mathematical models of the absorptive ammonia synthesis reactor were also developed to explain the absorption effects on per-pass conversion and, therefore,

improve the reactor performance. Two kinds of absorptive reactors, adjacent coupling and multi-bed coupled, were simulated. The lab-scale experiments were conducted to verify that the per-pass conversion was enhanced in the adjacent coupling configuration. Furthermore, a novel design of an absorptive reactor, the multi-bed coupled reactor, was proposed and simulated to give a future development direction. Additionally, experimental preparation and characterisation of a novel Ru-based catalyst were performed to develop new high-efficiency Haber-Bosch catalysts. This catalyst working under lower temperature was necessary to be synthesised to meet the requirements of the multi-bed absorptive reactor. The overall objectives of this research are to improve per-pass conversion, allow for milder operating conditions in the Haber-Bosch reactor, and provide a theoretical framework through mathematical modelling of an ammonia absorptive reactor, based on experimental data, for improvement purposes.

Chapter 3. A tentative model of the adjacent coupling absorptive reactor: the recycle stream model

3.1 Introduction

As elucidated in this chapter, a tentative mathematical model of the adjacent coupling absorptive reactor for ammonia synthesis was developed and implemented in MATLAB. The model of the catalyst bed consisted of a set of simultaneous differential equations. The Runge-Kutta-Fehlberg method, a fourth-order adaptive step method, was used to solve this system of differential equations along the length of the catalyst bed. The dynamics of fixed-bed absorption also played a crucial role in this absorptive reactor. Due to the gradual saturation of the absorbent bed, an unsteady-state model was more reliable in the simulation of this ammonia reaction-separation process. The resulting set of coupled differential equations was numerically solved using the method of lines (MOL) implemented in MATLAB®. The MOL is one common method for the solution of partial differential equations (PDEs) [111].

A hypothetical recycle stream was then added to represent the backflow from the absorbent bed to the catalyst bed, shown in Figure 3.4(a), and the hypothetical recycle fraction was assumed to be equivalent to the degree of backflow in the reactor. Ultimately, it affected the per-pass conversion of ammonia synthesis. Varying degrees of backflow correspond to the varying distances between the absorbent and catalyst bed. Altering the degree of backflow resulted in different conversion values, a behaviour similar to the packed-bed bioreactor reported in the literature [112]. The relationship between the improvement in conversion and the distance between the absorbent and catalyst beds are discussed in this chapter.

The structure of this chapter is as follows. In Sections 3.2 and 3.3, the experimental setup and results are described, which demonstrated the enhanced conversion of ammonia synthesis. The mathematical model developed and implemented in MATLAB® is described in Section 3.4.

These models were solved simultaneously to obtain the simulation results shown in Section 3.5. Finally, the conclusions of the work are summarised in Section 3.6.

3.2 Experimental setup

The effect of the absorbent on ammonia production was tested in a fixed-bed continuous-flow reactor (Figure 3.1) using a commercial iron catalyst. This industrial iron catalyst was obtained from Johnson Matthey. A glass reactor tube (cross-sectional area 5.024×10^{-5} m^2) was packed with 0.1 g commercial iron catalyst (length of the catalyst bed is 0.01 m) and 1 g absorbent (length of the absorbent bed is 0.1 m) with quartz wool in between. $MgCl_2$ was chosen as the absorbent, as it has been reported to achieve absorption with a theoretical maximum of six ammonia molecules per magnesium ion [113]. Three different distances (0.0, 5.0, and 10.0 cm) between the catalyst and absorbent were studied. When the distance is 0.0 cm, the thickness of quartz wool is 0.1 cm, which was neglected in the simulation. A 3:1 mixture of H_2 and N_2 was passed through the reactor at a pressure of 50 bar and a weight hourly space velocity of 31,200 mL $g^{-1}h^{-1}$.

The reactor was equipped with three independent furnaces that allowed different sections to be heated to different temperatures. The temperature of each furnace was controlled by an independent thermocouple, which had its own temperature controlling unit. To regulate the temperature, the furnace could be ramped up and down, such that heat was supplied to the heating compartment or lost to the atmosphere. The catalyst was located in the middle furnace, while the absorbent was placed in the bottom furnace and controlled at a different temperature. As a pre-treatment step, the catalyst was heated to 773 K and the absorbent to 673 K for 12 h. This activated the catalyst through the removal of the surface oxide layer and removed the water content of the absorbent. During the reaction step (2 h), the catalyst was at 743 K (470°C) and the absorbent at 423 K (150°C). The ammonia absorption on $MgCl_2$ has been measured at temperatures up to 430°C [114] under high pressure. The absorbent is assumed to be stable through the testing. The kinetics of ammonia uptake was measured as changes in ammonia

pressure in a small cell of fixed volume held at constant temperature. When the cell contains no magnesium chloride, its pressure is constant for more than 6 h. When the cell does contain the chloride, its pressure drops over minutes [114]. Finally, any absorbed ammonia was desorbed by heating the absorbent to 673 K (400°C) at ambient pressure for one hour. The ammonia conversion was obtained from the produced ammonia trapped through gas chromatography (GC).

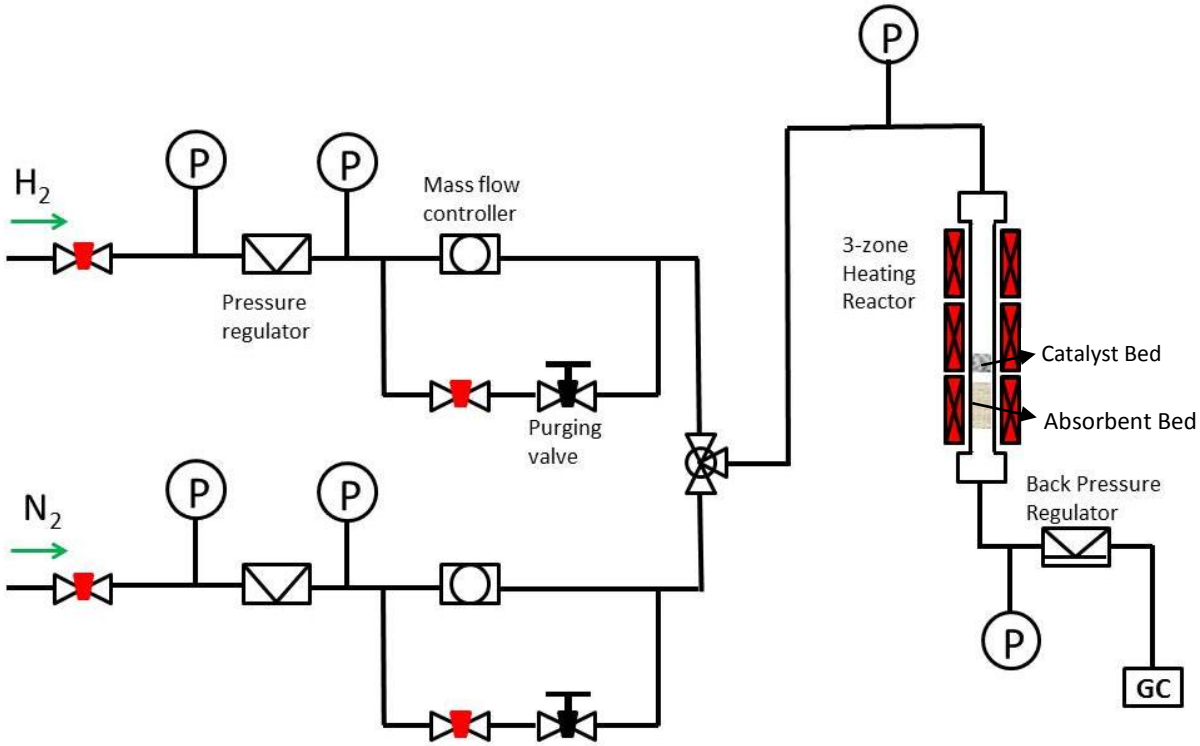

Figure 3.1. Schematic of the continuous-flow adjacent coupling absorptive reactor.

3.3 Experimental results

As illustrated in Table 3.1, the use of an absorbent increased the production rate of the catalyst, considering the desorption step. Three different distances between the absorbent and catalyst bed provided different production rates. The varying distances demonstrated that the closer the absorbent, the more of an improvement there was on the production rate. A distance of 0.0 cm between the catalyst and $MgCl_2$ more than doubled the reaction rate. A distance of 5.0 cm

between $MgCl_2$ and the catalyst increased reaction rate moderately, while a distance of 10.0 cm had a relatively small impact on the reaction rate of the catalyst.

Table 3.1. Catalyst reaction rate results, calculated from the ammonia collected with the catalyst at 743 K and absorbent at 423 K. A 3:1 mixture of H_2: N_2 at 50 bar and a weight hourly space velocity of 31,200 mL $g^{-1}h^{-1}$ were used. Ammonia was desorbed from the absorbent at 623 K and ambient pressure.

Absorbent	Distance between Absorbent and Catalyst	Catalyst Reaction rate	Per-pass reaction conversion
No Absorbent	-	30,000 μmol$g^{-1}h^{-1}$	4.31%
$MgCl_2$	0 cm	65,000 μmol$g^{-1}h^{-1}$	9.33%
	5 cm	48,000 μmol$g^{-1}h^{-1}$	6.89 %
	10 cm	32,000 μmol$g^{-1}h^{-1}$	4.59%

3.4 Mathematical model

A mathematical model was developed to analyse the effect of ammonia removal by absorption on an absorptive ammonia synthesis reactor – in other words, to model the experimental results presented in Section 3.3.

3.4.1 Ammonia synthesis model

The mass transfer associated with the catalyst fixed bed is described in this section. Due to symmetry in the radial direction of catalyst bed, the governing equations are independent of this direction. Thus, a one-dimensional model is considered. The complete set of equations for the gaseous phase, assumed to be reaction limited, may be written as [115]:

$$\frac{dF_k(z)}{dz} = A_{cat}(1-\varepsilon)R_{r,k}(z) \tag{3.1}$$

where F_k is the mole flowrate of species k, z is the distance measured from the catalyst bed inlet, A_{cat} is cross sectional area of the catalyst bed, ε is the void fraction in the catalyst bed, and $R_{r,k}$ is the reaction rate of species k. Subject to the boundary conditions (take ammonia for example):

$$F_{NH_3}(z) = 0 \tag{3.2}$$

The meaning of each variable is also listed in the Nomenclature section.

Dyson and Simon modified the Temkin expression to calculate the intrinsic rate of ammonia synthesis in mol/(m^3·s) [116], given in Equation (3.3):

$$R_{r,NH_3} = 2k_2\left[{K_a}^2 a_{N_2}\left(\frac{{a_{H_2}}^2}{{a_{NH_3}}^3}\right)^{\alpha} - \left(\frac{{a_{NH_3}}^2}{{a_{H_2}}^3}\right)^{1-\alpha}\right] \tag{3.3}$$

The parameter α is a constant, taking values between 0.5 and 0.75, and the expression of the activity of the components, a_k, is given in Equation (3.4):

$$a_k = \frac{f_k}{p^0} = \frac{\phi_k y_k p}{p^0} \tag{3.4}$$

Where ϕ_k is the fugacity coefficient of component k, y_k is the molar fraction of component k, p is the overall pressure, p^0 is the reference pressure and is assumed to be atmospheric (1 bar). Gillespie and Beattie calculated the equilibrium constant, K_a, and proposed the correlation in Equation (3.5) [117]:

$$log_{10} K_a = -2.691122\, log_{10}(T) - 5.519265 \times 10^{-5} T + 1.848863 \times 10^{-7} T^2 + \frac{2001.6}{T} + 2.689 \tag{3.5}$$

In turn, k_2 is estimated by the Arrhenius Equation [116]:

$$k_2 = 8.849 \times 10^{14} e^{\left(-\frac{40765}{1.987T}\right)} \tag{3.6}$$

3.4.2 Ammonia absorption model

This section investigates a one-dimensional mathematical model for the simulation of ammonia fixed-bed absorbent, which was numerically solved. As a temperature drop existed at the junction between the catalyst and absorbent bed, it would affect the temperature distribution

of the absorbent bed. Therefore, the PDEs for mass and energy balances of the absorbent bed were solved simultaneously using the numerical MOL. The simulation of the desorption step is also included in determining the number of absorptive reactors required to achieve a continuous ammonia production process. The main objective of this section and contribution to the research is to direct attention towards a theoretical, rather than empirical, approach to simulate the absorbent bed.

The sorbate (ammonia), mixed with unreacted hydrogen and nitrogen, comes from the outflow of the synthesis catalyst bed. As the mixed fluid continues to flow, the saturation zone of the absorbent bed moves forwards as a wave, illustrated by the breakthrough curve. This curve, an inverted S-shape, as presented in Figure 3.7(a), shows the concentration of the sorbate at different positions in the column. With time, the value of the breakthrough curve attains steady state at the end of the absorbent bed, and the outlet concentration becomes equal to that of the inlet, which indicates that the absorbent is entirely saturated. Therefore, transient mass and energy equations are necessary to simulate this process.

The following assumptions were considered in the development of the absorption model:

- The changes in volume of fluid and solid caused by temperature variations are neglected.
- The temperature of fluid into the absorbent bed is assumed to be the same as that at the outlet of the catalyst bed, which ignores the different distance setting between the catalyst and absorbent beds.
- The pressure gradient across the absorbent bed is neglected (details in Appendix A).
- There is a constant actual (interstitial) velocity, u, as the per-pass conversion of the reaction is quite low at about 5 – 7 %. Therefore, the volume change during the reaction and absorption processes was low enough to be ignored and the velocity can be assumed to be constant.
- There is an instantaneous equilibrium of the solute with the sorbate in the bulk fluid. (Some reactions are essentially instantaneous, while others may take years to reach

equilibrium. In this case, the kinetic rate of ammonia absorption is assumed to be fast and not to be the limiting step. Therefore, the equilibrium can be reached instantaneously.)

- Due to symmetry in the radial direction of the absorbent bed, the governing equations are independent of this direction. Thus, a one-dimensional model is considered.
- The ideal gas law applies.

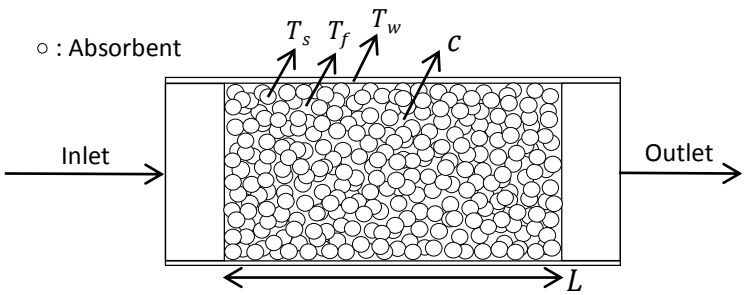

Figure 3.2. Schematic diagram of the absorbent bed configuration with significant variables.

According to the model assumptions, flow through a packed bed, displayed in Figure 3.2, may be adequately represented by the axial dispersed plug flow model [118][119], and Equation (3.7) governs the dynamic behaviour of fixed-bed absorption. Equation (3.7) predicts the concentration of solute in the bulk fluid as a function of time and location in the bed [120]:

$$-D_L \frac{\partial^2 c}{\partial z^2} + \frac{\partial (uc)}{\partial z} + \frac{\partial c}{\partial t} + \frac{1-\epsilon_b}{\epsilon_b} \frac{\partial \bar{q}}{\partial t} = 0 \tag{3.7}$$

where c is the sorbate (ammonia) concentration in the fluid phase, z is the distance measured from the column inlet, u is the fluid velocity, t is the time, and ϵ_b is the absorbent bed void fraction. In this model, the effects of all mechanisms which contribute to axial mixing are consolidated into a single effective axial dispersion coefficient, D_L. The last term accounts for the variation of $\bar{q}$, the volume-averaged sorbate loading throughout the absorbent particle, given as [120]:

$$\bar{q} = \left(\frac{3}{R_P^3}\right)\int_0^{R_P} r^2 q dr \tag{3.8}$$

where R_P is the radius of the absorbent particle, r is the radial coordinate of the absorbent pellet, and q is the sorbate loading per unit mass.

The heat balance equation for one column element (including both the fluid phase and the solid particles) can be written as [119][121]:

$$-\frac{\lambda_L}{C_f}\frac{\partial^2 T_f}{\partial z^2} + \frac{\partial\left(uT_f\right)}{\partial z} + \frac{\partial T_f}{\partial t} + \left(\frac{1-\epsilon_b}{\epsilon_b}\right)\left(\frac{C_s}{C_f}\right)\frac{\partial T_s}{\partial t} = \left(\frac{1-\epsilon_b}{\epsilon_b}\right)\left(\frac{-\Delta H}{C_f}\right)\frac{\partial \bar{q}}{\partial t} - \frac{4h_w}{\epsilon_b d C_f}\left(T_f - T_w\right) \tag{3.9}$$

where T_f, T_s, and T_w are the temperature of the fluid, solid, and column wall, respectively; λ_L is the effective axial thermal conductivity; C_f and C_s are the volumetric heat capacities for fluid and solid phases, respectively; ΔH is the enthalpy of ammonia absorption; d is the internal diameter of the absorbent bed; h_w is the overall heat transfer coefficient at the column wall.

The terms on the left side of this equation are analogous to the terms in Equation (3.7), while the terms on the right side indicate the rate of heat generation within a particle and the rate of transfer of heat to the column wall.

The heat balance for an absorbent pellet is written as [119][122]:

$$C_s\frac{\partial T_s}{\partial t} = \frac{3h}{R_p}\left(T_f - T_s\right) + \left(-\Delta H\right)\frac{\partial \bar{q}}{\partial t} \tag{3.10}$$

where h is the overall heat transfer coefficient between the absorbent particle and ammonia bulk fluid. Glueckauf proposed the linear driving force (LDF) model [123], formulating a lumped mass transfer coefficient to represent the intra-pellet diffusion rate. This is written in linear form in Equation (3.11):

$$\frac{\partial \bar{q}}{\partial t} = k_f a(c - c^*) = \frac{3k_f}{R_p}(c - c^*) \tag{3.11}$$

where a is the external surface area per unit particle volume ($3/R_p$ for spherical particles), c^* is the concentration in equilibrium with the absorbent loading q, and k_f is the external fluid film

mass transfer coefficient. The Sherwood number defined in Equation (3.47) as an appropriate dimensionless group can characterise this film mass transfer.

The model equations, together with the LDF model and effective axial thermal conductivity relation, take the following form after substituting Equation (3.11) in Equations (3.8), (3.9), and (3.10):

$$-D_L\frac{\partial^2 c}{\partial z^2}+\frac{\partial(uc)}{\partial z}+\frac{\partial c}{\partial t}+\frac{1-\epsilon_b}{\epsilon_b}\frac{3k_f}{R_p}(c-c^*)=0 \tag{3.12}$$

$$-\frac{\lambda_L}{C_f}\frac{\partial^2 T_f}{\partial z^2}+\frac{\partial\left(uT_f\right)}{\partial z}+\frac{\partial T_f}{\partial t}+\left(\frac{1-\epsilon_b}{\epsilon_b}\right)\left(\frac{C_s}{C_f}\right)\frac{\partial T_s}{\partial t} \tag{3.13}$$

$$=\left(\frac{1-\epsilon_b}{\epsilon_b}\right)\left(\frac{-\Delta H}{C_f}\right)\frac{3k_f}{R_p}(c-c^*)-\frac{4h_w}{\epsilon_b d C_f}\left(T_f-T_w\right)$$

$$C_s\frac{\partial T_s}{\partial t}=\frac{3h}{R_p}\left(T_f-T_s\right)+(-\Delta H)\frac{3k_f}{R_p}(c-c^*) \tag{3.14}$$

with boundary and initial conditions:

$$At\ t=0;\ c=0\ ;\ T_f=\ T_s=T_0;\ 0\le z\le L \tag{3.15}$$

$$At\ z=0;\ c=c_F;\ T_f=\ T_s=T_0$$

$$\left.\frac{\partial c}{\partial z}\right|_{z=L}=0;\ \left.\frac{\partial T_f}{\partial z}\right|_{z=L}=0$$

The heat capacity of the fluid and solid phases' changes caused by temperature variation, as described in Section 3.4.4.3.

The current desorption model assumes an isothermal system. It also assumes that there is no pressure gradient during intra-particle diffusion. The only driving force is the difference in concentration with the gas. Therefore, the transport equation used in the current absorbent bed study is the same as Equation (3.12); however, with different initial and boundary conditions:

$$At\ t=0\quad c=0\quad for\ 0\le z\le L \tag{3.16}$$

$$At\ z=0;\ c=0;\ \left.\frac{\partial c}{\partial z}\right|_{z=L}=0$$

3.4.3 The coupling between the catalyst and absorbent beds

The governing equations for the connection between the catalyst and absorption beds are presented in this section. If the flow across the reactor has an ideal plug flow pattern, coupling a consecutive absorption bed should not alter the per-pass reaction conversion, as ammonia absorbed in the absorption bed cannot affect the reaction in the preceding catalyst bed. However, an increase in conversion was observed in our experiments. Thus, it was hypothesised that the flow regime was not ideal plug flow, but rather an intermediate between plug flow and perfect mixing, i.e. backflow existed within the reactor. In this research, the concept of backflow is accepted to explain the experimental observations that an adjacent coupling of an absorbent bed increases the catalyst bed performance. The phenomenon of gas backflow was observed in steady-state tracer injection tests, in which a tracer is injected continuously at one location, and its concentration is monitored upstream of the injection point [124]. The backflow is caused by the instability of fluid systems. A schematic diagram of this phenomenon is presented in Figure 3.3:

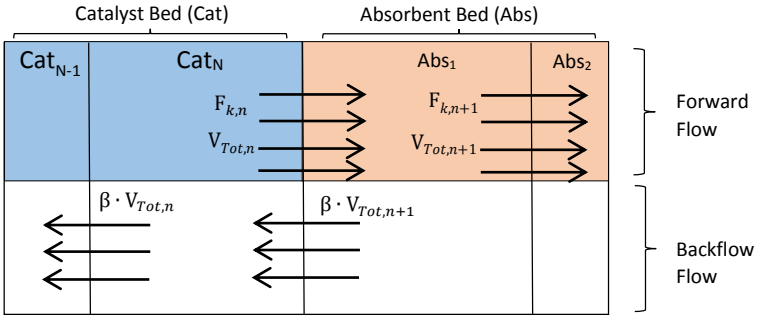

Figure 3.3. Schematic of backflow in an adjacent coupling catalyst-absorbent bed (F_k is the flowrate in mol/s, while V_{Tot} is the flowrate in m^3/s).

A backflow fraction, expressed by β (a β of zero is the plug flow; while when β equals infinity, it gives the perfect mixing), is proposed for all components – hydrogen, nitrogen, and ammonia. To represent the effect of absorption in the mathematical model, we propose the use of a hypothetical recycle stream as a modelling assumption to associate the absorption effect on

the per-pass conversion results. The schematic diagram of the hypothetical recycle stream model, which represents the connection between the catalyst and absorbent beds, is depicted in Figure 3.4(a). Bitsch et al. used to propose a plug flow tubular reactor with loop model for the simulation of backflow on reversible addition-fragmentation chain transfer polymerization [125]. That recycle-tube model, similar to the recycle stream model, controls the degree of backflow through the percentage recycle of flow. It has been observed that the ammonia conversion is higher for catalyst-absorbent coupled at a closer distance between the catalyst and absorption beds. Therefore, we hypothesise that the degree of backflow decreases as the distance between the catalytic and absorption beds increases. In this model, the backflow was assumed to happen between the catalyst section and absorption section. The hypothetical recycle fluid amount is set as R_s, which corresponds to the backflow fluid flowrate $\beta \cdot V_{Tot}$. As a hypothetical recycle stream was involved, the steady-state mass balance should be calculated using iterative methods.

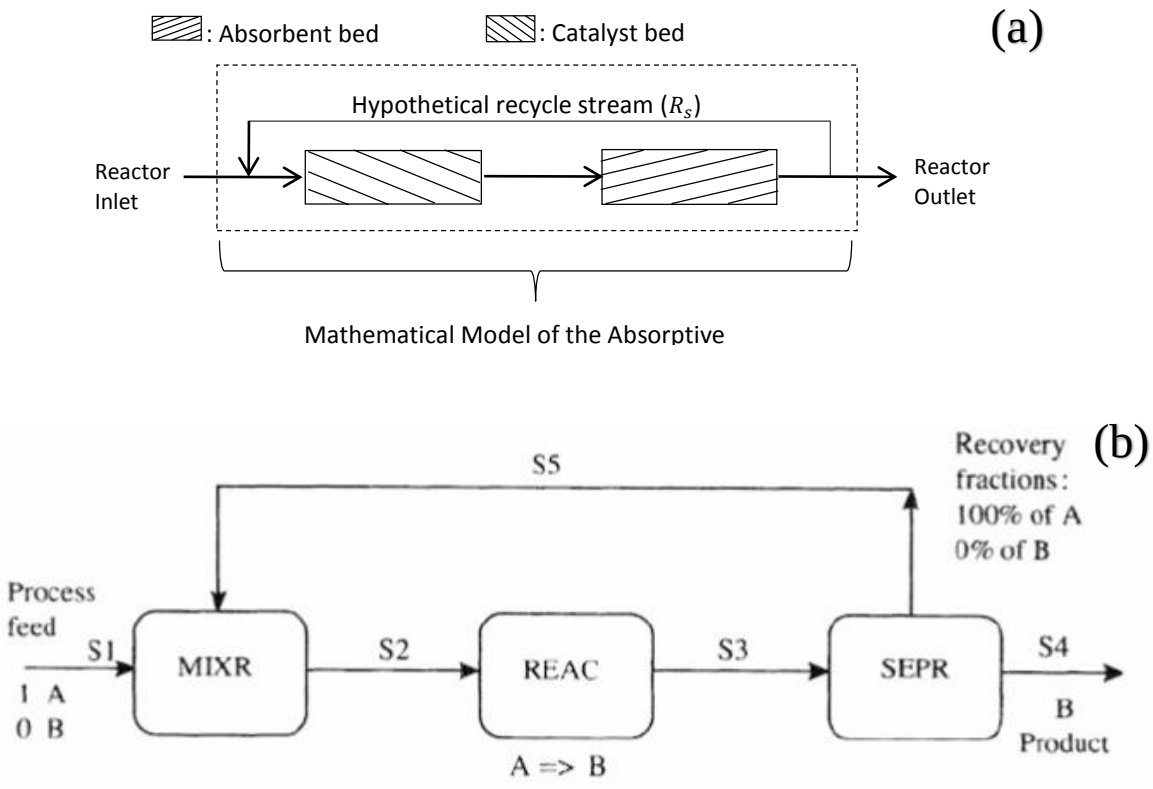

Figure 3.4. (a) Schematic of the hypothetical recycle of the reactor in order to model backflow. (b) Process with recycle [126].

The absorptive reactor has ammonia conversion of X, while the separation of ammonia is assumed to be complete. The unreacted hydrogen and nitrogen are recycled. Then, the steady-state mass balance of the mixer in Figure 3.4(b) should satisfy the relationship shown in Equation (3.17), where 1.0 represents the reactor inlet without recycling [126]. The conversion cannot be zero in this relationship.

$$R_s = (1 - X) * (1.0 + R_s) \tag{3.17}$$

R_s is the amount of nitrogen or hydrogen in the recycle stream in this case. Then repeat the process over and over. It is necessary to set an error tolerance; the procedure can take many iterations to converge to the steady-state within the tolerance. After 10 iterations, the difference of the value of recycle when starting an iteration and the value when ending the iteration is within the allowable error, then stop the process. A demonstration is given in Table 3.2, which is not the actual simulation data as the actual recycle times in the simulation is high.

Table 3.2. Mass balance with recycle.

Iteration Number	Feed, S1	Recycle, S5.	Into Reactor, S2.	Out of Reactor, S3.	Recycle, S5.
1	1	0	1	0.5	0.5
2	1	0.5	1.5	0.75	0.75
3	1	0.75	1.75	0.875	0.875
4	1	0.875	1.875	0.9375	0.9375
5	1	0.9375	1.9375	0.9687	0.9687
10	1	0.9980	1.9980	0.9990	0.9990

3.4.4 Parameter values

This model is specific for ammonia absorption in a $MgCl_2$ absorbent bed. The parameters used in this simulation pronounced are determined in this section. All properties with sub ‘mix’ in this

section refer to the fluid mixture of hydrogen, nitrogen and ammonia and depend on the composition which are assumed to be the same as the initial condition to simplify the simulation.

3.4.4.1 Dimensionless groups

The mass transfer and heat transfer coefficients are estimated from the relationship of several dimensionless groups, including the Reynolds, Schmidt, and Prandtl Numbers.

Reynolds Number:

$$Re = 2R_p \rho_{mix} u / \mu_{mix} \tag{3.18}$$

where R_p is the absorbent pellet radius, μ_{mix} is the viscosity of the fluid mixture, ρ_{mix} is the density of the fluid mixture, and u is the velocity of the fluid.

Schmidt Number:

$$Sc = \mu_{mix} / \rho_{mix} D_m \tag{3.19}$$

where D_m is the mass diffusivity, μ_{mix} is the dynamic viscosity of the fluid mixture, and ρ_{mix} is the density of the fluid mixture.

Prandtl Number:

$$Pr = C_{f,mix} \mu_{mix} / \lambda_{mix} \tag{3.20}$$

where $C_{f,mix}$ is the volumetric heat capacity of the fluid mixture, μ_{mix} is the dynamic viscosity of the fluid mixture, and λ_{mix} is the thermal conductivity of the fluid mixture.

3.4.4.2 Viscosity

Several properties of the fluid in the absorbent bed are needed for the dimensionless groups. This section focuses on the viscosity of the fluid mixture (hydrogen, nitrogen and ammonia) using Chung et al.'s method [127].

$$\mu_{mix} = \mu^* \frac{36.344(M_m T_{cm})^{\frac{1}{2}}}{{V_{cm}}^{\frac{2}{3}}} \tag{3.21}$$

$$\mu^* = \frac{(T^*)^{0.5}}{\Omega_v}\{F_c[{G_2}^{-1} + E_6 y]\} + \mu^{**} \tag{3.22}$$

$$\mu^{**} = E_7 y^2 G_2 exp[E_8 + E_9 (T^*)^{-1} + E_{10}(T^*)^{-2}] \tag{3.23}$$

$$\Omega_v = A(T^*)^{-B} + C\, exp(-DT^*) + E\, exp(-FT^*) \tag{3.24}$$

$$G_2 = \frac{E_1\left\{\frac{[1 - exp(-E_4 y)]}{y}\right\} + E_2 G_1\, exp(E_5 y) + E_3 G_1}{E_1 E_4 + E_2 + E_3} \tag{3.25}$$

$$F_c = 1 - 0.2756\omega_m + 0.059035\, {\eta_{rm}}^4 \tag{3.26}$$

$$\omega_m = \frac{\sum_i \sum_j y_i y_j w_{ij} {\sigma_{ij}}^3}{{\sigma_m}^3} \tag{3.27}$$

$$\eta_{rm} = 131.3 \frac{\eta_m}{(V_{cm} T_{cm})^{0.5}} \tag{3.28}$$

$${\eta_m}^4 = {\sigma_m}^3 \sum_i \sum_j \frac{y_i y_j {\eta_i}^2 {\eta_j}^2}{{\sigma_{ij}}^3} \tag{3.29}$$

$$y = \frac{\rho_m V_{cm}}{6} \tag{3.30}$$

$$G_1 = \frac{1 - 0.5y}{(1 - y)^3} \tag{3.31}$$

$$E_i = a_i + b_i \omega_m + c_i {\eta_{rm}}^4 \tag{3.32}$$

$$T^* = 1.2593 \frac{T}{T_{cm}} \tag{3.33}$$

The calculations of the hard-sphere equivalent diameter, the molecular weight of the fluid mixture, and density of mixture are also presented in Appendix A. Constants in Equation (3.24), dipole moments of N_2, H_2 and NH_3, and constants for E_i are listed in Appendix A [127].

3.4.4.3 Heat capacity

The individual heat capacity at constant pressure is calculated using the polynomial Shomate equation [128]:

$$C_{pk} = A + Bt + Ct^2 + Dt^3 + \frac{E}{t^2} \tag{3.34}$$

where $t = T/1000$. C_{pk} is the heat capacity of i in J/K, which is nitrogen, hydrogen, ammonia, or magnesium chloride. A, B, C, D, and E are parameters shown in Table 3.3. The values for ${N_2}^1$ are for nitrogen at 100–500 K, while those for ${N_2}^2$ are for temperatures higher than 500 K.

Table 3.3. Parameters for the heat capacity equation.

i	A	B	C	D	E
${N_2}^1$	28.986	1.854	-9.648	16.635	0.00017
${N_2}^2$	19.5	19.88	-8.59	1.369	0.5276
H_2	33.066	-11.363	11.433	-2.772	-0.1585
NH_3	20	49.77	-15.376	1.9212	0.189
$MgCl_2$	78.30733	2.435888	6.858873	-1.728967	-0.729911

The fluid through the absorbent bed is a mixture. Therefore, the heat capacity of the fluid at constant pressure is given by:

$$C_{fm} = \sum_{i=1}^{n} y_k \, C_{p,k} \tag{3.35}$$

where y_k is the fraction of species k: nitrogen, hydrogen, or ammonia.

3.4.4.4 Thermal conductivity

$$\lambda_{mix} = \frac{31.2\mu_m^0 \psi}{M_m/10^3}(G_2^{-1} + B_6 y) + qB_7 y^2 T_{r,m}^{1/2} G_2 \tag{3.36}$$

The low-pressure mixture gas viscosity, μ_m^0, was obtained from the Chung et al. correlation in Equation (3.37):

$$\mu_m^0 = \frac{26.69 F_c (M_m T)^{\frac{1}{2}}}{{\sigma_m}^2 \Omega_v} \tag{3.37}$$

in which Ω_v is as defined in Equation (3.24), and F_c is as defined in Equation (3.26).

The parameter ψ is given by:

$$\psi = 1 + \alpha\left\{\frac{0.215 + 0.28288\alpha - 1.061\beta + 0.26665Z}{0.6366 + \beta Z + 1.061\alpha\beta}\right\} \tag{3.38}$$

$$\alpha = \left(\frac{C_{p,m} - R}{R}\right) - \frac{3}{2}$$

$$\beta = 0.7862 - 0.7109\omega_m + 1.3168{\omega_m}^2$$

$$Z = 2.0 + 10.5T_{r,m}^2$$

The parameters q, y, B_i, and G_i are given by Equation (3.39):

$$q = 3.586 \times 10^{-3} \frac{\left(\frac{T_{c,m}}{M_m/10^3}\right)^{\frac{1}{2}}}{{V_{c,m}}^{\frac{2}{3}}} \tag{3.39}$$

$$y = \frac{V_{c,m}}{6V_m}$$

$$G_1 = \frac{1 - 0.5y}{(1-y)^3}$$

$$G_2 = \frac{(B_1/y)[1 - exp(-B_4 y)] + B_2 G_1\, exp(B_5 y) + B_3 G_1}{B_1 B_4 + B_2 + B_3}$$

$$B_i = a_i + b_i\omega_m + c_i{\mu_{rm}}^4$$

Coefficients for B_i are given in Appendix A [127].

To establish a relationship between the mass and heat transfer coefficients, an analogy between Schmidt number and Prandtl number was accepted, and it was assumed that the convective transport of heat and mass occur through the same mechanism (Reynolds Analogy, a similarity based approach, which relates turbulent momentum and heat transfer). Schmidt number is a dimensionless number defined as the ratio of momentum diffusivity and mass diffusivity, shown in Equation (3.19). Prandtl number is the ratio of momentum diffusivity to thermal diffusivity, given by Equation (3.20). Therefore, the relationship between the mass and thermal diffusivities is assumed to be given in Equation (3.40).

$$\lambda_f = C_f D_m \tag{3.40}$$

Similarly, the relationship between the overall mass and heat transfer coefficients, based on the analogy between the Nusselt number and Sherwood number, is given in Equation (3.41):

$$h = k_f C_f \tag{3.41}$$

The effective axial thermal conductivity is given by [119]:

$$\lambda_L = C_f D_L \tag{3.42}$$

where C_f is the volumetric heat capacity of the fluid phase, and D_L is the axial dispersion coefficient.

3.4.4.5 Axial dispersion coefficient

Disregarding effects caused by non-uniformity of packing, there are two main mechanisms, which contribute to axial dispersion: molecular diffusion and turbulent mixing (the turbulent mixing effect can be neglected in this project as the gaseous flow was laminar) of flows around the absorbent particles. These effects are additive to a first approximation, such that the dispersion coefficient may be represented by [119]:

$$D_L = \gamma_1 D_m + \gamma_2 2R_p u \tag{3.43}$$

where γ_1 and γ_2 are constants, which are normally valued at approximately 0.7 and 0.5, respectively. D_m is the mass diffusivity of ammonia in the mixture, which is taken as $2*10^{-10}$ m^2/s [23]. The effect of temperature on diffusion is given by [127]:

$$D \propto T^2 \tag{3.44}$$

Therefore, we can assume that

$$\frac{D_{m1}}{D_{m2}} = (\frac{T_1}{T_2})^2 \tag{3.45}$$

3.4.4.6 Heat transfer coefficient

The Nusselt number is given by [119]:

$$Nu = 2 + 1.1\, Re^{0.6} Pr^{1/3} = \frac{2R_p h}{\lambda_m} \tag{3.46}$$

3.4.4.7 Mass transfer coefficient

The Sherwood number is given by [119]:

$$Sh = 2 + 1.1\, Re^{0.6} Sc^{1/3} = \frac{2R_p k_f}{D_m} \tag{3.47}$$

Table 3.4 displays the model parameters in the simulation. The mass and heat transfer coefficients depend not only on the temperature of the fluid but also on the composition of the mixture. The inlet of the absorbent bed comes from the outlet of the Haber-Bosch reactor (after the catalyst bed). Furthermore, the change in composition is small, as the concentration of ammonia is low. Therefore, the effect of the mixture composition on the coefficients can be neglected. As shown in Figure 3.5, the mass and heat transfer coefficients increase as the temperature increases. This relationship is based on Equations (3.46) and (3.47).

Table 3.4. Model parameters used in the simulation.

Parameter	Description	Value
d	Internal diameter of absorbent bed, m	0.008
D_m	Mass diffusivity, m^2/s	$2*10^{-10}$ [129]
D_L	Axial dispersion coefficient, m^2/s	$2*10^{-6}$
h_w	Heat transfer coefficient at the column wall, $W/(m^2*K)$	0.12 [119]
ΔH	Enthalpy of ammonia absorption, kJ/mol	-87
p	Pressure, bar	50
R	Gas constant, J/(mol*K)	8.314
R_p	Absorbent pellet radius, m	$2*10^{-4}$
$T_{0,f}$	Initial temperature of fluid, K	743
$T_{0,s}$	Initial temperature of absorbent pellet, K	423
T_w	Temperature of absorbent column wall, K	423
u	Fluid velocity, m/s	0.01
ϵ_b	Absorbent bed void fraction	0.4

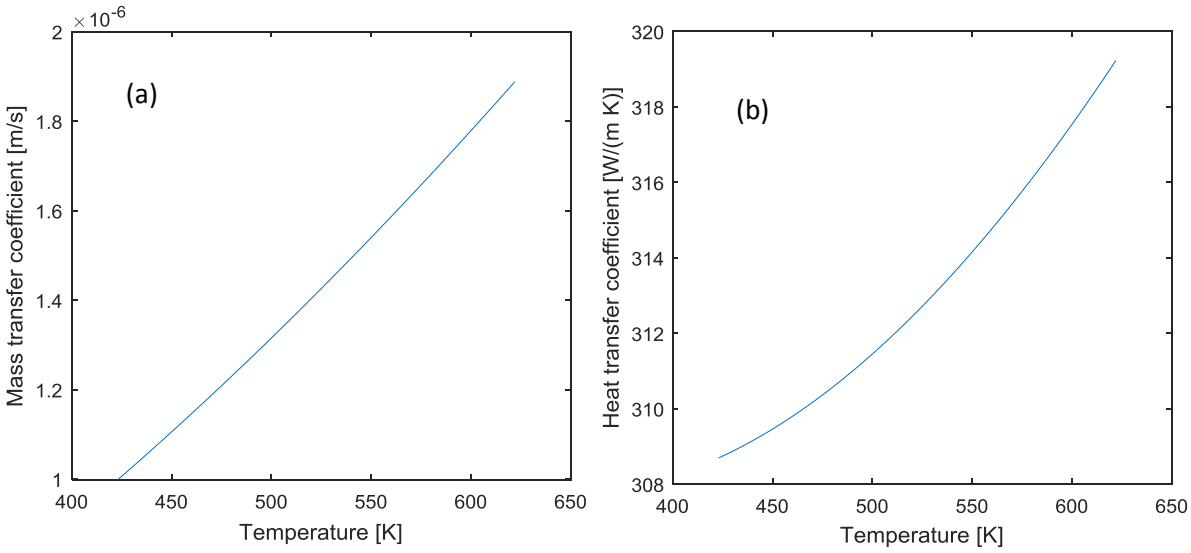

Figure 3.5. Relationship between (a) mass and (b) heat transfer coefficients with temperature.

3.5 Numerical simulation and discussion

The increase in conversion of ammonia synthesis in the presence of absorbents was studied in a bench-scale fixed-bed tubular reactor. The governing equations of ammonia production in the absorptive reactor model consist of a set of differential-algebraic equations, i.e. the mass balance with their boundary conditions. The simulation was based on the same operating conditions as the experimental setting. To solve the aforementioned equations at the steady-state condition, the Runge-Kutta-Fehlberg method was applied. During the iteration of the mass balance equation, the values of components flowrate and ammonia concentration were recorded. The result of the catalyst bed model is displayed in Figure 3.6:

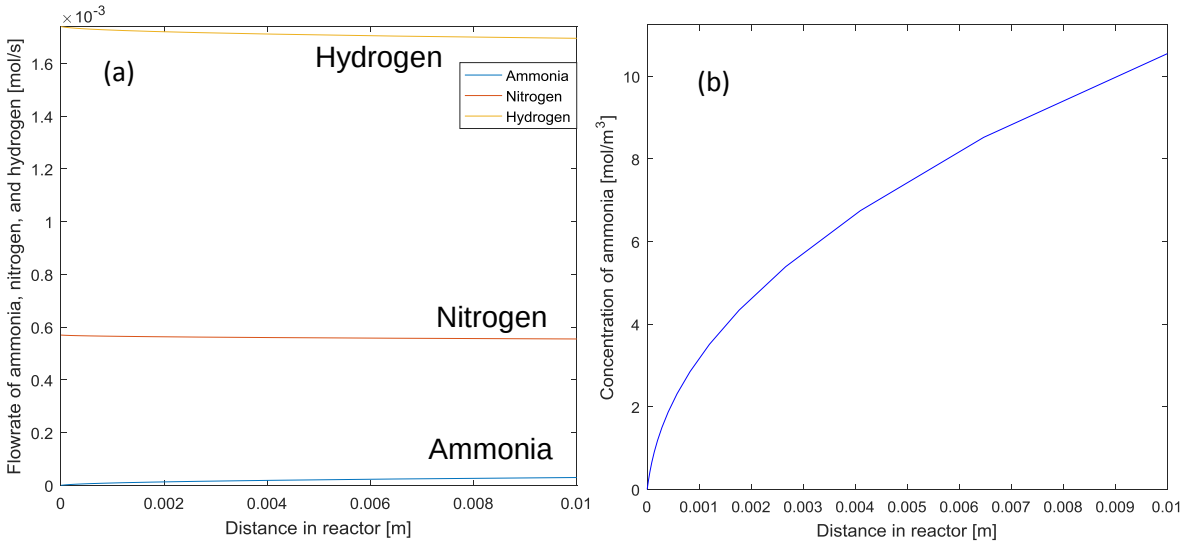

Figure 3.6. (a) Flowrate of components in the catalyst bed. (b) The concentration of ammonia in the catalyst bed, calculated with the catalyst at 743 K. A 3:1 mixture of H_2: N_2 at 50 bar and a weight hourly space velocity of 31,200 mL $g^{-1}h^{-1}$ were used.

The flowrate of the components along the catalyst bed within 0.01 meters was calculated using MATLAB (0.01-meter catalyst bed in the bench-scale reactor). Figure 3.6 (a) depicts the flowrate of the three components of the reaction. It is evident from Figure 3.6 (b) that the reaction equilibrium was not achieved at a reactor length of 0.01 m, as the concentration of ammonia was still increasing at the end of the reactor. It is worth noting that this is the main reason for the low conversion values of the laboratory results. From the modelling results, the conversion was calculated using Equation (3.48):

$$Conversion\ of\ reaction\ X = \frac{Moles\ of\ N_2\ reacted}{Moles\ of\ N_2\ fed} = \frac{F_{N_2,0} - F_{N_2}}{F_{N_2,0}} \qquad (3.48)$$

For the fixed-bed absorbent, the non-isothermal mathematical model considers both temperature and flow rate changes caused by ammonia absorption and is, therefore, more general than isothermal models. It provides a useful representation of the behaviour of breakthrough curves and temperature profiles for ammonia in an absorbent packed bed. Sets of PDEs for the mass and energy balances in the absorbent bed were solved in MATLAB using the numerical MOL. Equations (3.12), (3.13), and (3.14) were first discretised in space via the

classical five-point, fourth-order finite difference approximation, then reduced to a set of ordinary differential equations (ODEs). The resulting ODEs in time were then integrated using the ode15s solver from MATLAB. Ode15s was an appropriate solver due to the highly stiff nature of the PDEs, with sharp concentration and temperature fronts. The parameters used for solving the absorption-desorption equations are detailed in Section 3.4.4.

The results from the non-isothermal fixed-bed absorption model are presented in Figures 3.7 and 3.8. Equations (3.12), (3.13), and (3.14) were selected as the governing equations for the ammonia concentration and temperature profiles of absorbent and bulk temperature, respectively. Figure 3.7(a) displays typical breakthrough curves as a function of distance through the absorbent bed for different times. The inverted S-shape front lines in Figure 3.7(a) illustrate that the concentration decreases in the absorbent bed at each time point and that the breakthrough curve moves right as time progresses. Upstream from the front, the absorbent is saturated, and, therefore, the concentration of ammonia is that of the feed. In turn, downstream from the front, the concentration of the solute in the fluid is nearly zero, because the ammonia is almost completely absorbed. Figure 3.7(a) reveals that, as time increases, the steepness of the breakthrough curve decreases. Meanwhile, there is a slight rise of C/C_F at the further end of the absorption bed as time passes, shown in Figure 3.7(a). In the governing equation of solute concentration Equation (3.12), the mass transfer coefficient k_f is influenced by the temperature of fluid, calculated from Equation (3.47). As the absorption progress, the temperature of column element increased, which leads to an increase of the mass transfer coefficient, however, a negative effect on the $\frac{\partial c}{\partial t}$, therefore, the C/C_F rises at the further end of the absorption bed.

As depicted in Figure 3.7(b), the temperature of the absorbent quickly increases and drops because of heat transfer from the hot fluid passing through, then experiences a slight increase caused by heat released from absorption. It eventually reaches a relatively stable level. At a certain time, corresponding to each line in Figure 3.7(c), the temperature decreases caused by the heat transfer with solid and heat lost at the wall, then immediately rises to a plateau because of the exothermic absorption. It remains at this level because of the absorption zone

not moving further at the given time. The final steady-state ammonia temperature for each time step decreases caused by heat loss at the wall, as intuitively interpreted in Figures 3.7(b) and 3.7(c).

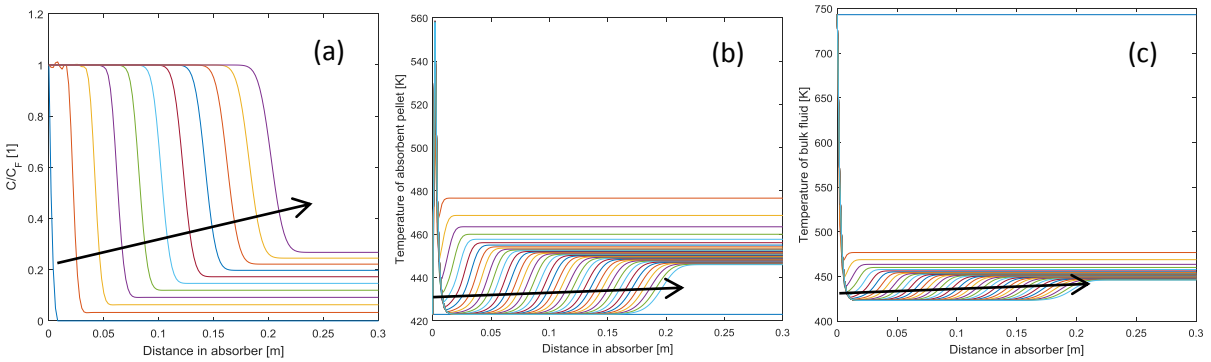

Figure 3.7. (a) Breakthrough curves of ammonia, (b) temperature profiles of absorbent pellets, and (c) temperature profiles of bulk fluid (arrows point in the direction of increasing time from 0 to 20 minutes) calculated with the absorbent at 423 K at the beginning.

Figure 3.8 presents the concentration and temperature profiles in the absorbent bed at different times. Each line in Figure 3.8(a) indicates that ammonia is almost entirely absorbed at first when the concentration is nearly zero at the exit of the absorbent bed. In turn, the bed is nearly saturated after some time and can no longer absorb ammonia, which leads to the concentration equalling that of feed. The curves move to the right, and the breakpoint time increases from 2 to 20 minutes. Similarly, the absorbent temperature in Figure 3.8(b) first increases when the absorption is releasing heat and heat is transferred from hot fluid and falls when the absorbent becomes saturated; furthermore, there is only heat loss at the wall until the equilibrium is reached (temperature of column wall). The higher temperature for each line shifts to the right as the position in the absorbent bed moves. Moreover, the temperature wave is decreasing caused by heat loss at the wall. However, the bulk temperature, as depicted in Figure 3.8(c), first decreases, even when absorption is releasing heat, because of the heat loss from the wall and heat transfer from the hot fluid to the absorbent solid. The further temperature decreases

(the second decrease/drop) when the absorption is finished. This temperature also reaches an equilibrium (temperature of the column wall) after some time.

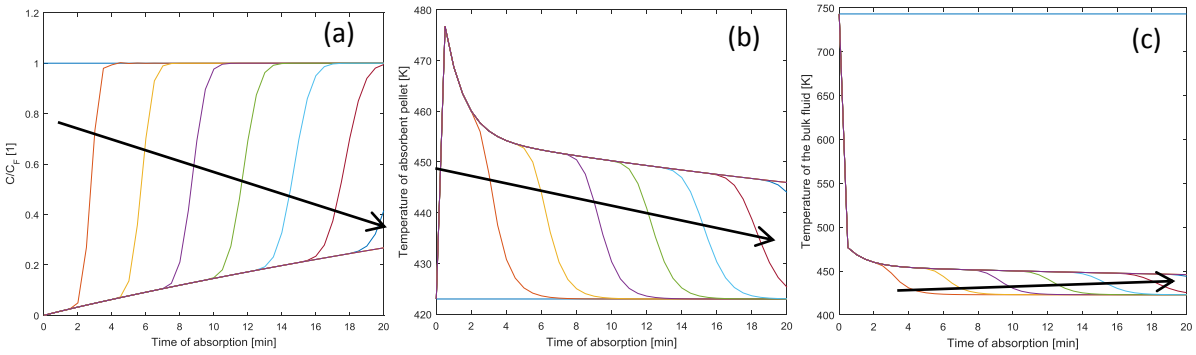

Figure 3.8. (a) Concentration of ammonia, (b) temperature profiles of absorbent pellets and (c) temperature profiles of bulk fluid (arrows point in the direction of increasing distance from 0 to 0.3 meter), calculated with the absorbent at 423 K at the beginning.

Figure 3.9 displays the temperature difference between particles and fluid. The temperature difference only exists at the beginning, as the heat transfer between them is rapid. Moreover, it ultimately reaches a steady level. As the temperature difference between solid and fluid is negligible – 10^{-4} – the temperature difference between the absorbent pellets and fluid can be neglected.

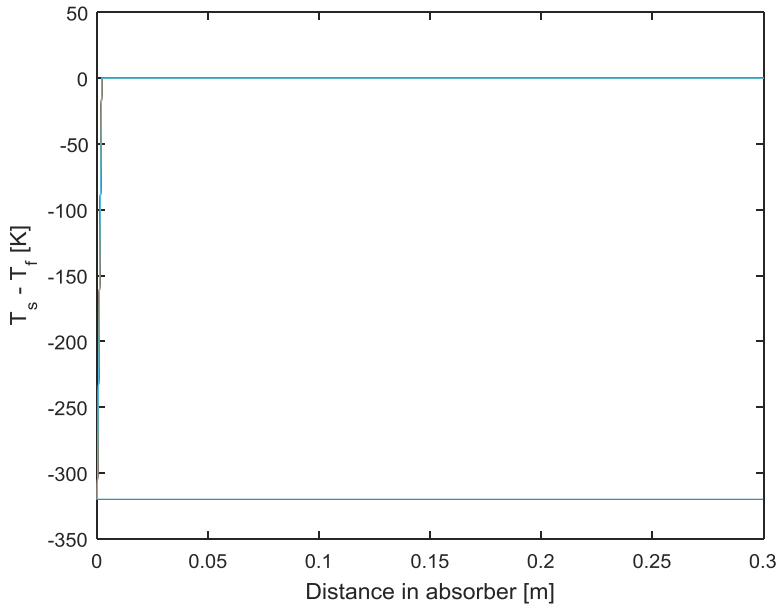

Figure 3.9. The temperature difference between fluid and solid in the absorbent bed.

Figure 3.10 displays the process of ammonia desorption from the absorbent particles. During regeneration, the operating condition maintains a high temperature (400 ˚C), leading to a reduction in the ammonia storage capacity of the absorbent with ammonia released to the gas phase. The driving force for desorption only depends on the difference in ammonia concentration between absorbent particles and the gas phase. As desorption progresses, this difference is reduced. The desorption rates (i.e. the curve slopes in Figure 3.10) markedly decrease. Moreover, given that the time needed for desorption is longer than for absorption (as ammonia is strongly absorbed), the number of absorptive reactors should be greater than two to achieve continuous ammonia production.

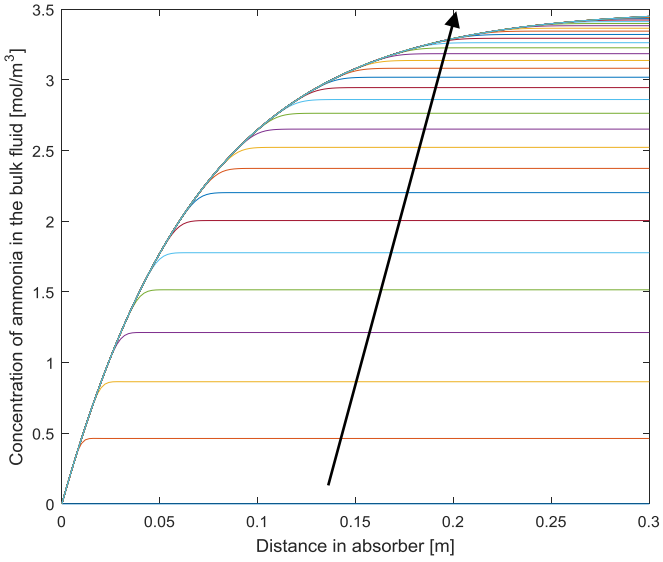

Figure 3.10. Concentration profiles of ammonia in the bulk fluid concerning the distance at different times for the desorption process (arrow points in the direction of increasing time from 0 to 40 minutes).

The simulation results based on the $MgCl_2$ absorbent, particularly those reported in Figure 3.7(a), qualitatively agree with the experimental breakthrough curves for ammonia absorption on $MgBr_2$ [130]. As an example, Figure 3.11 demonstrates the effect of CO_2 concentration in the flue gas on the temperature profile of the absorption column, one typical result of absorption

column modelling in [131]. Chemical absorption for CO_2 capture from different gas streams by solid particles is a bulk chemical reaction in solid phase. In particular, solid sorbent materials have been proposed for capturing CO_2 through a reversible chemical transformation. CO_2 reacts with MEA (an organic chemical compound), which is an exothermic reaction. Therefore, flue gas with high CO_2 concentration exhibits a higher peak in the temperature profile of the absorption column, similar to Figure 3.8(b). This is because of more CO_2 exothermic absorption in the amine solution and more heat release resulting in an increase in the overall temperature of the absorption column. Besides, after most of the CO_2 in the gas stream is absorbed in the amine solution, the temperature starts to decrease due to the evaporation of water [131], while, in the model, this occurs because of heat transfer at the wall. Consequently, we can conclude that this model can fit real experimental results. Future experiments should obtain the value of these parameters for specific ammonia absorbents to achieve a suitable match between the model and reality.

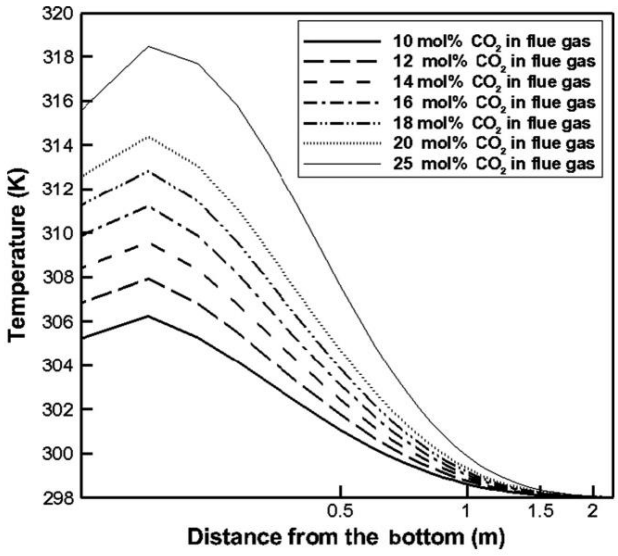

Figure 3.11. Temperature profile of the absorption column for different CO_2 concentrations in flue gas [131].

The mathematical model for the fixed-bed reactor combining absorption and reaction was validated with experimental data. In this case, the backflow is introduced in terms of a hypothetical recycling ratio. The results from the mathematical model are displayed in Figure 3.12. Figure 3.12(a) presents the flowrate of ammonia, and 3.12(b) indicates the concentration of ammonia in the bulk fluid in the longitudinal direction of the reactor coupled with the magnesium chloride absorbent bed under various backflow degrees represented by a hypothetical recycle fraction from 0 to 100% (arrow pointing in an increasing direction).

As indicated in Figure 3.12(a), as expected, the flowrate of ammonia increased as the backflow increased (caused by higher hypothetical gas recycling). Figure 3.12(b) presented that the concentration of ammonia decreased because of the absorption, which could promote the ammonia synthesis reaction. Then, the per-pass reaction conversion improved. At 470 ˚C the thermodynamic equilibrium was typically equivalent to about 13% ammonia conversion from H_2: N_2 = 3:1 under 50 bars total pressure [132]. Our model conversion without the absorbent was 5.70% – much lower than that of the equilibrium value. Therefore, the improvement in the per-pass reaction conversion was probably not because the reaction equilibrium was driven, but mainly because of the backflow created by the absorption bed. The backflow may have enhanced ammonia production caused by higher hypothetical gas recycling or a higher reaction rate when ammonia was absorbed. Ammonia absorption led to a lower concentration of ammonia, as shown in Figure 3.12(b). According to Equation (3.3), the reaction rate was faster as the partial pressure of ammonia decreased. Therefore, the per-pass reaction conversion was higher even when the reaction thermodynamic equilibrium was not reached.

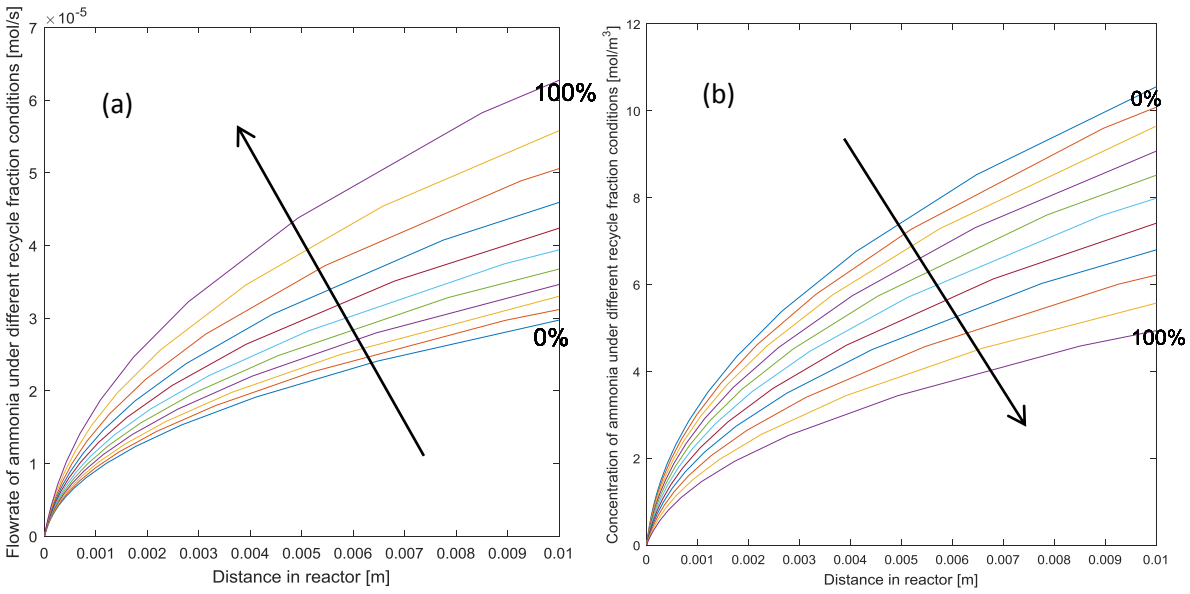

Figure 3.12. (a) Flowrate and (b) concentration of ammonia in a coupled catalyst and $MgCl_2$ absorbent bed reactor operating at different recycling fractions.

The relation between per-pass ammonia-synthesis conversion and backflow degree can be given based on the model results presented in Figure 3.13 for the $MgCl_2$ absorbent.

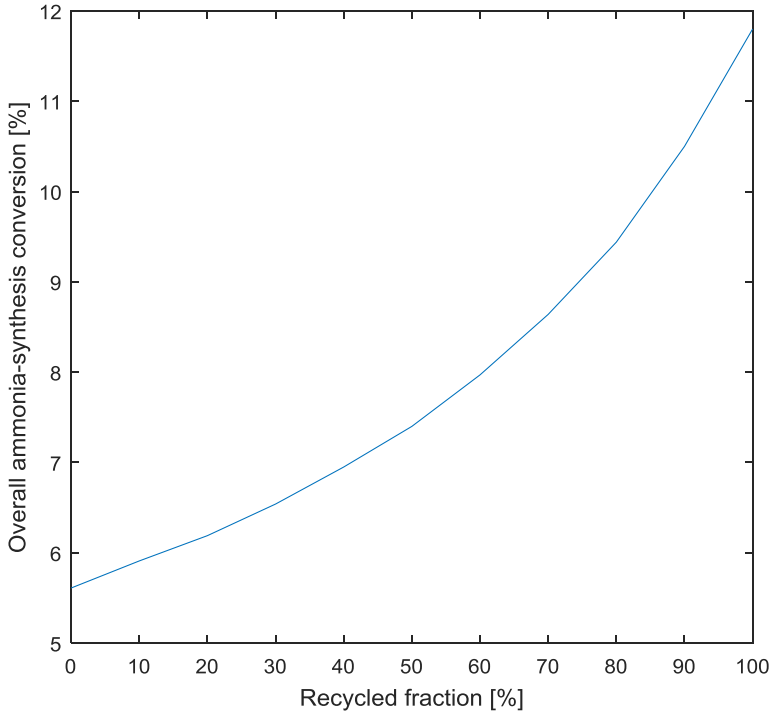

Figure 3.13. Simulation result of the relation between the per-pass reactor conversion and recycle fraction (representing the degree of backflow) in the absorptive reactor.

Based on experimental data in the absorption-enhanced reactor, the per-pass conversions are 9.33%, 6.89%, and 4.59% at 0.0, 5.0, and 10.0 cm packing separation between the catalyst and absorbent beds, respectively. As the packing distance increases, the improvement on the per-pass conversion decreases. In this simulation, the concept of backflow is adopted to explain the effect of adjacent-coupling absorption on improved ammonia synthesis per-pass conversion. The placement of the absorbent bed below the catalyst bed could create backflow, while the backflow fraction is related to the packing distance. And the increased packing distance leads to a decreased backflow fraction. The simulation results indicate that the reaction conversion similarly decreases when the backflow fraction decreases. One thing is for certain: the position of the absorbent can influence the improvement of conversion. The closer absorbent and catalyst beds are to each other, the more of an improvement there is on the conversion. Therefore, the numerical solution for the absorption-enhanced ammonia-synthesis reactor model can be an approximation to the experimental results. It is concluded that the absorption of ammonia can influence the reaction conversion, which because backflow may widen the residence time distribution and increase the reaction rate. Take the tank in series model of residence time distribution as an example, the idealness of the residence time distribution is represented by the number of CSTR tanks used (N in Figure 3.14). A large number of tanks indicates an ideal plug flow reactor ($N \rightarrow \infty$), and a small number leads to a CSTR reactor ($N = 1$). The large backward flux indicates fast material exchange between adjacent tanks. In an ideal plug flow reactor the fluid particles do not mix with those in front and behind. However, the real system in this research is not ideal plug flow. The ammonia absorbed will affect the reaction in front. Therefore, the backflow in the absorptive reactor caused wider distribution which means that the decreased ammonia concentration due to absorption will have an impact on the overall ammonia conversion.

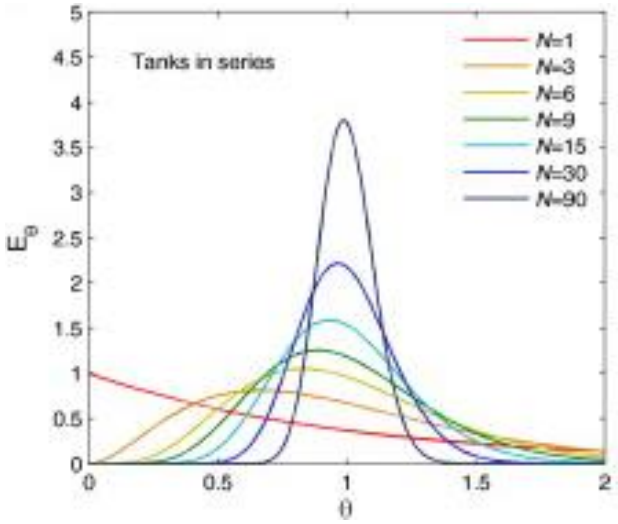

Figure 3.14. E curves (the distribution of exit times) of residence time distribution model: tank in series [133].

The measured conversion without absorbent was 4.31% (Table 3.1), much lower than the equilibrium value of 13%. In this chapter, the increase in the ammonia conversion was under the kinetic controlled regime. The placement of an absorbent bed after the catalyst bed could create backflow, which is equivalent to the effect of gas recycling including the effect of ammonia absorption. Thus, under the kinetic controlled regime, the lower ammonia partial pressure result in higher ammonia conversion approaching the thermodynamic equilibrium.

Although ammonia synthesis is exothermic (the enthalpy of ammonia production (ΔH) is -45.7 kJ·mol^{-1} [132]), the released energy had been neglected in this simulation as the amounts are very small. From the experimental data, the ammonia production rate is 30,000 μmolg^{-1}h^{-1} under a 3:1 mixture of H_2: N_2 at 50 bar and a weight hourly space velocity of 31,200 mL g^{-1}h^{-1}. For 100 mg iron catalyst, it is 3,000 μmolh^{-1}. Therefore, the heat released is:

$$Q_{rxn} = -45.7 \times 10^3 \times 3000 \times 10^{-6} = -137.1\, J \cdot h^{-1} = -0.04\, W$$

Assume that the room temperature is 25 °C, and the thickness of reactor wall is assumed to be ignored. Therefore, the heat loss [134] during the ammonia synthesis process is:

$$Q_{loss} = h_w A_{column}\left(T_{surface} - T_{air}\right) = 0.12 \times 0.0157 \times (400 - 25) = 0.71\, W$$

Compared with the heat loss on the wall, the heat released from ammonia production can be

neglected. The heating system of the reactor needs to provide additional energy, $0.67\,W$, to keep the catalyst bed at constant temperature.

The catalyst and absorbent beds were regarded as two separate blocks in the simulation, and only a hypothetical recycle stream linked these two beds. The temperatures for the two beds were set at a different value. However, the fluid coming from the catalyst bed at 470 ˚C flows into the absorbent bed at a higher temperature than the intended 150 ˚C, which would influence the temperature profile in the absorbent bed. We tried to keep the catalyst and absorbent beds operating isothermally. However, there still was a temperature gradient between the two compartments in the case of a 0.0 cm distance because the temperature gradient between the catalyst and absorbent beds cannot change as a sharp step, i.e. there is a gap between the actual, ideal and simulated behaviour, shown in Figure 3.15. In our simulation, this temperature gradient was assumed to be located in the absorbent bed only, and based on the simulation results in Figures 3.7 and 3.8, part of the absorbent bed had a higher temperature than the set point (150 ˚C). The temperature gradient between the two compartments is a potential issue, which might affect the match between experimental and modelling results. Another reason for the mismatch between the experimental and simulation-based results may due to the fact that the commercial iron catalyst used in our experiments was not identical to the catalyst used in the literature. Both of these factors are thought to introduce deviations from our simulation results.

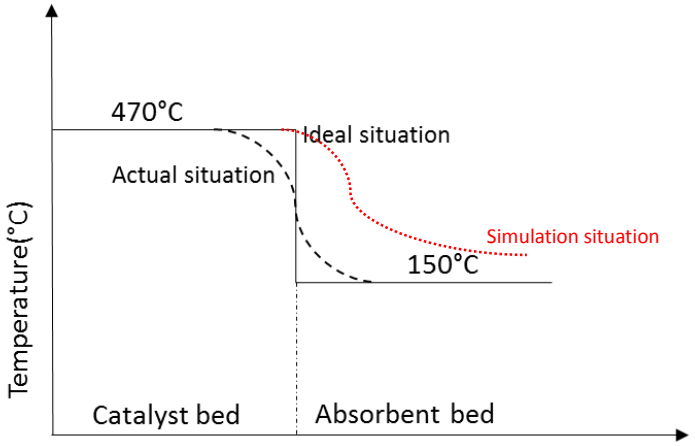

Figure 3.15. Comparison of the temperature variation under different situations.

3.6 Conclusions

In this chapter, experimental testing under Haber Bosch conditions and a preliminary model were developed for the adjacent coupling absorptive reactor. The bench-scale ammonia synthesis reactor coupled with magnesium chloride as the absorbent was operated at various bed-packing distances. The reaction conversion improved in the presence of $MgCl_2$ absorbent, especially when the distance between catalyst and absorbent is zero. Experimental results revealed that the conversion was affected by the distance between the catalyst and absorbent beds. The varying distances demonstrated that the closer the absorbent, the greater the improvement in the production rate. The initial model seems to be consistent with experimental results, indicating the possibility for further improving the combined bed reactor with the absorbent unit, a design that would result in a higher reaction conversion than one without absorption. The backflow between the catalyst and absorbent beds, assumed to explain the observation of an improved synthesis conversion in the presence of absorbent material, was approximated by a hypothetical recycle stream. The varying distance was represented by a hypothetical fraction of backflow in the model. Our experiments and simulation support the hypothesis that increasing the degree of backflow leads to higher conversions. The increase in the ammonia conversion was under the kinetic limitation, as the thermodynamic equilibrium was not yet reached. The backflow in the catalyst bed may create wider residence time distribution; meanwhile, a lower ammonia concentration caused by absorption could result in a faster reaction rate. Thus, a kinetically controlled regime, a faster reaction rate can result in a higher ammonia conversion, which is closer to the thermodynamic equilibrium.

Based on experimental data in the absorption-enhanced reactor, the per-pass conversions are 9.33%, 6.89%, and 4.59% at 0.0, 5.0, and 10.0 cm packing separation between the catalyst and absorbent beds, respectively. However, the simulation conversions for the absorptive reactor are 5.70% to 11.80% when the backflow fraction changes from 0 to 100%, which are higher than the corresponding experimental values. The simulation results indicate that the

reaction conversion similarly decreases when the backflow fraction decreases corresponding to the increased packing distance. Therefore, the numerical solution for the absorption-enhanced ammonia-synthesis reactor model can be qualitatively validated with the experimental results. There have been potential sources of error and shortcomings in this simulation. The laboratory apparatus used did not allow us to measure the absorption rates under Haber Bosch conditions (high pressure and high temperature), so it was difficult to collect absorption rates under the same conditions as for the simulation. As a result, the simulation of the fixed-bed absorbent used mass/heat transfer parameters from the literature under Haber Bosch conditions, as the data at mild conditions were not representative of the absorption rates under industrial conditions. Similarly, the commercial catalyst used was not identical to the literature catalyst, which is thought to have introduced differences in the simulation results.

The temperature of the catalyst and absorbent beds were attempted to be controlled independently and kept isothermal at different temperature values. However, there were difficulties in controlling the temperature of the absorbent bed. A temperature gradient existed between the two compartments, as a result this may have affected the match between experiment and model. The scarcity of the experimental data was also mentioned.

Although simulation of the backflow suggested that the effect could be very similar to gas recycling, at this stage our laboratory equipment is unable to accommodate gas recycling. Thus, there are the shortcomings from our reactor design the verification of the experiment from simulation data, but this would be a future experiment, which we would like to perform.

In this chapter, the hypothetical recycle stream model focuses on the effect of distance between catalyst and absorbent beds on the per-pass conversion, and gives possible reasons for the improvement of the per-pass reaction conversion. These reasons and the absorption effect will be further explored via the transient backflow cell model in Chapter 4.

Chapter 4. The transient backflow cell model of the adjacent coupling absorptive reactor

4.1 Introduction

Chapter 3 has demonstrated that the improvement in conversion was affected by the distance between the catalyst bed and absorbent bed, which was represented by different backflow fractions in the recycle stream model. Based on the results of Chapter 3, the best conversion of the absorptive reactor occurs when the absorbent bed is adjacent to the catalyst bed. Therefore, the only condition considered in this chapter is a 0 cm distance between the catalyst and absorbent beds. Based on the results of Chapter 3, there are two possible reasons for the improvement: the wider residence time distribution and the influence of absorption (absorb ammonia to increase the reaction rate and drive the reaction equilibrium to the right). The reason for the improvement in conversion needs to be further explained. Furthermore, the required amount of absorbent (the optimal length of the absorbent bed) also needs to be investigated.

One of the goals of this thesis is to synthesise ammonia under milder conditions. This chapter explored the use of milder conditions, i.e. a lower temperature (400 ˚C) for the catalyst bed and a lower pressure (10 bar), compared with Chapter 3. Furthermore, this would reduce the temperature difference between the catalyst and absorbent beds in the adjacent-coupling absorptive reactor. We aim to determine whether the enhancement of conversion still occurs when the operating temperature of the catalyst is decreased.

In this chapter, the reason was identified through a more detailed model. The transient backflow cell model (BCM) for the absorptive reactor was created to verify the absorption effect and determine the most efficient absorbent amount. The simulation starts from the very beginning of the process, therefore the performance of reactor is related to time. However, after a period of time after the operation, the system will be at steady state. Whether the length

of the absorbent bed is long enough to meet the requirement of complete ammonia separation within a certain time was investigated. Meanwhile, the transient cell model (CM) was also implemented as a reference to simulate the absorptive reactor when assuming no backflow and, therefore, no absorption effect occurring.

The cell model was first proposed by Deans and Lapidus [135][136]. In their cell models, the reactor was represented by ideally stirred tank reactors (cells) connected in series, i.e. each fixe-bed catalyst layer with its bulk fluid is considered as a cell, and each cell is connected with the adjacent cells. The simplest cell model is obtained by assuming that the network is a one-dimensional series of stirred tanks. The transient cell model is one of the cell models.

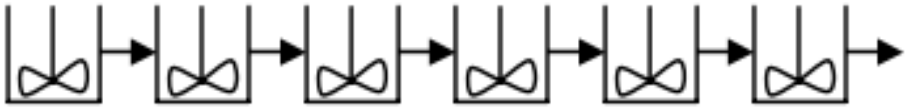

Figure 4.1. Schematic diagram of the simplest cell model [137].

On this basis mixing effects can be enhanced by introducing additional interactions between the cells [138]. Figure 4.2 corresponds to the one-dimensional model with axial dispersion [139], on which the transient backflow cell model is based.

Figure 4.2. Schematic diagram of the cell model with axial dispersion [137].

Actually, the backflow cell model has actually been adopted in many other types of research before. For example, the backflow-cell model was applied to a two-phase flow process with the exchange of a single solute [140]. The backflow cell models of isothermal flow reactors were developed for a reversible reaction in finite reactors to consider the effect of backflow upon the maximum product yields [141]. This model has also been derived for flow systems with longitudinal mixing to determine the cell responses to an impulse input of tracer in the inlet

stream [142]. The analyses for the backflow cell model of a distillation plate with linear interphase mass transfer [143], of an ozone bubble column [144], of a static mixer [145], and of tubular adiabatic reactors [146] were also given. Extraction and absorption column dynamics were also simulated through backflow cell model [147][148]. The backflow cell model is convenient because the mathematical treatment is simple, as shown by a numerical investigation for multiple stages.

The structure of this chapter is as follows. In Section 4.2, experimental results were obtained from a lab-scale absorptive reactor, which demonstrated the enhanced conversion of ammonia synthesis. The mathematical model of this packed-bed absorptive reactor was developed and implemented in MATLAB® in Section 4.3. These models consisted of a set of differential equations that were solved simultaneously, with the simulation results shown in Section 4.4. The sensitivity on the number of cells, as one parameter used in the model, was also considered in this section. Finally, the conclusions of the work are summarised in Section 4.5

4.2 Experimental section

4.2.1 Catalyst preparation

The synthesis of Cs-Ru/MgO followed the incipient wetness impregnation procedure. Commercial MgO powder was evacuated overnight at 70 °C inside a vacuum oven. $Ru_3(CO)_{12}$ was then sonicated and dispersed in Tetrahydrofuran and loaded onto the MgO powder by the incipient wetness impregnation method. The mixture was left to stir for 4 h, and the solvent was removed through rotary evaporation. The Ru-loaded catalyst was then calcined under flowing Argon at 350 °C for 6 h. The addition of the promoter Cs again followed the impregnation method. $CsNO_3$ was dissolved in distilled water and then impregnated to the calcined Ru/MgO powder. Prior to the catalytic testing, the Cs-Ru/MgO powder underwent reduction at 350 °C for 4 h under 5% H_2 in Argon.

4.2.2 Ammonia synthesis activity tests

The effect of the absorbent on ammonia production was tested in a fixed bed continuous flow reactor (Figure 3.1 in Chapter 3) using Cs-Ru/MgO catalyst. 0.1 g Cs-Ru/MgO catalyst and 1 g absorbent ($MgCl_2$) with quartz wool in between were packed. Prior studies have determined that the use of absorbents maximally promotes the catalytic reaction when the distance between absorbent and catalyst beds is zero. Therefore, the absorbent bed in this study was located directly next to the catalyst bed. The thickness of quartz wool is 0.1 cm, which can be neglected in the simulation. A 3:1 mixture of H_2 and N_2 was passed through the reactor at a pressure of 10 bar and a weight hourly space velocity of 36,000 $mLg^{-1}h^{-1}$. During the reaction step, the catalyst was at 400 ˚C and the absorbent at 150 ˚C. Finally, any ammonia absorbed on the absorbent was desorbed by heating the absorbent to 400 ˚C at ambient pressure. The other experimental settings were in accord with the experimental setup section in Chapter 3.

4.2.3 Experimental results

Catalyst activity results were calculated from the ammonia collected after 1 h of reaction and 2 h of desorption. The use of the absorbent increased the per-pass reaction conversion by a factor of 1.55, to 7,884 $\mu molg^{-1}h^{-1}$ compared with 5,082 $\mu molg^{-1}h^{-1}$ without absorbent. The results revealed that the ammonia conversion in the catalyst-absorbent coupled reactor was higher than that in the catalyst reactor without absorbent even under milder conditions.

4.3 Mathematical model

The backflow process leads to two possible mechanisms that affect the per-pass conversion of the reaction: wider residence time distribution and ammonia removal due to the absorption effect. In this section, we identify each mechanism via two models: the transient BCM and the transient CM for the adjacent-coupling absorptive reactor and the conventional reactor (catalyst bed only). The simulation was based on the same operating conditions as the

experimental setting.

4.3.1 The transient backflow cell model

4.3.1.1 The absorptive reactor

Figure 4.3 represents a schematic of the transient BCM in an absorptive ammonia synthesis reactor. The BCM hypothesises a stable unchanging backflow, expressed by $\dot{q}\beta$ between each cell, to characterise the backflow in the reactor. There are *m* cells in the catalyst bed and *n* cells in the absorbent bed. In this case, the backflow ratio β represents the backflow amount. An β of zero is the plug flow limit; while when β equals infinity, the model approaches the stirred tank limit. The assumptions that govern the development of transient BCM are:

- Due to symmetry in the radial direction of the packed bed, the governing equations were independent of this direction. Thus, a one-dimensional model was considered.
- Constant actual (interstitial) velocity and volumetric flow of gas were assumed, as the per-pass conversion of the reaction is quite low at about 1-2 %. Therefore, the volume change during the reaction and absorption processes was low enough to be ignored and the velocity can be assumed to be constant.
- Isothermal condition for the catalyst bed was assumed, based on the discussion in Chapter 3.
- Each cell was assumed to be perfectly mixed.
- Instantaneous equilibrium of the solute in the bulk fluid with the absorbate.
- Catalyst/absorbent packing has uniform voidage and particle size.

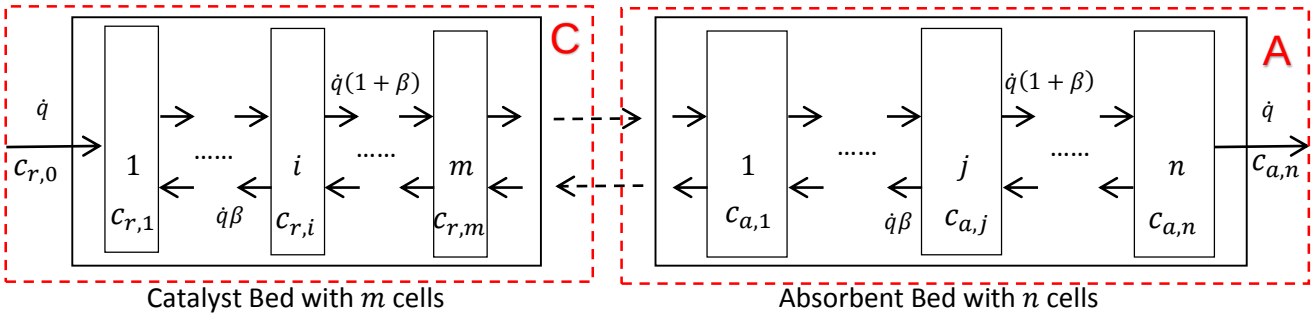

Figure 4.3. Schematic diagram of the BCM in the ammonia synthesis absorptive reactor.

According to these assumptions, the differential equations of the transient BCM were developed along the axial direction based on the principle of mass balance. The mathematical relationship for these cells can be written as follows. For the first cell of the catalyst bed:

$$V_{r,f} \cdot \frac{dc_{r,1}}{dt} = \dot{q}c_{r,0} + \dot{q}\beta c_{r,2} - \dot{q}(1+\beta)c_{r,1} + V_{r,c} \cdot R_r \tag{4.1}$$

Similarly, the modelling equations for the intermediate cells of the catalyst bed (*i* = 2, 3, …, m-1) can also be written.

$$V_{r,f} \cdot \frac{dc_{r,i}}{dt} = \dot{q}(1+\beta)c_{r,i-1} + \dot{q}\beta c_{r,i+1} - \dot{q}(1+2\beta)c_{r,i} + V_{r,c} \cdot R_r \tag{4.2}$$

For the last cell of the catalyst bed:

$$V_{r,f} \cdot \frac{dc_{r,m}}{dt} = \dot{q}(1+\beta)c_{r,m-1} + \dot{q}\beta c_{r,m+1} - \dot{q}(1+2\beta)c_{r,m} + V_{r,c} \cdot R_r \tag{4.3}$$

For the first cell of the absorbent bed:

$$V_{a,f} \cdot \frac{dc_{a,1}}{dt} = \dot{q}(1+\beta)c_{a,0} + \dot{q}\beta c_{a,2} - \dot{q}(1+2\beta)c_{a,1} + V_{a,c} \cdot R_a \tag{4.4}$$

For the intermediate cells of the absorbent bed, *j* = 2, 3, …, n-1:

$$V_{a,f} \cdot \frac{dc_{a,j}}{dt} = \dot{q}(1+\beta)c_{a,j-1} + \dot{q}\beta c_{a,j+1} - \dot{q}(1+2\beta)c_{a,j} + V_{a,c} \cdot R_a \tag{4.5}$$

For the last cell of the absorbent bed:

$$V_{a,f} \cdot \frac{dc_{a,n}}{dt} = \dot{q}(1+\beta)c_{a,n-1} - \dot{q}(1+\beta)c_{a,n} + V_{a,c} \cdot R_a \tag{4.6}$$

with initial conditions:

$$At\ t = 0; c_{N_2} = 10^{-5};\ c_{H_2} = 3 \times 10^{-5};\ \ c_{NH_3} = 0\ ; \tag{4.7}$$

where $\dot{q}$ is the inlet gas flowrate (in m^3/s) and $\dot{q}\beta$ is the backflow. The forward flow increases to $\dot{q}(1+\beta)$. The mass balances for hydrogen, nitrogen, and ammonia are respectively calculated by Equations (4.1) through (4.6), with different reaction rates and absorption rates.

The intrinsic rate of reaction R_{r,NH_3} is calculated by the Temkin expression in mol/(m^3·s) [116], and given in Equation (3.3) of Chapter 3. According to the reaction stoichiometric coefficients,

the reaction rates of nitrogen and hydrogen are:

$$R_{r,H_2} = -1.5 \times R_{r,NH_3} \tag{4.8}$$

$$R_{r,N_2} = -0.5 \times R_{r,NH_3}$$

The absorbents only absorb ammonia. Therefore, the absorption rate for hydrogen and nitrogen is zero.

$$R_{a,H_2} = R_{a,N_2} = 0 \tag{4.9}$$

Based on the breakthrough curves of the absorbent [14], the ammonia concentration of the outlet flow is kept at zero until the absorbent bed begins to saturate. In this mathematical model, the absorbent bed is first assumed to be at a non-saturated condition. The saturation condition of the absorbent will then be considered to determine the influence of the absorbent amount.

While a detailed mechanism for absorption is not known, kinetic experiments conducted previously [149] allow the fitting of an analytical equation:

$$R_{a,NH_3} = k_{a1} e^{k_{a2}(P_{NH3} - P^*_{NH3})} \; when \; (P_{NH3} - P^*_{NH3}) < 1 \; bar \tag{4.10a}$$

$$R_{a,NH_3} = k_{a3}(P_{NH3} - P^*_{NH3})^2 \; when \; (P_{NH3} - P^*_{NH3}) > 1 \; bar$$

where R_{a,NH_3} is the rate in moles per second per unit volume of absorbent, k_{a1-a3} are experimentally determined constants, P_{NH3} is the pressure of ammonia in kPa, and P^*_{NH3} is the equilibrium pressure of ammonia at a given temperature in kPa, as illustrated in [6]. Based on simulation results in Chapter 3, the temperature for absorption is not exactly 150 °C, but about 20 °C higher than the setting. Therefore, these analytical equations will be calculated based on the temperature profile in the absorbent bed at about 170 °C. The experimental results, which form the basis for these equations are presented in [6].

$$k_{a1} = 1.6 \times 10^{-4} \; \frac{\mu mol}{s \; g_{abs}}$$

$$k_{a2} = 9.0 \times 10^{-2} \; kPa^{-1} \tag{4.11b}$$

$$k_{a3} = 3.8 \times 10^{-6} \; \frac{\mu mol}{s \; g_{abs} \; kPa^2}$$

4.3.1.2 The conventional reactor

The schematic of the transient BCM of the conventional reactor is shown in Figure 4.4. The existence of backflow in the conventional reactor results in the flow passing through the catalyst bed with a wider residence time distribution. Therefore, more cells were assumed in the model as shown in Figure 3.14: the cell number in the BCM of the catalyst bed is *m'*, which was higher than *m* in CM.

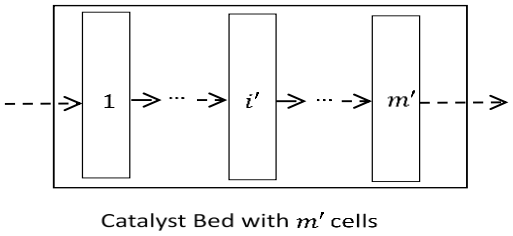

Figure 4.4. Schematic diagram of the BCM in the ammonia catalyst bed.

Similarly, the modelling equation for the cells of the catalyst bed (i' = 1, 2, …, m') can be written as Equation (4.11).

$$V_{r,f} \cdot \frac{dc_{r,i'}}{dt} = \dot{q}c_{r,i'-1} - \dot{q}c_{r,i'} + V_{r,c} \cdot R_r \quad (4.12)$$

4.3.2 The transient cell model

4.3.2.1 The absorptive reactor

The schematic diagram of the absorptive reactor is illustrated in Figure 4.5. The reactants flow in one direction.

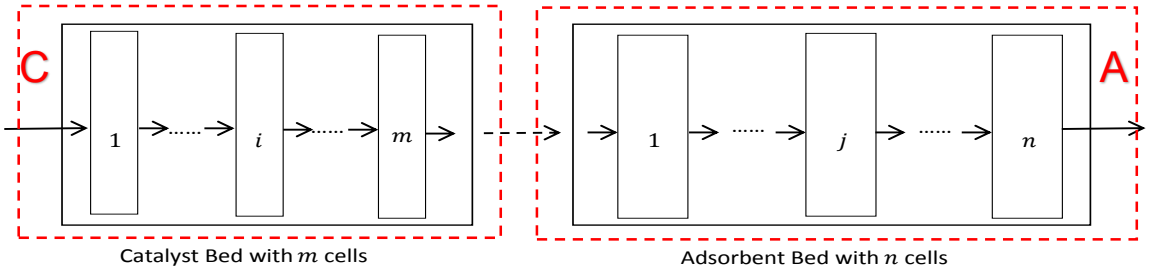

Figure 4.5. Schematic diagram of the CM of the absorptive ammonia reactor.

The modelling equation for the cells of the catalyst bed is consistent with Equation (4.11) for (i = 1, 2, …, m), while those for the cells of the absorbent bed can be written as Equation (4.12):

$$V_{a,f} \cdot \frac{dc_{a,j}}{dt} = \dot{q}c_{a,j-1} - \dot{q}c_{a,j} + V_{a,c} \cdot R_a \tag{4.13}$$

4.3.2.2 The conventional reactor

For the transient CM of the conventional reactor, the schematic was the same as the left part 'C' in Figure 4.5. The material balance equations without backflow agreed with Equation (4.11) in terms of a cell element along the axial direction inside the catalyst bed.

4.4 Numerical results and discussion

The governing equations of the transient BCM and transient CM are ordinary differential equations, which were solved using the ode15s solver from MATLAB®. The numerical results and discussion are presented in this section. Parameters used in these models are listed in Appendix B. Nitrogen is taken as the reference to calculate the reaction conversion. The number of cells used and cell size has been listed in Table 4.1. These settings are the same for both BCM and CM simulations.

Table 4.1. Number and length of cells in the conventional and absorptive reactors.

	Conventional reactor	Absorptive reactor
Catalyst bed (1)	8	8
Absorbent bed (1)	-	10
Catalyst cell length (m)	0.001	0.004
Absorbent cell length (m)	-	0.01

4.4.1 The conventional reactor

The transient CM of the conventional reactor consists of 3×m governing equations (presented in Section 4.3.2.2), with 3×m unknowns (the concentrations of H_2, N_2, NH_3 in m cells). Figure 4.6(a) depicts the concentration of these three components in the catalyst bed at different times. The steady-state concentration of hydrogen and nitrogen for the downstream position is lower than upstream positions as the reaction progresses ($c_{N_2/H_2,7} < \cdots < c_{N_2/H_2,5} < \cdots < c_{N_2/H_2,1}$). For the first cell of the catalyst bed (m = 1), the nitrogen and hydrogen decrease until equilibrium is reached. However, the concentration profiles for cells after the first one increase from zero and reach equilibrium as time is needed for the reactants to reach the following cells from the inlet. As illustrated in Figure 4.6(b), the concentration of ammonia increases from the first cell to the end as a result of the superposition of the produced ammonia. The conversion in the catalyst bed is 6.25%, according to the simulation results, which depend on the parameters used in the model, such as length of the catalyst bed, temperature, and pressure.

As illustrated in Figures 4.6(c), the concentration profiles of ammonia change with the location at different times. The concentration of ammonia increases with time in each one of the cells and eventually reaches a steady value. From Figure 4.6(c), we can also see that the concentration of ammonia has progressively increased from the first cell to the end. The concentration of nitrogen through the catalyst fixed bed varies from left to right as the fluid flows through the catalyst bed and reaches a steady value after some time.

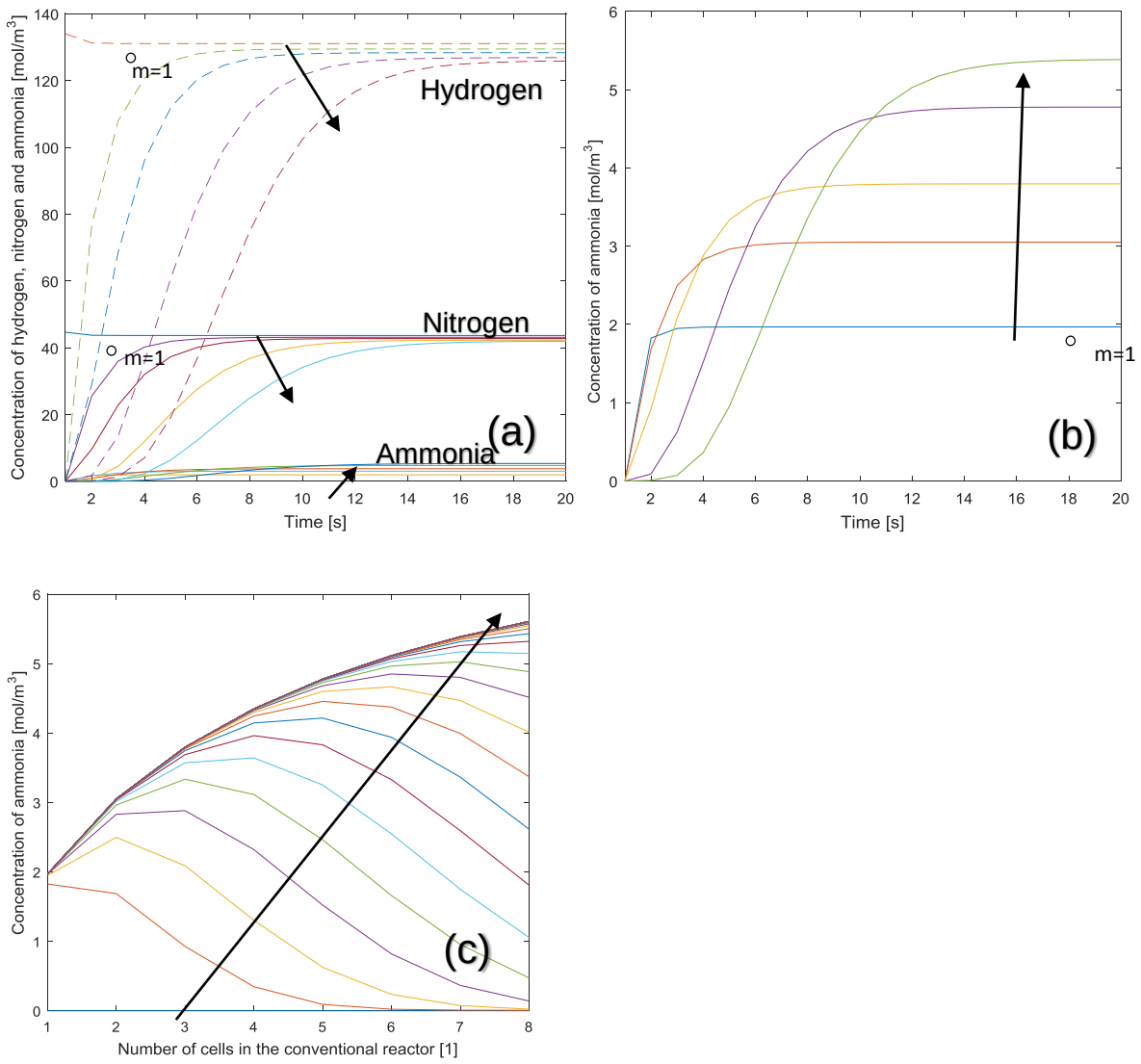

Figure 4.6. The concentration of (a) hydrogen, nitrogen, and ammonia and (b) ammonia in the conventional reactor changes with time (arrows point in the direction of an increasing number of cells). (c) The concentration of ammonia in the conventional reactor changes with location (arrow points in the direction of increasing time), calculated with the catalyst at 673 K. A 3:1 mixture of H_2: N_2 at 10 bar and a weight hourly space velocity of 36,000 mL $g^{-1}h^{-1}$ were used.

The reaction equilibrium has not been reached in Figure 4.6 (6.25%), as the thermodynamic equilibrium conversion of ammonia synthesis from H_2: N_2 = 3:1 at T = 400 °C and P = 10 bar is 7.45%, shown in Figure 4.7. Therefore, the effect of the catalyst bed length on the reaction conversion was first considered here. As demonstrated in Figure 4.7, the conversion of the ammonia synthesis rises sharply at first with the increasing length of the catalyst bed, then

reaches a stable value: the equilibrium value of the reversible reaction. This balance cannot be broken unless the reaction conditions change or the product is removed. In Figure 4.7, the ammonia synthesis reaches equilibrium when the catalyst bed is longer than 0.04 m.

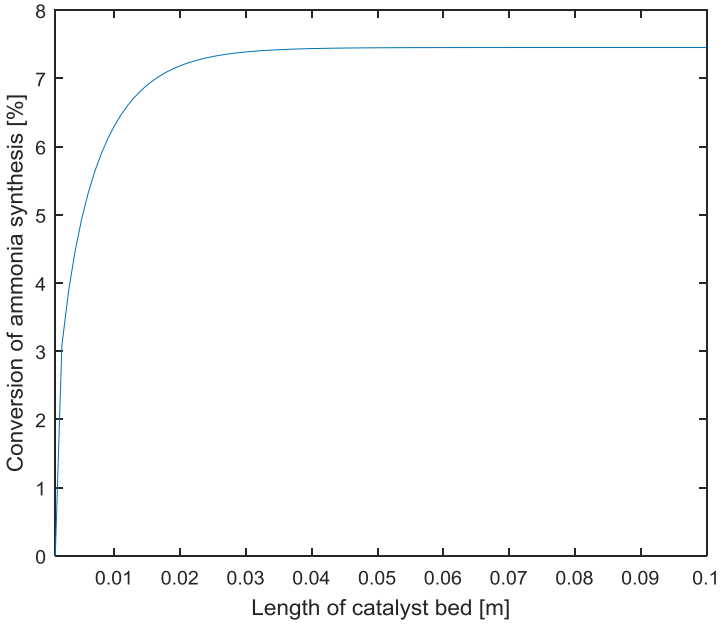

Figure 4.7. The conversion of ammonia synthesis varies with the length of the catalyst bed.

Based on the transient BCM of the conventional reactor, the relationship between the per-pass reaction conversion and the backflow ratio is identified. As depicted in Figure 4.8, the ammonia synthesis conversion will not change with the backflow fraction when the conversion has already reached equilibrium (when the length of the catalyst bed is 0.1, 0.2, 0.5, or 1 m).

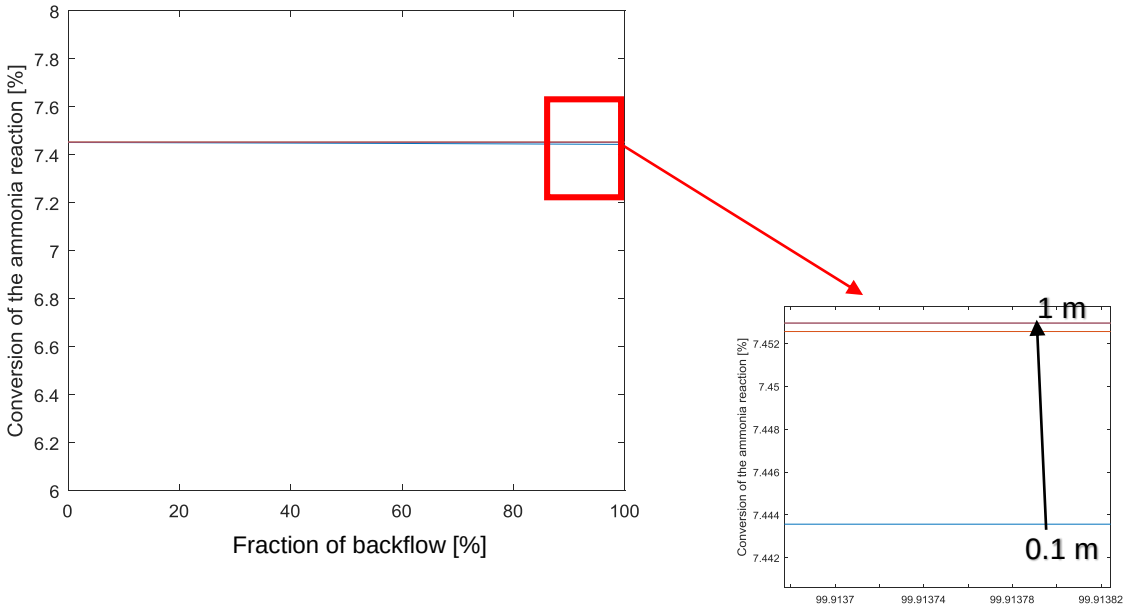

Figure 4.8. Effect of the backflow fraction on the ammonia synthesis conversion when the length of the catalyst bed is 0.1, 0.2, 0.5, and 1 m, respectively.

However, for a catalyst bed length below the equilibrium length (0.04 m), the reaction conversion is affected by the backflow fraction. Figure 4.9 presents the conversion of ammonia synthesis under various backflow fractions. The backflow brings about wider residence time distribution, and was represented by a larger cell number in this simulation, same as explanation in Figure 3.14. An increase in ammonia production conversion from 6.25% to 7.25% can be observed. In the transient BCM of the conventional reactor, the fraction of backflow was assumed to be related to the number of cells in the catalyst bed. When the backflow fraction is 100% (100% fluid start at the beginning and flow right through to the end of the catalyst bed all over again), the catalyst bed is assumed to be extended by the same amount of its cell number, equivalent to that the reactant mixture has a wider residence time distribution for reaction.

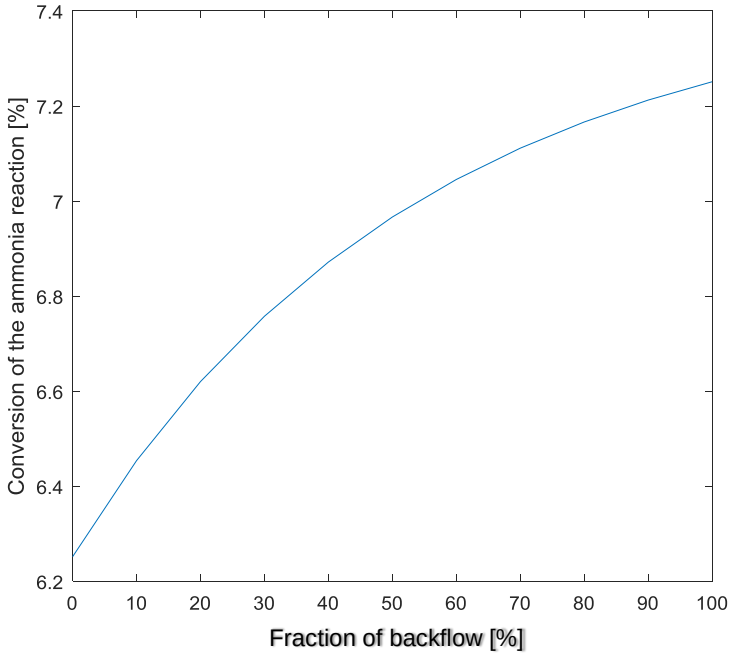

Figure 4.9. The effect of backflow fraction on the ammonia synthesis conversion when the length of the catalyst bed is 0.01 m.

Based on the results in Figure 4.6, it can be concluded that the number of cells is an important parameter in the BCM and CM. Therefore, it is necessary to analyse the sensitivity on the number of cells in a fixed-length catalyst bed, which is displayed in Figure 4.10. The cell number is one parameter of the BCM simulation. The sensitivity study of cell number is a significant aspect as an excess of cell number will lead to a heavy and complicated calculation while an insufficient cell number will affect the simulation result. When the number is bigger than 8, the effect of cell number can be eliminated. Therefore, in this case, the insufficient cell number means that the cell number is less than 8. In Figure 4.10. When the length of the catalyst bed is longer than the equilibrium length (0.04 m), the cell number should be larger than 8, then the results stop changing with cell number. However, when the length of the catalyst bed is shorter than 0.04 m, increasing the number of cells will slightly increase the reaction conversion. In this case, a cell number of 12 is taken to minimise the deviation due to the dependence on cell number. The backflow fraction was assumed to be at a certain value, 10% in this case to evaluate the cell number effect.

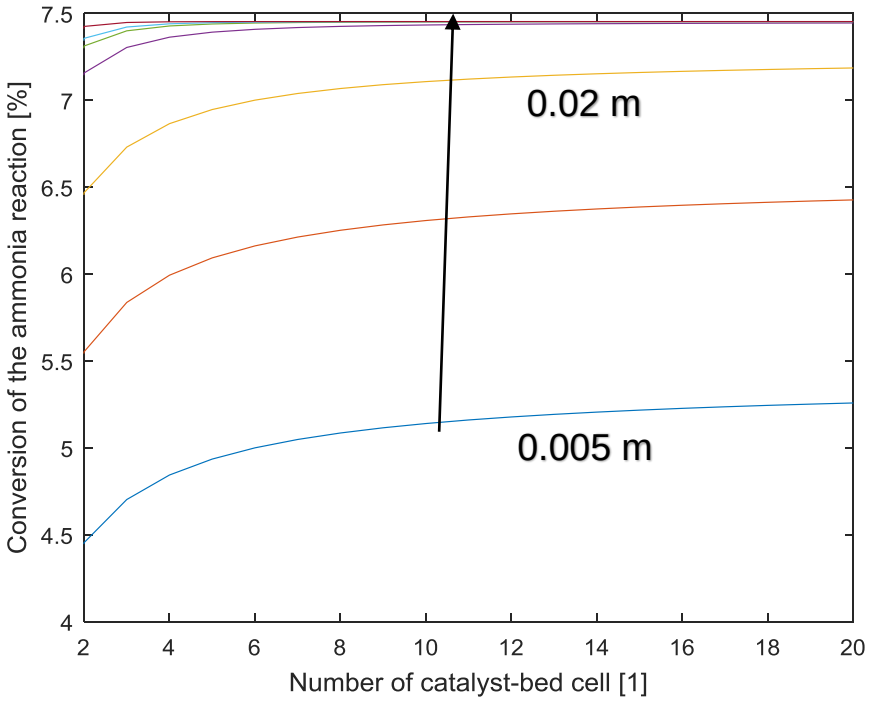

Figure 4.10. The sensitivity on the number of cells in the catalyst bed. (The length of catalyst bed equals 0.005, 0.01, 0.02, 0.05, 0.08, 0.1, and 0.2, respectively).

4.4.2 The absorptive reactor

Based on the results in Section 4.4.1 for the simulation of the absorptive reactor, the length of the catalyst bed was fixed to 0.04 m to ensure that the reaction equilibrium was reached, and therefore the effect only of absorption capacity in the absorptive reactor could be focused on. The cell number was set to be 8 to decrease computation time. The transient CM of the absorptive reactor consists of 3×$(n+m)$ governing equations (Section 4.3.2.1), with 3×$(n+m)$ unknowns (the concentrations of H_2, N_2, NH_3 in $n+m$ cells). Figure 4.11(a) presents the concentration of nitrogen and hydrogen along the catalyst and absorbent beds. The concentrations of these components in the catalyst bed are the same as in Figure 4.6(a). Figure 4.11(b) is the changes of ammonia concentration in the absorptive reactor. To construct a better illustration, the ammonia product is separately displayed in Figure 4.11(c). As depicted in Figure 4.11(c), the concentration sharply reduces to zero after the catalyst bed caused by the absorption of ammonia. The per-pass conversion of the absorptive reactor is 7.45%, calculated by the transient CM, which is the same as the conversion of the conventional reactor.

Therefore, the absorption does not affect the ammonia synthesis conversion when using the transient CM, which is not consistent with the experimental results.

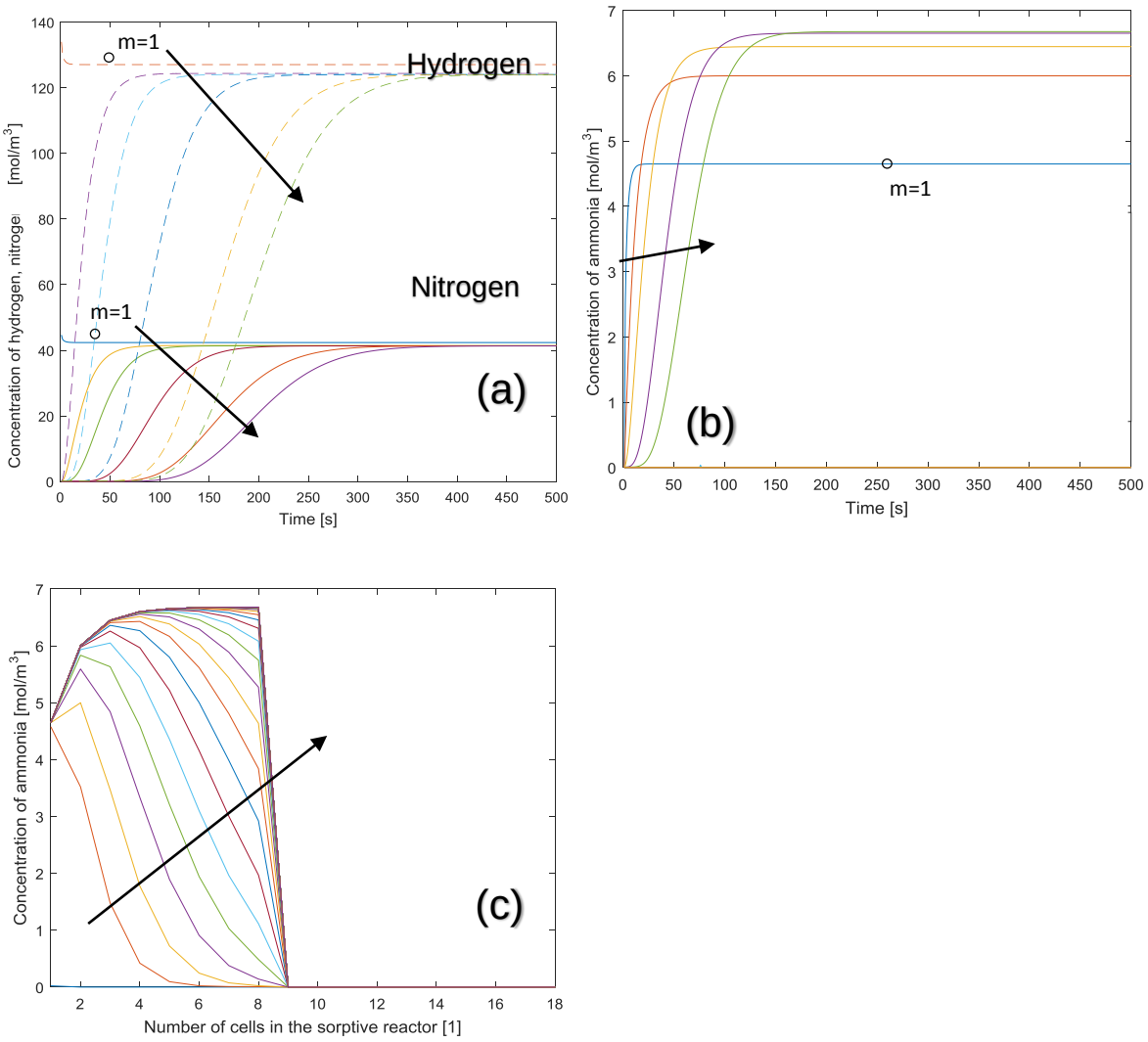

Figure 4.11. The concentration of (a) hydrogen and nitrogen and (b) ammonia in the absorptive reactor changes with time (arrows point in the direction of an increasing number of cells). The concentration of (c) ammonia in the absorptive reactor changes with location (arrow points in the direction of increasing time), calculated with the catalyst at 673 K and absorbent at 423 K. A 3:1 mixture of H_2: N_2 at 10 bar and a weight hourly space velocity of 36,000 mL $g^{-1}h^{-1}$ were used.

Based on the experimental results, an absorption bed following the catalyst bed has an impact on the per-pass reaction conversion. Therefore, the transient CM does not apply to the

absorptive reactor and the simulation can be switched to the transient BCM taking the case of 50% backflow ratio. Figure 4.12 displays the results: the concentration profiles of ammonia and nitrogen. Unlike the transient CM results in Figure 4.11, the ammonia concentration decreases at the end of the catalyst bed, when the flow has yet to reach to absorbent bed. Furthermore, the nitrogen concentration has a second drop at the junction of the catalyst bed and absorbent bed, shown in the red square of Figure 4.12(b). This 'drag' is crucial to the effect on the ammonia synthesis per-pass conversion.

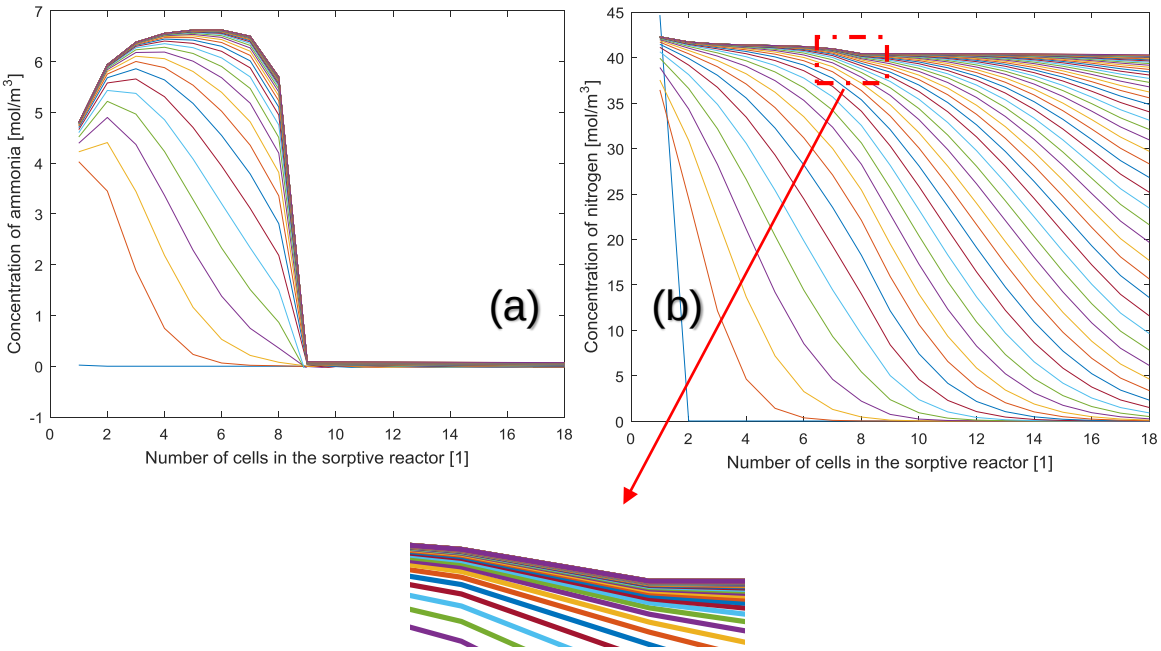

Figure 4.12. The concentration of (a) ammonia and (b) nitrogen with backflow ratio at 0.5 varying with the number of cells in the bed.

The comparison of the transient BCM and CM simulations is illustrated in Figures 4.13 to 4.15. In Figures 4.13 to 4.15, the dashed lines are concentration profiles from the CM simulation, while the solid lines are the simulation results of the transient BCM. Figure 4.13 depicts the concentrations of nitrogen and ammonia changing with time in different cells. The arrows point in the direction of increasing cell number. Figure 4.14 indicates the concentrations in the longitudinal direction of the reactor among the cells of catalyst and absorbent bed at various times. The arrows point in the direction of increasing time. Figure 4.15 gives a more intuitive presentation of three points in time from Figure 4.14.

As illustrated in Figures 4.13 to 4.15, the dashed curves and solid curves are noticeably different, which means that simulated results were influenced greatly by the backflow setting. Under the same cell number and same time conditions, a lower nitrogen concentration with lower ammonia concentration (due to absorption) is revealed for the catalyst bed part in the absorptive reactor with the BCM simulation in comparison with that in the CM simulation. This implies that the per-pass synthesis conversion in the BCM simulation is higher than the one predicted by the CM simulation. Indeed, the transient BCM matched experimental results better than the transient CM.

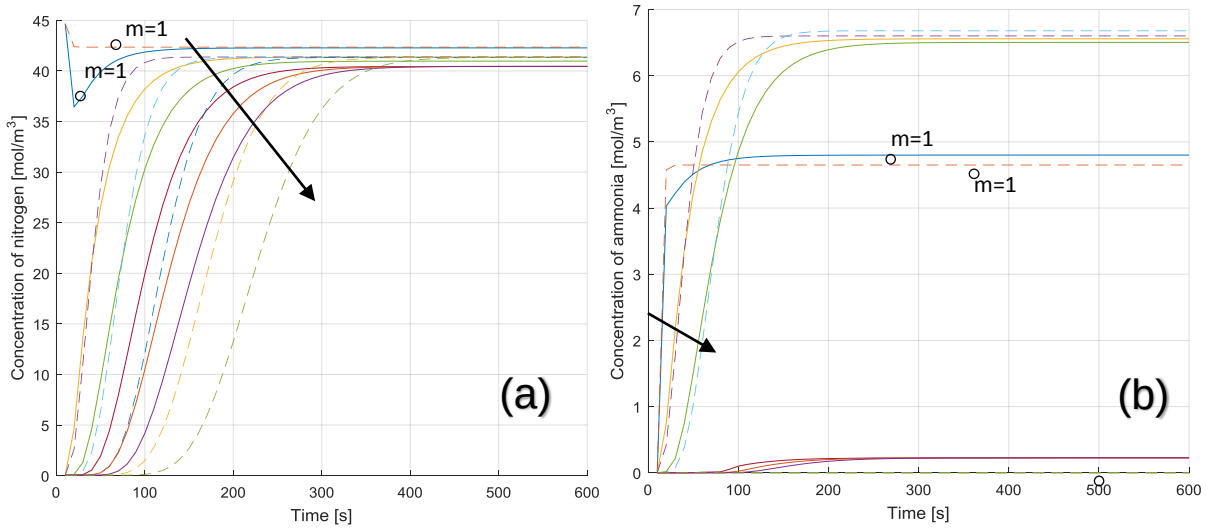

Figure 4.13. The concentration of (a) nitrogen and (b) ammonia in the absorptive reactor changes with time.

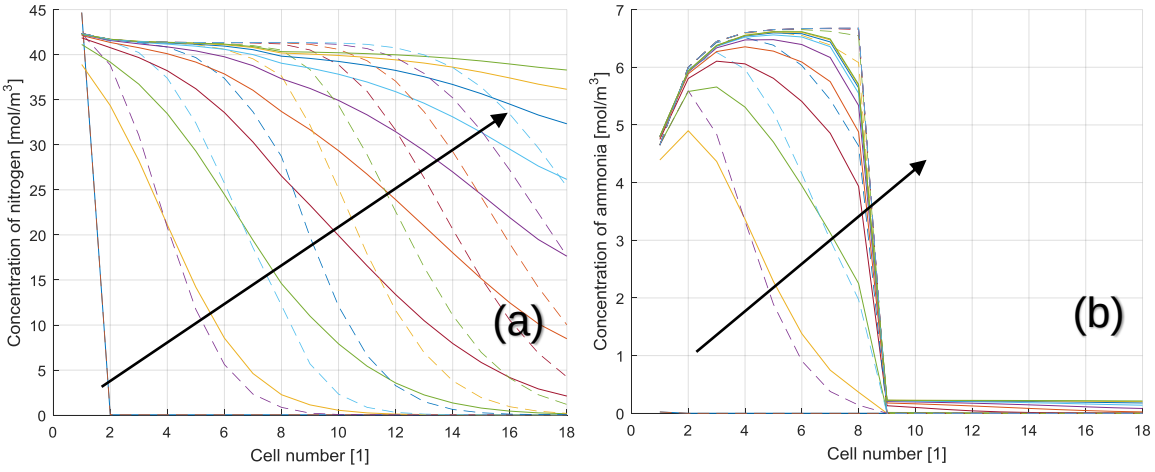

Figure 4.14. The concentration of (a) nitrogen and (b) ammonia in the absorptive reactor changes with position.

Based on the BCM simulation, the absorption capacity of the absorptive reactor, which promotes the reaction conversion, can be further analysed. In this BCM simulation, the equilibrium of the reaction in the catalyst bed has been reached as its length is set at 0.04 m with 8 cells. Therefore, the per-pass conversion of ammonia synthesis does not change when there is the only backflow without absorption, based on the results of Section 4.4.1. Therefore, the reason for improved conversion is because of the absorption capacity of the absorptive reactor, which speeds up the reaction rate and drives the reaction to the right as the partial pressure of ammonia decreases. Then, the backflow ratio, length and cell number of absorbent bed, as well as the saturation degree of absorbent bed, will be discussed.

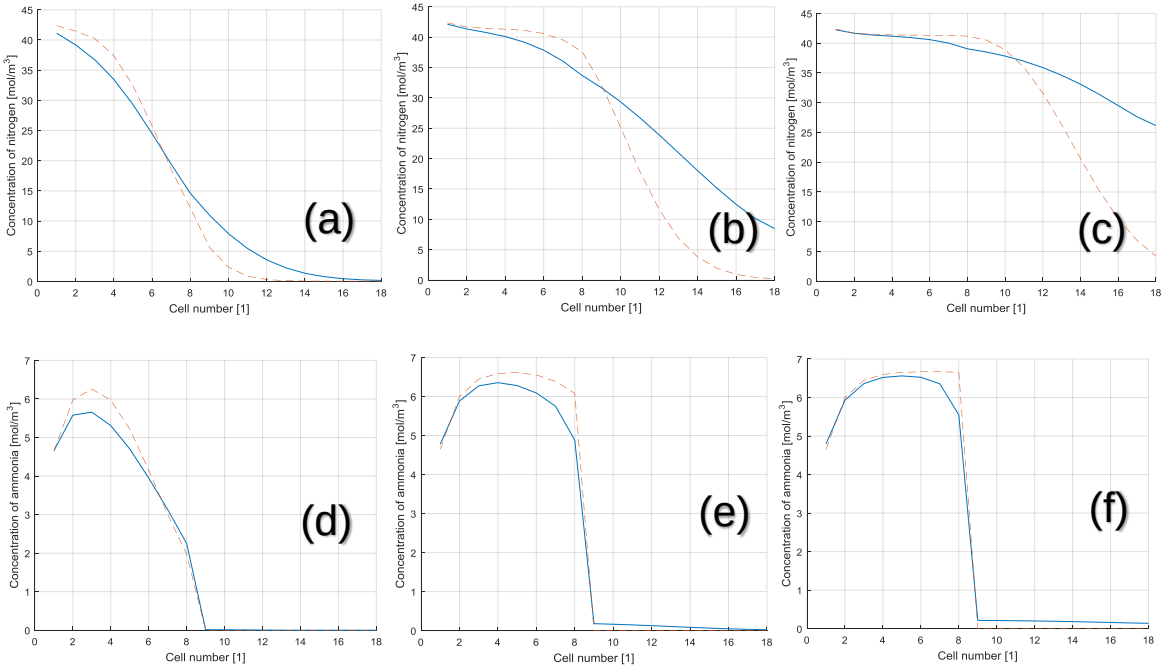

Figure 4.15. The concentration in the absorptive reactor changes with position. (a)(b)(c) t = 70, 130, 190 seconds, respectively, of nitrogen; (d)(e)(f) t = 70, 130, 190 seconds, respectively, of ammonia.

The concentrations of nitrogen under different backflow ratios are illustrated in Figure 4.16. The simulation results in Figures 4.16 and 4.17 are taken at the end of the simulation, 10 minutes. There is a downward trend of the nitrogen concentration through the absorptive

reactor when the backflow ratio changes from zero to one hundred. This trend is more pronounced for a higher backflow ratio, as shown in Figures 4.16 (c). The nitrogen concentration leaving the absorptive reactor is decreasing as the backflow ratio increases. This shows that the reaction conversion increases as backflow ration increases.

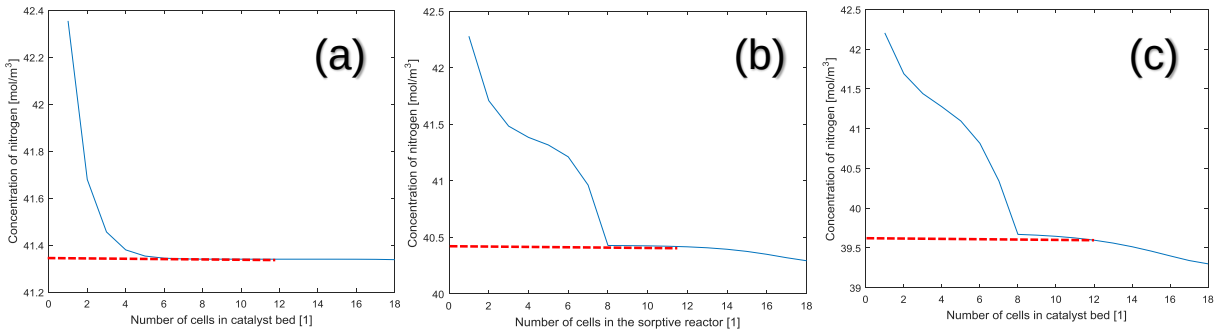

Figure 4.16. The concentration of nitrogen with backflow ratio at (a) 0%, (b) 50%, and (c) 100% varying with the number of cells in the absorptive reactor (at the end of simulation t=10 mins).

Figure 4.17 reveals a relationship between the synthesis conversion of the absorptive reactor and the backflow ratio. The reaction conversion has a linear growth as the backflow ratio increases when the absorbent bed has not been saturated. The practical implication would be that introducing or improving the backflow in an absorptive reactor could be good for per-pass synthesis conversion, which also applies to other researches. For example, various backflow zones can be observed in a long distance water supply pipeline, which increases the resistance of the water flow [150]. The obstacle inside solar air heater channel can create backflow [151]. The obstacle could increase the backflow ratio in a real reactor. In this case, the reaction conversion increases from 7.45% (the equilibrium conversion) to 11.2% in Figure 4.17. Therefore, the absorption in the absorptive reactor can drive the synthesis equilibrium to the right when the thermodynamic equilibrium of the reaction has already been reached.

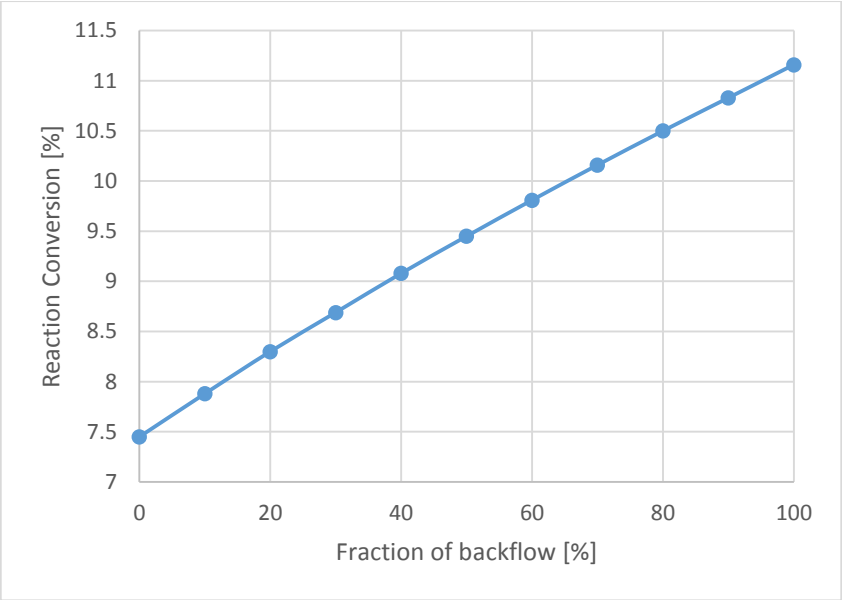

Figure 4.17. The relationship between reaction conversion and backflow fraction in the absorptive reactor (at the end of simulation t=10 mins).

Then, the length and cell number of the absorbent bed were considered for their impact in the conversion improvement. Figures 4.18 and 4.19 illustrate that increasing infinitely the length or the cell number of the absorbent bed does not affect the synthesis conversion when the absorbent bed was assumed to be unsaturated. As the synthesis process goes on, the absorbent bed will be saturated gradually, and once it is saturated completely, the absorptive reactor will lose its function. Therefore, in this step, we assume that the absorbent bed will always under an unsaturated condition to simply the calculation.

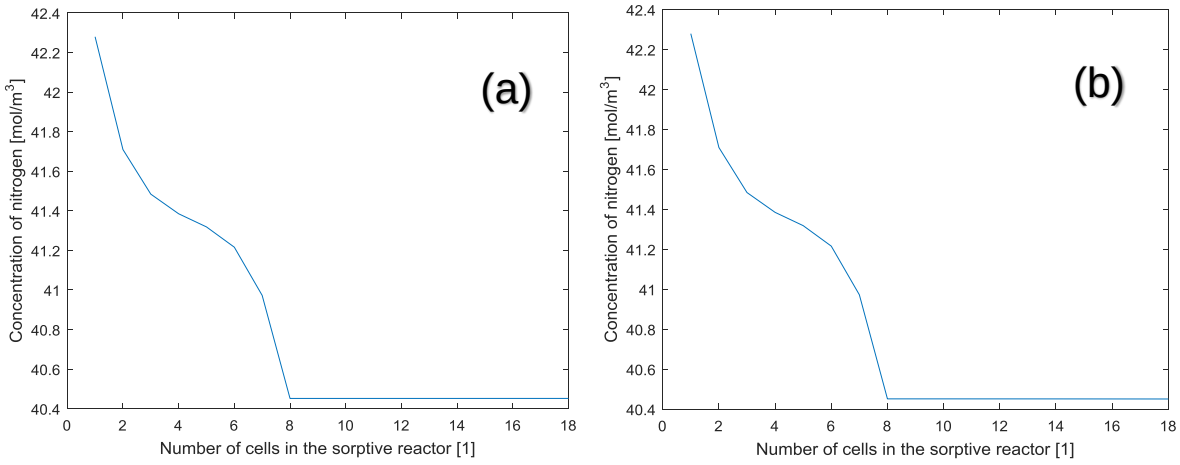

Figure 4.18. Concentrations of nitrogen under different absorbent bed lengths: (a) 0.05m, (b) 0.1m. The cell number of absorbent beds is 10.

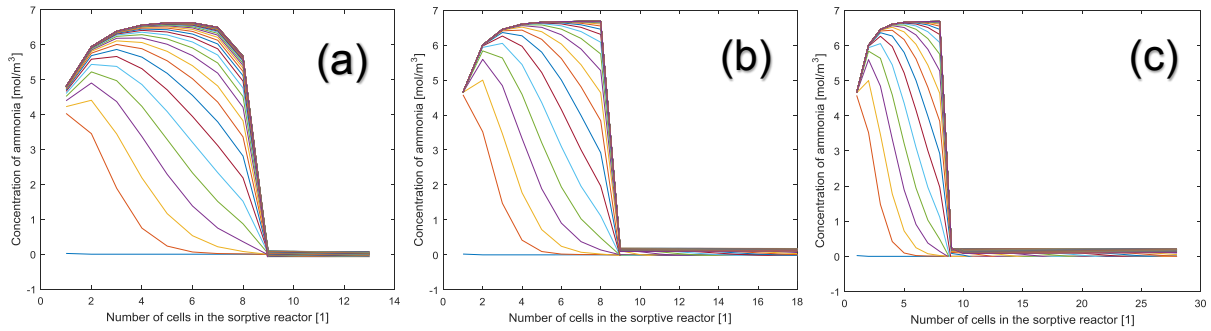

Figure 4.19. The concentration of ammonia in the absorptive reactor with varying absorbent cell numbers (a) 5, (b) 10, and (c) 20. The length of the absorbent bed is 0.1 m.

However, in reality, the absorbent bed is gradually saturated as the synthesis take place and the effect of absorption on the synthesis conversion begins to wane as the absorbent pellets stop absorbing ammonia. For example, Figure 4.20 displays a relationship between the absorptive reactor conversion and the saturated cells in the absorbent bed. In this case, the backflow ratio is set at 50% with a fixed-absorbent-bed length of 0.1 m. A saturated cell number equals to six, which means that the first six cells of the absorbent bed have been saturated and the absorption occurs at the seventh cell. Figure 4.20 reveals that the saturation state of only the first six cells in the absorbent bed can affect the synthesis conversion. Once the first six cells (0.06 m) are saturated, the conversion no longer increases, and there is no difference between an absorptive reactor and a conventional reactor.

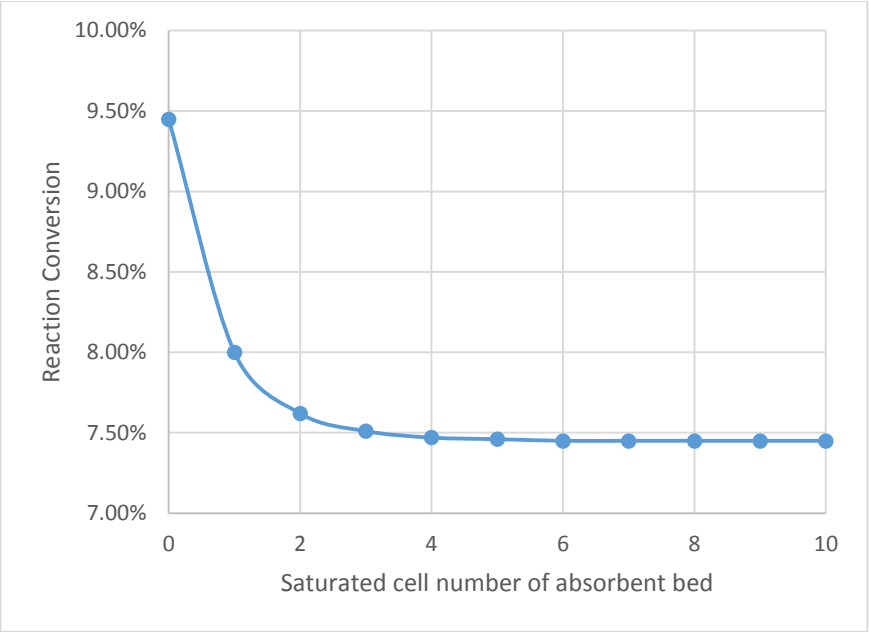

Figure 4.20. The reaction conversion of ammonia synthesis under a backflow ratio of 50% with a gradually saturated absorbent bed.

When the ammonia synthesis in the catalyst bed has not reached the thermodynamic equilibrium, the results indicate that, the wider residence time distribution can yield higher ammonia conversion to approach the thermodynamic equilibrium as shown in our model. Once this equilibrium is reached, the absorption could still increase the reaction conversion. Therefore, the possible reasons in Chapter 3 for the improvement have been verified that both the wider residence time distribution and the influence of absorption could improve the reaction per-pass conversion. Take the absorption effect as an example, if the backflow ratio is zero, the decrease in ammonia concentration or partial pressure caused by absorption will not affect the synthesis reaction. However, when the backflow ratio is greater than zero, the reactants with the reduced partial pressure of ammonia (ammonia was absorbed) will flow to upstream cells, speeding up the reaction and driving the equilibrium to the right.

In a previous back flow cell model of static mixers, the model parameters, number of cells and back flow ratio were determined from residence time distribution tracer studies [145]. The analytical expressions for the function of residence time distribution were implemented in MATLAB and fitted to experimental data by minimising the square error function with respect

to the number of cells and back flow ratio [145]. However, the residence time distribution tracer study was difficult to apply in this research due to the lack of the corresponding laboratory apparatus. Therefore, the only thing that could be done was analysing the sensitivity to the number of cells in the simulation and observing whether the simulation results trend fit that of the experiment data under a certain backflow ratio.

The reaction conversions from experimental results were 1.09% and 0.71%. These were much lower than the simulation conversion of a stoichiometric feed. However, the production rate in the experiments is consistent with the same order of magnitude of synthesis rate for Ru/MgO catalyst (1,500 $\mu molg^{-1}h^{-1}$ at 390 and 0.9 MPa) from the literature [152]. The low conversion is therefore mainly caused by the short residence time, especially when the reaction rate is low due to the mild operating conditions. At mild temperatures, the equilibrium is strongly in favour of ammonia, but the reaction does not proceed at a detectable rate [8]. Furthermore, the catalyst used in this chapter was a Ru catalyst, which was not identical to the one reported in the literature. This is thought to introduce errors in our simulation. Moreover, the kinetic expression for ammonia absorption used in this model is constructed from ammonia absorption in calcium chloride, which seems to be different from magnesium chloride. However, as the backflow effects on the per-pass conversion in the simulation show the same increasing trend as in reality, this model of the ammonia absorptive reactor can, to some extent, explain the experimental results.

There is still one more potential limitation to this simulation. The ammonia synthesis reaction is not equimolar (with 4 mol of reactants being converted to 2 mol of products), and absorption will only remove ammonia from the gas phase. In this simulation, the per-pass conversion of the reaction is quite low at about 5 – 7 %. Therefore, the volume change during the reaction and absorption processes was low enough to be ignored in this chapter.

4.5 Conclusion

In this chapter an advanced mathematical model, the transient BCM of the adjacent coupling

absorptive reactor was presented. In this model, the catalyst and absorbent beds were not regarded as two separate blocks, but as a single unit. A transient CM was taken as a reference to identify what role the absorbent plays in the enhancement of synthesis conversion.

Our analysis indicates that the cell number should be fixed between 8 and 12 to make the simulation results independent of the cell number at an acceptable computing cost. In this simulation, the length of each cell is fixed. Therefore, the key parameter for the simulation of the absorptive reactor is the cell number. As the cell number increased but under 8, the reaction conversion will be affected. However, the backflow effect is required to be compared. Therefore, the cell number should be with a certain range that cannot affect the reaction conversion. The bench-scale absorptive ammonia synthesis reactor was operated to obtain experimental data to verify this point. It still performed better than the conventional Haber Bosch process under milder operating condtions, as Ru catalyst was used. The measured Ru catalytic reaction rate in the experiment was found to be of the same order of magnitude as the literature value. The analysis of the reasons for the improvement provided by absorbents in an ammonia synthesis absorptive reactor in this chapter permits an assessment of how the production rate is improved: wider residence time distribution, and efficient ammonia separation by absorption. Modelling results indicate that both wider residence time distribution and absorption can affect the per-pass synthesis conversion when an absorbent is packed adjacently after the catalyst. Under a kinetically controlled regime, the wider residence time distribution has been proven to result in higher ammonia conversions approaching the thermodynamic equilibrium. If the equilibrium of reaction has been reached, the conversion can still be further improved because of the effect of absorption based on the simulation results in Figure 4.17, increasing from 7.45% to 11.2%. The simulation results support the suggestion that increasing the degree of backflow leads to a higher per-pass ammonia conversion. The suitable length of the absorbent bed has been investigated in this model, and has been estimated to be 0.06 m.

Based on experimental data in this chapter, the per-pass reaction conversions for the absorptive and conventional reactors were 1.09% and 0.71%, respectively. However, the simulation conversions are from 7.45% to 11.2% for the reason of absorption effect while from

6.25% to 7.25% for the reason of wider residence time distribution. Both numerical model and experiment indicate that the absorptive reactor has a higher per-pass conversion than the conventional reactor. Therefore, the simulation results can be qualitatively validated with the experimental results.

Potential sources of issue and shortcomings still exist in the simulation. Controlling the temperature of the absorbent bed is still difficult even with a lower temperature difference between the catalyst and absorbent beds, as a result this process is not operating under its optimal conditions. Furthermore, there was a deviation in the experimental performances compared to those predicted from our simulation, as the Ru catalyst used was not identical to the literature catalyst assumed in the simulation. And the kinetic expression for ammonia absorption used in this model is not constructed from absorption in magnesium chloride. Another limitation of this research is that the number of cells and backflow ratio could not be determined from residence time distribution tracer studies due to the lack of adequate experimental equipment. What we tried to do, instead, was analysing the sensitivity to number of cells in order to reduce the uncertainty of this model parameter. Since the simulation results trend at a certain backflow ratio fits experimental data, we could demonstrate that the backflow in the absorptive reactor can indeed promote the ammonia reaction per-pass conversion. Therefore, the models were validated with experimental data and found which could suggest the reactor performance of the adjacent coupling ammonia absorptive reactor and give the reasons for the improved performance.

Chapter 5. Computational fluid dynamics simulation of the adjacent-coupling ammonia absorptive reactor

5.1 Introduction

Simplified models of the adjacent coupling absorptive reactor were implemented using MATLAB in Chapters 3 and 4. The experimental phenomenon of absorption effect on the ammonia synthesis was simulated through the backflow concept. However, considering the complexity of the absorptive reactor, i.e. simultaneous balance of mass, momentum, and energy, and coupling with reaction, the utilisation of computational fluid dynamics (CFD) simulation can be a more effective approach. Therefore, in this chapter, a computational fluid dynamics model was developed to investigate the reason for the increment of ammonia per-pass production in the absorptive reactor. The convection–diffusion equations were used in this simulation, in which gases are transferred inside the system due to two processes: diffusion and convection. The convection–diffusion equation is obtained by combining the conservation equation for an infinitely small box with the equations describing advective and diffusive fluxes. Three kinds of ammonia synthesis reactor were simulated in this chapter: the absorptive reactor, non-absorptive reactor and conventional reactor. Considering the non-absorptive reactor was to separate flow effects from the absorption effects. Furthermore, the temperature deviation was also considered in this simulation.

In the present work, the absorptive, non-absorptive and conventional reactors were simulated through the commercial package ANSYS Fluent® v. 19.0, which is based on the finite control volume method. The comparison of the conventional reactor, non-absorptive reactor and absorptive reactor on ammonia per-pass conversion was studied operating under the same conditions as Chapter 4. In the simulation, the mass, momentum, and energy conservation equations were developed and computed [153]. The fixed-bed pellets were simulated by the porous media model in Fluent. Using the C programming language, a user defined function

(UDF) was written and compiled within the ANSYS Fluent code to calculate the kinetic rate of ammonia synthesis and ammonia absorption. Then, the characteristic contours in the reactor, such as the species mole fractions, pressure, and temperature, were generated and analysed.

5.2 Methodology

A two-dimensional computational fluid dynamics model was used to investigate the performance of three kinds of ammonia synthesis reactors, especially in terms of their per-pass conversion. The schematic diagrams are shown in Figure 5.1. The catalyst bed is referred by ‘C,’ the empty bed by ‘E,’ the inert-pellet bed by ‘I’, and the absorbent bed by ‘A.’ The three reactors are (a) the conventional reactor, (b) the non-absorptive reactor and (c) the adjacent coupling absorptive reactor. The simulation was based on the same operating conditions as the experimental setting. These vessels consisted of the same amount of catalyst, assumed under uniform operating pressure but at different temperature, high temperature in the catalyst bed and low temperature in the absorbent/empty/inert pellets bed, which is in line with the experimental setup in Chapter 4. The diameter of the cylinder is set to be 0.008 m.

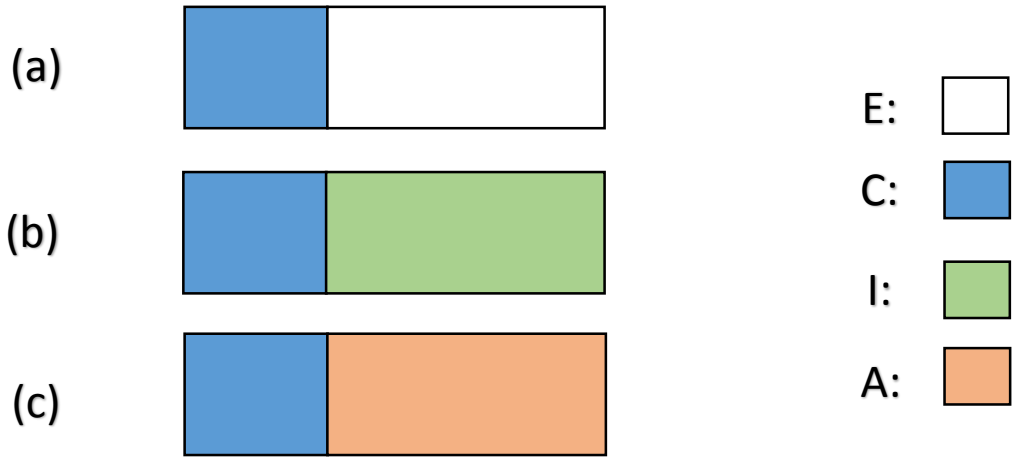

Figure 5.1. The schematic of three kinds of ammonia synthesis reactors.

The working fluid was a mixture of nitrogen and hydrogen as the input to the reactors. The properties of hydrogen, nitrogen, and ammonia were imported from the Fluent database. The properties of the $MgCl_2$ absorbent, such as heat capacity and enthalpy, were retrieved from [154], and are listed in Appendix C. The temperature gradient between the two coupled beds as well as the temperature distribution within the reactor was clearly illustrated in this study. The viscosity, thermal conductivity, and diffusion coefficient of each species were assumed to be constant. The catalyst, absorbent and inert pellets in the reactor cause resistance to the reactant flow, this was estimated using the porous medium model. The convection-diffusion model is applied in this simulation that corresponds to the 'backflow' in Chapters 3 and 4. The following assumptions were also considered in this simulation:

- The reactants had been well mixed before they were pumped into the fixed bed reactor.
- The gravitational body force was neglected.
- The porous media domain was utilized where the porosity of the catalyst and absorbent/ inert pellets zones was assumed to be isotropic.
- The catalyst/absorbent/inert pellets packing had the same voidage and particle size.
- Incompressible gas was assumed.

5.3 Governing equations

Given the operating conditions of 400 ^{o}C and 10 bar, the density of the fluid is 6 $kg \cdot m^{-3}$ and its viscosity 3.19×10^{-5} $Pa \cdot s$ [155]. The diameter of the particles in the fixed bed is assumed to be 2×10^{-4} m and the inlet velocity of the fluid 0.004 $m \cdot s^{-1}$. The voidage of the fixed bed is assumed to be 0.5, and so the flow in the fixed beds of the ammonia synthesis reactors was laminar with a Re = 0.3, which is suitably described by the laminar Navier-Stokes equations. The governing equations describe the flow, mass, and heat transfer behaviors of the fluid in the reactors. These equations were solved using the ANSYS Fluent® 19.0 solver, including the continuity equation:

$$\frac{\partial \rho}{\partial t} + \nabla \cdot (\rho \vec{u}) = 0 \tag{5.7}$$

where ρ is the density of the fluid, t is the time, and $\vec{u}$ is the velocity vector.

Momentum equation:

$$\frac{\partial}{\partial t}(\rho \vec{u}) + \nabla \cdot (\rho \vec{u}\vec{u}) = -\nabla p + \nabla \cdot (\bar{\bar{\tau}}) + \vec{F} \tag{5.8}$$

where $\bar{\bar{\tau}}$ is the stress tensor, p is the pressure, $\vec{F}$ is the external body force.

$$\bar{\bar{\tau}} = \mu \left[(\nabla \vec{u} + \nabla \vec{u}^T) - \frac{2}{3} \nabla \cdot \vec{u} I \right] \tag{5.9}$$

where μ is the dynamic viscosity, and I is the unit tensor. The second term on the right-hand side is the effect of volume dilation, which is equal to zero in this model.

Energy equation:

$$\frac{\partial}{\partial t}(\rho E) + \nabla \cdot (\vec{u}(\rho E + p)) = \nabla \cdot \left(k_{eff} \nabla T - \sum_k h_{e,k} \vec{J}_k + \left(\bar{\bar{\tau}}_{eff} \cdot \vec{u} \right) \right) + S_h \tag{5.10}$$

where k_{eff} is the effective conductivity, T is the temperature, h_e is the enthalpy, $\vec{J}$ is the diffusion flux, which arises due to gradients of concentration and temperature, and S_h is the heat source term, which originates from the chemical reaction.

$$E = h_e - \frac{p}{\rho} + \frac{u^2}{2} \tag{5.11}$$

where sensible enthalpy h_e is defined for incompressible flows as

$$h_e = \sum_k Y_k h_{e,k} + \frac{p}{\rho} \tag{5.12}$$

Species mass balance equations:

$$\frac{\partial}{\partial t}(\rho Y_k) + \nabla \cdot (\rho \vec{u} Y_k) = -\nabla \cdot \vec{J}_k + R_k \tag{5.13}$$

where Y is the mass fraction of each species, R_k is the net rate of production of each species by chemical reaction.

The catalyst and absorbent particles in the reactor produce resistance to the flow. The drag force is calculated by the porous medium model and added to the momentum equations as $\vec{F}$. This source term is composed of two parts: a viscous loss term, the first term on the right-hand side of Equation (5.14), and an inertial loss term, the second term on the right-hand side of Equation (5.14).

$$F = -(\sum_{j'=1}^{2} D_{pre}\mu u_{j'} + \sum_{j'=1}^{2} C_{pre}\frac{1}{2}\rho|u|u_{j'}) \tag{5.14}$$

where F is the source term for the momentum equation, and $|u|$ is the magnitude of the velocity. D_{pre} and C_{pre} are matrices in Fluent's default setting.

In this simulation, the diffusivity refers to the molecular diffusivity. Molecular diffusion is caused by random motion of molecules caused by collisions with other molecules (Brownian motion). This process occurs regardless of whether the fluid has any form of bulk motion and is characterised by the molecular diffusivity. It is often considered as causing by gradients in concentration of a molecular species. Fick's law is approximated to model mass diffusion only caused by the concentration gradient in this study; therefore,

$$\vec{J}_k = -\rho D_{k,m}\nabla Y_k \tag{5.15}$$

where $D_{k,m}$ is the mass diffusion coefficient for species k in the mixture. The kinetic theory of gases was used in Fluent simulation to calculate the molecular diffusivity.

The ammonia synthesis and absorption rates for laminar flows appeared as source terms in Equation (5.13). Cs-promoted Ru catalyst was chosen for ammonia synthesis in this chapter, which is in line with the experiment in Chapter 4. The kinetic equation of Ru catalyst for ammonia synthesis was found to be affected markedly by the kind of support or promoter [156]. Moreover, the pressure also has a great impact on the kinetics of ammonia synthesis over Ru catalyst [157]. Kinetic data of ammonia synthesis over Ru catalysts was obtained in [158] as the following power rate form, but the range of reaction conditions covered is insufficient to select appropriate data for this case.

$$R_{NH_3(cat)} = k^* p_n^{x_{Ru}} p_h^{y_{Ru}} p_a^{z_{Ru}} \quad (5.16)$$

k^*, x_{Ru}, y_{Ru} and z_{Ru} can be achieved from the experimental parameter under the specific reaction condition. Similarly, this power-law rate expressions were derived at high pressure up to 50 bar [159]. The modified Temkin equation is the another kinetic modelling, which has been carried out under high pressure 50-100 bar [160] of Ru/C catalyst. However, there is no kinetic expression of ammonia synthesis over Cs-promoted Ru catalyst under mild conditions such as low pressure at 10 bar. Therefore, the value of ammonia synthesis rate at 10 bar changing from 270 to 450 ˚C obtained from Figure 5.2 [76] was chosen as the input of this simulation. Based on this volcano-shaped curve of the Cs-promoted Ru Catalyst, we can have an approximate function for the ammonia synthesis rate and temperature for Cs-Ru catalyst. Then, we can get the synthesis rate at the simulation conditions of 400 ˚C and 10 bar. The mole fraction of ammonia at equilibrium under 400 ˚C and 10 bar is 5%, based on data in Figure 5.3 [132].

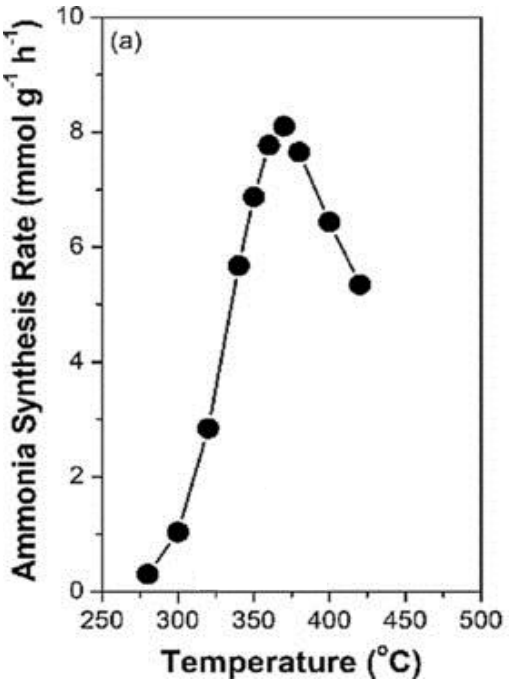

Figure 5.2. The ammonia synthesis rate as a function of reaction temperature over the prepared Cs−Ru catalysts [76].

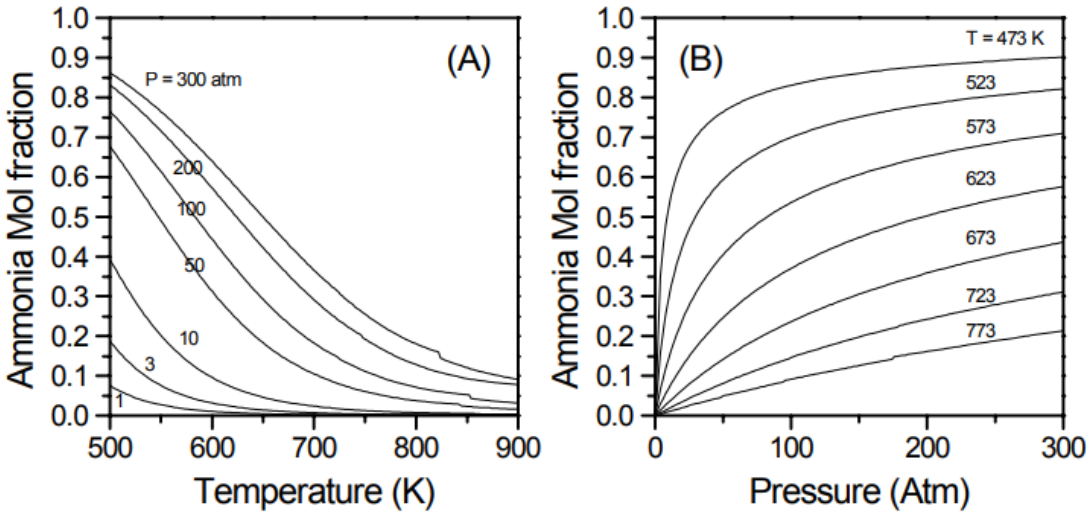

Figure 5.3. Mole fraction of ammonia at equilibrium from an initial mixture of 1:3 N_2/H_2 gas at (A) at different temperatures at a fixed pressure, and (B) at different pressures at a fixed temperature [132].

The kinetics of ammonia absorption into magnesium chloride are measured in terms of the ammonia pressure change at the temperature range 170 - 430°C [114]. The dependence of absorption rate on temperature was also investigated. For ammonia absorption, the rate of absorption is governed by both chemical kinetics and diffusion. The uptake of ammonia (in mol/s) is described by [114]:

$$R_{NH_3(abs)} = \frac{V}{RT}\frac{dp}{dt} = -AK_{ab}(p - p^*) \tag{5.17}$$

where V is the vessel volume, R is the gas constant, T is the temperature, p is the pressure, A is the surface area of the absorbent, and t is the time. The pressure p^* is the value of the pressure at equilibrium, when no further uptake occurs. The equilibrium pressure for different temperatures can be obtained from the literature [6].

The parameter K_{ab} is described by [114]:

$$K_{ab} = \left(\sqrt{\frac{D}{\pi t}}\right) H \tag{5.18}$$

where D is the diffusion coefficient of ammonia in the solid, and H is a partition coefficient, i.e. the ratio of the ammonia concentration in the solid, in moles per volume, to the ammonia

pressure. These approximate diffusion and partition coefficients (D and H) of ammonia in magnesium chloride are listed in Appendix C. Based on the results in Chapter 3, an exotherm of about 20 ˚C is observed (caused by exothermal absorption [114]) in the absorbent bed. This small exotherm is unlikely to significantly influence the diffusion coefficient and isothermal operation was assumed to be an acceptable approximation. Therefore, the data for the absorbent at 150 ˚C is approximated by the data at 170 ˚C in Table C.2 of Appendix C.

5.4 Numerical procedures

5.4.1 Geometric model and meshes

The ammonia synthesis reactors were investigated in the form of a horizontal column, with 0.8 cm diameter and three-centimetre length. The length of the catalyst bed is one centimetre and the absorbent/empty/inert-pellet bed is two centimetres. The flow domain of the reactors is discretised into a finite set of control cells. The discretised domain containing these cells is called the mesh. Governing equations are then solved for each cell to calculate variables such as the mole fraction of species, temperature and pressure. To discretise the domain for solving the governing equations via the finite volume approach, the ANSYS ICEM CFD® was used. In this case, the structured grids were used, and the shape of cells is rectangular. Quadrilateral meshes are much more computationally efficient than triangular meshes. The numbers of nodes, faces, and cells in the mesh are displayed in Table C.1 of Appendix C with explanation of these concepts.

To obtain accurate results and quick convergence, a high-quality mesh is required in the simulation. There are numerous ways to define and control the quality of a generated mesh, like the minimum orthogonal quality. The concept of mesh orthogonal quality relates to how close the angles between adjacent elements faces are to some optimal angle - 90˚. The orthogonal quality measure ranges from 0 (low quality) to 1 (good quality). In this case, it equals 1, the best meshing, as the grids were structured. Aspect ratio, defined as the ratio of the shortest edge length to the most extended, ideally equals 1. In this model, the mean aspect

ratio was 0.99998. Meshing the computational domain appropriately is the primary step to obtain accurate simulation results.

To ensure that the results are mesh independent, the domain was meshed with a different number of quadrilateral elements. A mesh-independent solution should converge by repeating the calculation on a series of successively refined meshes. The independence of the mesh has been taken into account. Considering the cost of simulation, the simulation results can be independent from the mesh size within the allowable error when the maximum global element seed size is no higher than 0.01 cm.

5.4.2 Boundary and initial conditions

To compare the performance of the absorptive, non-absorptive, and conventional reactors, the boundary and initial conditions used were kept the same for both cases. The boundary condition applied at the inlet to the computational domain was ‘velocity inlet’; at the outlet, ‘pressure outlet’; while the ‘wall’ boundary condition describes others. Inlet boundary conditions for the computational domain were specified by the Dirichlet conditions that both velocity and temperature profiles were assumed to be uniform and constant. The velocity magnitude was set normal to the boundary. At the outlet, zero derivative values of velocity and temperature along the flow direction were assumed. The stationary walls were defined with the no-slip shear condition. The velocity components equalled zero, and a zero-gradient condition for all species was assumed at the walls. As for the initial conditions, the pressure was set as 10 bar. Meanwhile, a 3:1 mixture of H_2 and N_2 was set. The operating parameter values are detailed in Table 5.1.

Table 5.1. Operating parameters used for model simulation.

Parameter	**Value**
Hydrogen inlet to the reactor	75 mol%
Nitrogen inlet to the reactor	25 mol%
Ammonia inlet to the reactor	0 mol%
Initial pressure	10 bar
Gas inlet velocity	0.004 m/s
Viscous model	Laminar
Initial temperature of the reactor column	300 ˚C
Initial $N_2/H_2/NH_3$ ratio in the reactor column	1 : 3 : 0
Temperature of the inlet flow	400 ˚C
Temperature at the wall of the catalyst bed	400 ˚C
Temperature at the wall of the absorbent/empty bed	150 ˚C
Temperature at outlet	150 ˚C

5.4.3 Numerical methods

The Navier-Stoke equations were solved by the SIMPLE algorithm, the pressure-based algorithm of Fluent. The Semi-Implicit Method for Pressure Linked Equations (SIMPLE) algorithm, the pressure-based algorithm of Fluent, employs a relationship between velocity and pressure corrections to enforce mass conservation and to obtain the pressure field. The second-order discretisation scheme was applied for all of the model equations. In the process of simulation, the catalyst and absorbent/inert-pellet beds were simplified through a porous media model. The resistance loss in the catalyst and absorbent/inert-pellet zones was simulated through this porous media model. The ammonia synthesis and absorption are considered as volumetric reactions. Using the C programming language, a user-defined function (UDF) was written and compiled within the ANSYS Fluent code to calculate the kinetic

rate of ammonia synthesis and ammonia absorption. The unsteady-state calculation solver was used with a time step size of 0.1 s.

5.5 Simulation results and discussion

Results were represented and analysed through the contour and XY plots. The XY plots were created by using data from surfaces and modifying the axis and curve attributes. The contours of temperature, pressure and mole fractions of ammonia, as well as the XY plots, were produced for the three reactor configurations.

Figure 5.4 displays the temperature distribution in the conventional, non-absorptive and absorptive reactors. The reactor was laid horizontally and the gas flow entered from the left of the vessel. A localized temperature gradient zone is located at the junction of the catalyst bed and the absorbent/empty/inert-pellet bed. The catalyst bed is enclosed within a black rectangle, while the absorbent/empty/inert-pellet bed is within a red rectangle. It is interesting to note that, under the specified boundary conditions, conventional and absorptive reactors yield a very different temperature field, while the non-absorptive reactor has a similar temperature distribution as the absorptive one. For the conventional reactor, temperature variation in the empty bed takes the shape of a vortex. This was caused by the flow entering into the empty bed without any obstacles, i.e. without a fixed bed. Therefore, the flow has a sudden increase in velocity, leading to flow turbulence. However, regarding the absorptive and non-absorptive reactors, the temperature variation is symmetrical in both the catalyst and absorbent/inert-pellet beds. The isotherms could be divided into two different sections, in the catalyst bed it is left-convex, and in the absorbent/inert-pellet bed right-convex. Therefore, the average temperature in the catalyst bed of the absorptive reactor is somewhat lower than that in the conventional reactor, which may lead to a decrease in the synthesis rate. However, the temperature changes in the absorbent bed of the absorptive reactor are relatively smaller and cover less area, which could justify the neglect of the impact of temperature variation on the absorption rate.

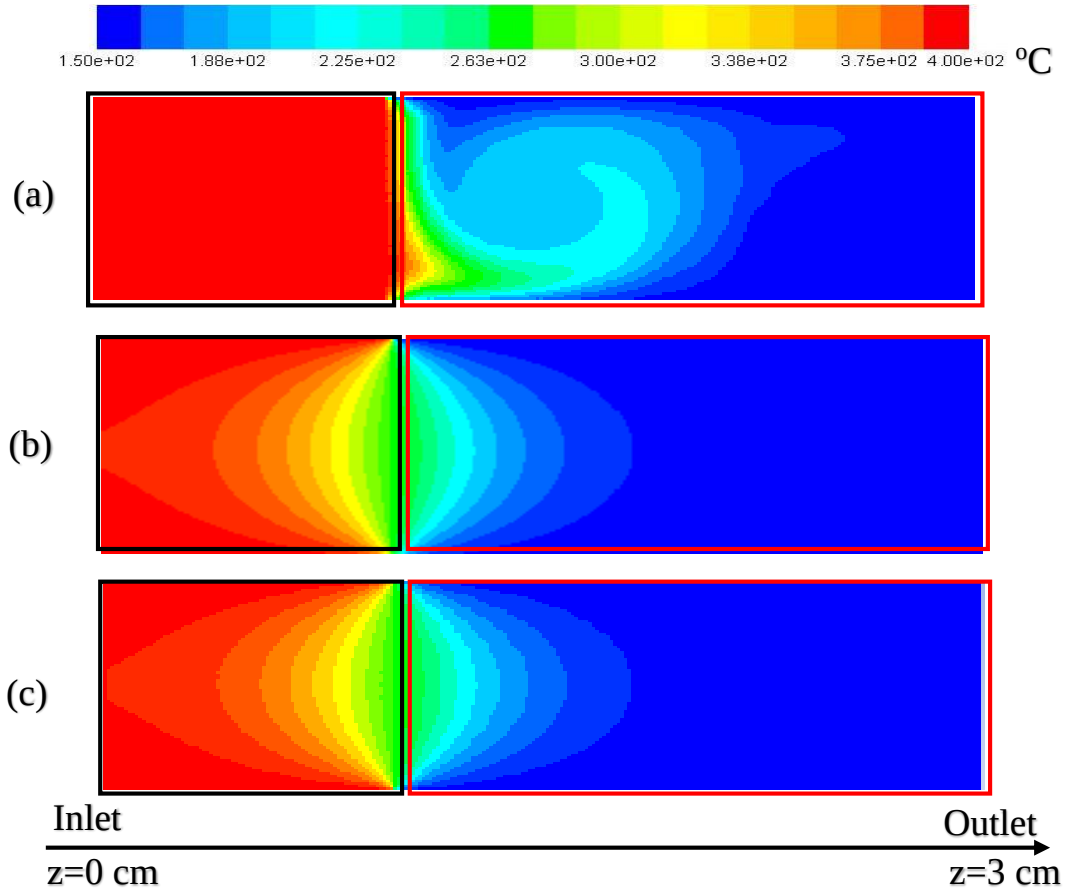

Figure 5.4. Contour plots of temperature (°C) in the three configurations of the ammonia synthesis reactor: (a) conventional reactor (b) non-absorptive reactor and (c) absorptive reactor. The colormap alignment is on the top.

Figure 5.5 exhibits the static pressure at the central longitudinal axis of the three reactors. The pressure profiles are essentially constant along all the reactors (absorptive reactor, non-absorptive reactor or conventional reactor). In reality, the friction drag produced by the catalyst and absorbent/inert particles could lead to the loss of pressure even the fixed bed is only 1 to 3 cm. However, this simulation is carried out as the pressure at the outlet is assumed to be the same as the initial pressure. Therefore, the packed-bed reactors is recognized as under uniform pressure condition in the simulation.

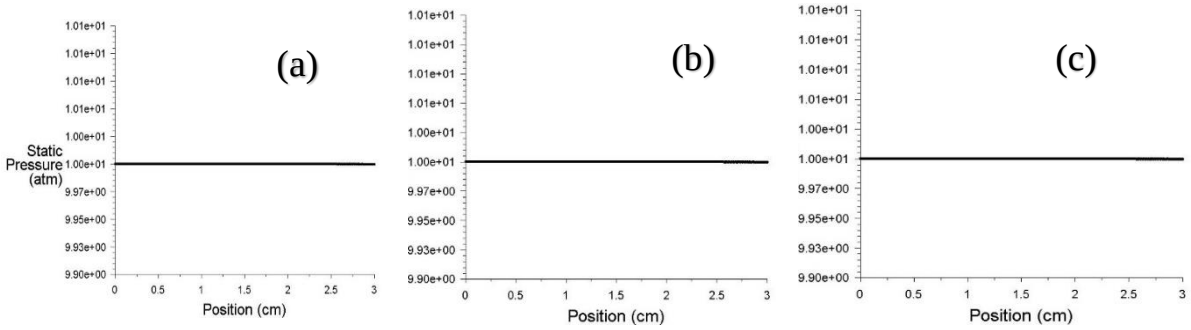

Figure 5.5. The static pressure (atm) at the central longitudinal axis of (a) conventional reactor (b) non-absorptive reactor and (c) absorptive reactor.

Figure 5.6 displays the pressure distribution in the absorptive reactors. The reactor was laid horizontally and the gas flow entered from the left of the vessel. It is interesting to note that the pressure is distributed uniformly through the reactor, at 10 bar. There is still a small pressure differential, which however could be neglected for the impact of pressure variation on the absorption rate.

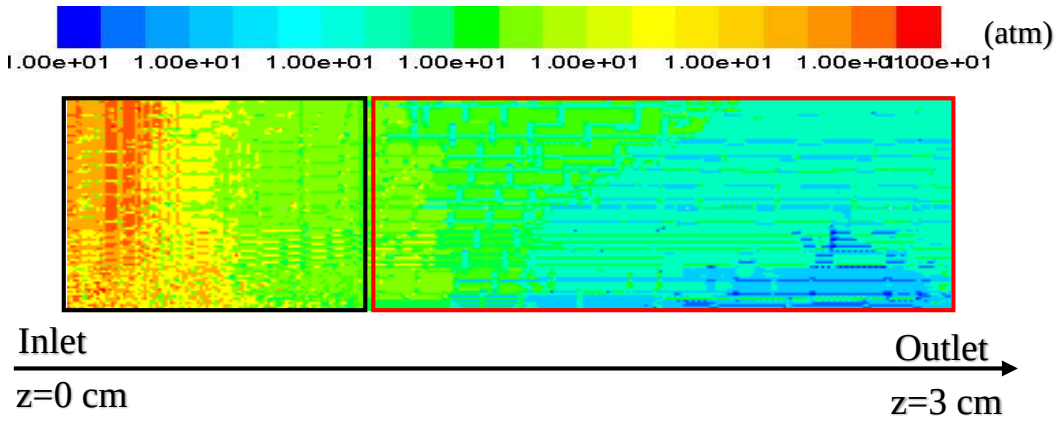

Figure 5.6. Contour plots of pressure (atm) in the absorptive ammonia synthesis reactor. The colormap alignment is on the top.

Take, for example, the absorptive reactor, for the variation of species that can be observed and analysed. Figure 5.7 depicts the variation of ammonia mole fraction as a function of time from 0.1 s to 5 s in the absorptive reactor. The reaction occurs when the hydrogen and nitrogen flow through the catalyst zone. Ammonia is produced in the catalyst bed. It is observed that, after the catalyst bed, the mole fraction of ammonia decreased as the fluid passes through the absorbent bed and ammonia is absorbed in this zone. The mole fraction of ammonia reaches a peak within the catalyst bed. This peak is moving to the end of the catalyst bed as time increases and the reaction accumulates: the mole fraction of ammonia at 0.1 s is only 0.46% while it increases to 4.8% at 5 s. After calculating the reaction conversion (details in Appendix C), it increases from 0.9% at 0.1 s to 9.2% at 5 s. The contour plots are nearly constant as the reaction reaches a steady-state after 10 s.

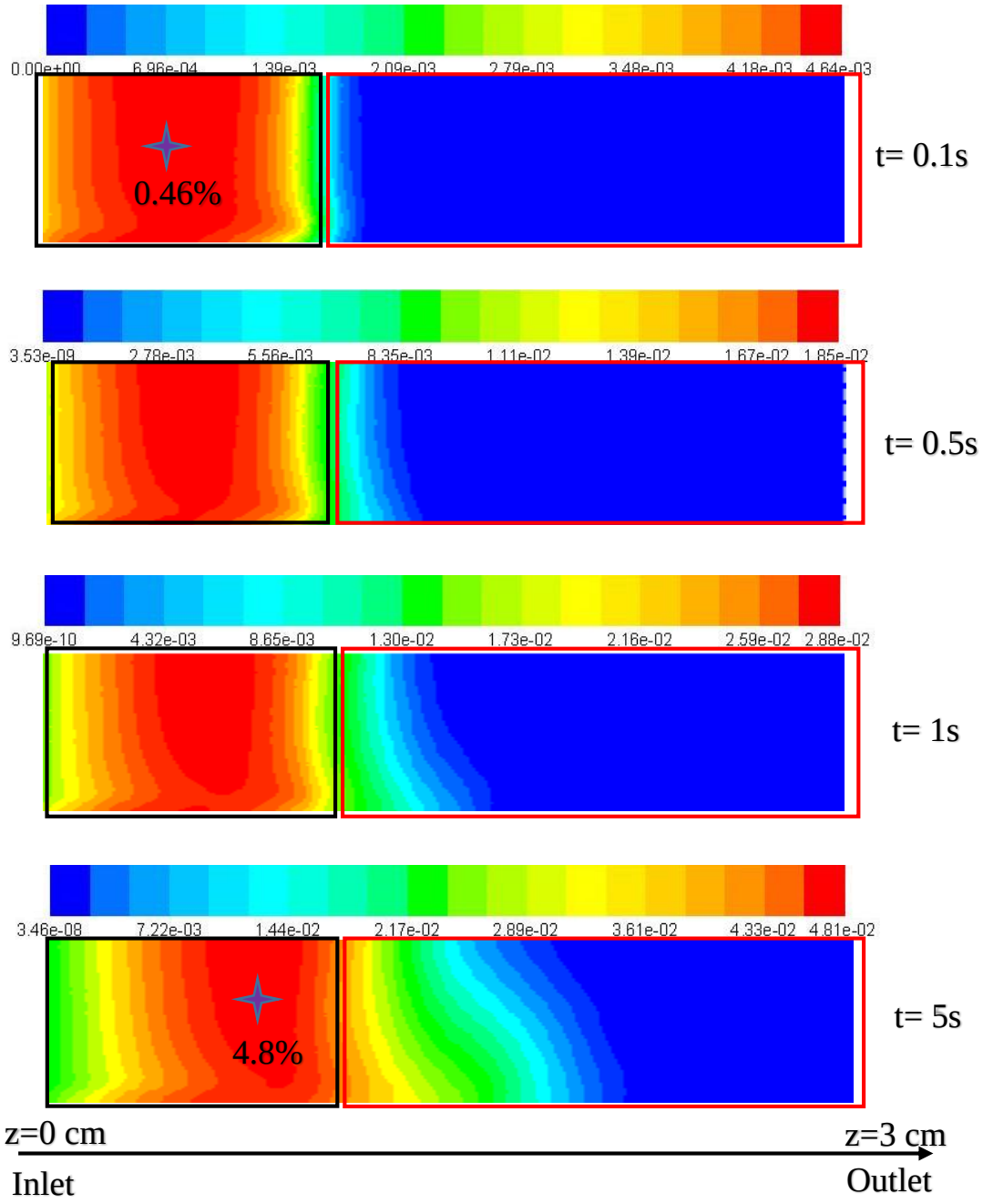

Figure 5.7. Contour plots of ammonia mole fraction in the absorptive reactor at intervals of 0.1, 0.5, 1, and 5 s time. The colormap of the mole fraction ranges are different for each of the cases and aligned on the top of each case.

Figure 5.8 displays the contour plots of ammonia mole fraction in the conventional, non-absorptive and absorptive reactors, respectively, at 10 s. The mole fraction of ammonia peaks at the end of the catalyst bed. For the absorptive reactor in Figure 5.8(c), the ammonia fraction

decreases in the absorbent bed as ammonia is absorbed. Similarly, in the conventional and non-absorptive reactors, the mole fraction of ammonia is lower in the empty/inert-pellet bed than in the catalyst bed, shown in Figure 5.8(a) and 5.8(b). However, this is not caused by the separation of ammonia but because ammonia is diluted in this zone. Due to the simulation setting, this zone is filled with unreacted nitrogen and hydrogen before the produced ammonia flows through. Then, the ammonia is diluted leading to a lower mole fraction distribution.

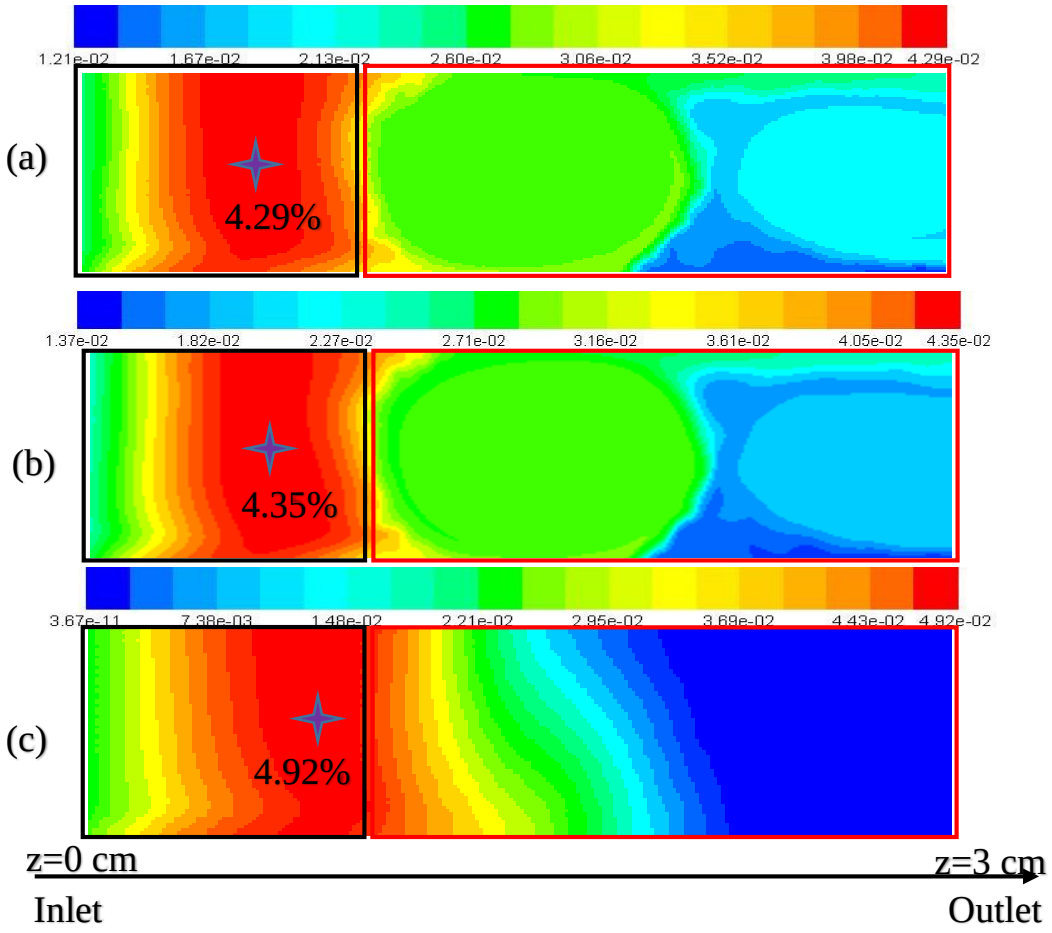

Figure 5.8. Contour plots of the ammonia mole fraction in the three reactor configurations: (a) conventional reactor (b) non-absorptive reactor and (c) absorptive reactor. The colormap of mole fraction ranges is different for each of the cases and is aligned on the top of each case.

The contour plots of ammonia mole fraction are almost the same for the conventional and non-absorptive reactors, reaching 4.29% in the conventional reactor and 4.35% in the non-absorptive reactor. However, the mole fraction of ammonia reaches 4.92% in the absorptive

reactor, which is higher than that in the other two. Therefore, the effect of the resistance flow caused by the absorbent on the ammonia production rate is slight compared with its absorption ability. The reaction conversion is 8.2% in the conventional reactor and is 9.4% in the absorptive reactor after 10 s running. Therefore, the per-pass conversion in the absorptive reactor has grown by 14% over that in the conventional reactor. This coincided with experimental results showing that the production rate of ammonia in the absorptive reactor is higher than that in the conventional reactor. The main reason for the difference between experimental and simulation results in this chapter may because our catalyst used (MgO supported) was still not identical to the literature catalyst (carbon supported). In this simulation, the kinetic data used for Ru catalyst was different from Chapter 4, and therefore the simulation results were a little different.

According to Figure 5.8, the per-pass conversion in the absorptive reactor is higher than for the conventional and non-absorptive reactors. The reason for this increment is further discussed through Figures 5.9 and 5.10. Figure 5.9 displays the mole fraction of ammonia at the central longitudinal axis of the absorptive reactor. The trend of ammonia mole fraction is according to expectations: it increases through the catalyst zone and then decreases in the absorbent zone. However, the decreasing trend starts at the end of the catalyst bed, as shown in Figure 5.9. Meanwhile, the mole fraction of nitrogen has a corresponding increase at the end of the catalyst bed, displayed in Figure 5.10. This indicates the presence of ammonia diffusion within the absorptive reactor, showing that the absorbent bed can affect ammonia synthesis in the catalyst bed. As the partial pressure of ammonia decreases, it speeds up the reaction rate and drives the reaction to the right.

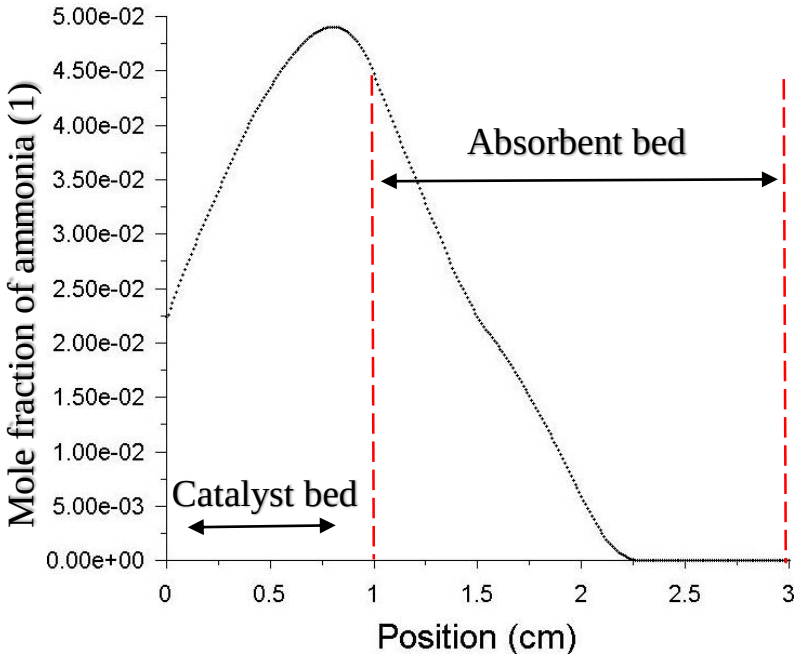

Figure 5.9. Mole fraction of ammonia at the central longitudinal axis of the absorptive reactor.

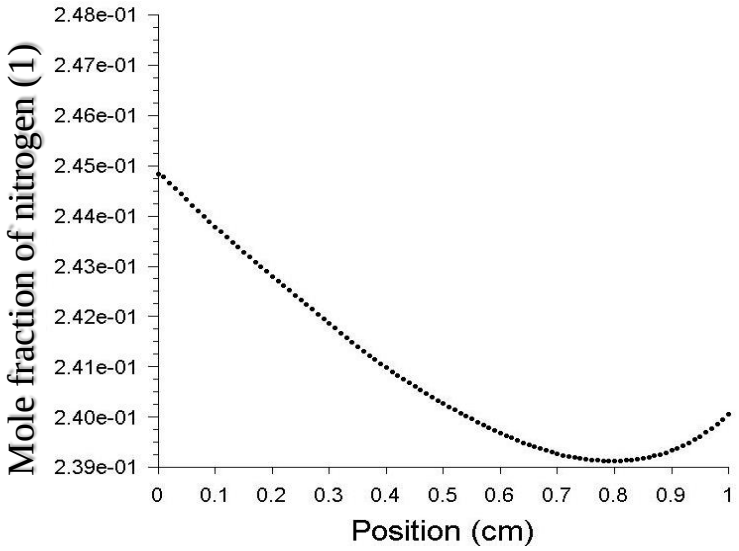

Figure 5.10. Mole fraction of nitrogen for the catalyst bed in the absorptive reactor.

Therefore, improved per-pass conversion is mainly because of the absorption capacity of the absorptive reactor. Chapters 3 and 4 used the 'backflow' concept to explain the reason for the higher efficiency of the adjacent-coupling absorptive reactor, while in Chapter 5, the species

diffusion mechanism was the reason for the interaction between ammonia synthesis and absorption. It could be concluded that the improved conversion is, to a large degree, because of the absorption capacity of the absorptive reactor, which causes an increase of ammonia production rate, and therefore a higher per-pass conversion.

5.6 Conclusion

A computational fluid dynamics simulation was presented to evaluate the effects of an absorbent bed in an absorptive reactor for ammonia synthesis. The convection-diffusion model was simulated using the commercial CFD software ANSYS Fluent. The developed CFD simulation coupled thermal and flow processes with ammonia synthesis and absorption, and produced results which were physically correct. The temperature profiles were estimated for the conventional, non-absorptive and absorptive reactors with a temperature gradient zone located at the junction of beds. It also provided detailed results of the species mole fraction and presure profiles in the three reactor configurations. The simulation proved that pressure loss could be neglected at laboratory scale.

The effect of absorption was manifested in the contrast between the conventional reactor, non-absorptive reactor and the absorptive reactor. To determine the effect of the absorbent bed on reactor performance, the non-absorbent reactor case was run in the CFD simulation, first taking into account the absorption properties, and second, without it. The mole fractions of ammonia were found to have obvious increase in the presence of absorbent, while the effect in the non-absorbent case was very small. This simulation confirms the conclusion of Chapter 4, i.e. that the absorption indeed has an effect on the per-pass conversion even if the equilibrium has not been reached. It also confirms that both flow and absorption effects are beneficial to the efficiency of the ammonia synthesis. Furthermore, our analysis indicates that the flow effect is anticipated to be less important than the effect of the absorbent capacity, as shown by the simulation results. The increased per-pass synthesis conversion was mainly

caused by ammonia absorption, which reduced the partial pressure of ammonia and led to a faster reaction rate, resulting in a higher per-pass conversion.

The reaction conversions from experimental results were 1.09% and 0.71% for the absorptive and conventional reactors respectively. The per-pass conversion had a 1.5 times increase. However, based on the simulation results, the absorption influence is not significant as the conversion was improved from 8.2% to 9.4%, just over 1.15 times increase. The increment in productivity caused by the absorption is only to a lesser degree as the influence of diffusion is less than the convection for the species transport. Thus, a multi-bed absorptive reactor is proposed in Chapter 6 to achieve a high per-pass conversion absorptive reactor for ammonia synthesis.

The computational results agree well with data from the literature but not with experimental values. The mole fraction of ammonia in the computational results reaches 4.92% in the conventional reactor, which is close to the literature reference 5% [132]. This discrepancy between the simulation results and experiment data is because the catalyst used (MgO supported) was not identical to the literature catalyst (carbon supported). However, this proposed model of absorptive reactor predicts an improvement on ammonia per-pass conversion comparable with the available experimental data. We have shown that there is no reason to be concerned that the increased production rate might not be accommodated by the absorbent. This type of model might help to design other absorptive reactors in the future, such as the multi-bed absorptive reactor.

Chapter 6. Computational fluid dynamics simulation of the multi-bed ammonia absorptive reactor

6.1 Introduction

For the adjacent coupling absorptive reactor in Chapters 3, 4 and 5, the per-pass conversion of the vessel was increased compared with the conventional reactor. However, the increased conversion was still below the equilibrium level and the increment is not much. Furthermore, at an industrial scale the temperatures in the catalyst and absorbent beds would be difficult to be precisely controlled at different levels, and any deviation will have a non-negligible effect on the kinetics of reaction and absorption. Therefore, it is desirable to reduce the temperature difference between the two beds to zero. This chapter models a multi-bed absorptive reactor under uniform operating temperature, in which the equilibrium of ammonia synthesis in the catalyst bed is reached. The multi-bed coupled absorptive reactor contains more than two beds of catalyst or absorbent pellets, and the operating condition is the same for all the beds through the vessel. We assume that the uniform operating temperature for the multi-bed absorptive reactor is feasible for future experiments. The production of ammonia is exothermic as the enthalpy of reaction (ΔH) is -45.7 kJ·mol^{-1} [132]. Similarly, the standard enthalpy change corresponding to the direct formation of $Mg(NH_3)_6Cl_2$ and $Mg(NH_3)Cl_2$ from $MgCl_2$ were measured experimentally to be −58 ± 6 kJ·mol^{-1}, and −64 ± 1 kJ·mol^{-1}, respectively [161]. Therefore, a cooling jacket with different heat transfer duties corresponding to the catalyst and absorbent beds would be required to remove the heat released from reaction or absorption, only then a uniform operating temperature could be maintained for the multi-bed reactor. Based on the energy calculation in Chapter 3, the heat released in the lab scale is negligibly small. Therefore, these exothermic effects would not be considered in this chapter. In this chapter, a new perspective of the absorption-enhanced ammonia synthesis, the multi-bed

coupled absorptive reactor, was simulated to improve its performance and the results were presented.

The catalyst used in the multi-bed absorptive reactor should be effective even under low operating temperatures to match the optimal temperature of absorption. Several catalysts can work under low temperatures, such as activated carbon-supported and Cs-promoted Ru catalyst (Cs-Ru/AC), which can be operated at 280-450 °C [76]. At temperatures below 300 °C, Ru and Co catalysts on the barium-doped calcium amide (Ba-Ca[NH_2]$_2$) enhances the efficiency of ammonia synthesis by two orders of magnitude with respect to a conventional Ru catalyst [162].

A wide variety of ammonia absorbent materials have been studied, amongst them metal halides (including magnesium, calcium, strontium and barium chloride and bromide), borohydrides, and zeolites. Magnesium chloride has one of the highest ammonia absorption capacities of the metal chlorides (9.1% hydrogen by weight) and is, therefore, one of the more widely studied ammonia absorption materials [163], which can also work under relatively high temperature. The ammonia absorption on magnesium chloride has been measured in the temperature range of 170 to 430 °C [114]. This high absorption capacity, even under high operating temperatures, makes it a promising absorbent for the absorptive reactor, and therefore, it was initially chosen for the multi-bed absorptive reactor. $Mg(NH_3)_6Cl_2$ is directly formed at room temperature by the reaction between magnesium chloride and ammonia without the formation of $Mg(NH_3)Cl_2$ and $Mg(NH_3)_2Cl_2$ even though these are more stable phases than $Mg(NH_3)_6Cl_2$. At 100 °C, the formation of $Mg(NH_3)_2Cl_2$ is realized. Furthermore, it is found that $Mg(NH_3)Cl_2$ can be formed at a temperature higher than 300 °C [161].

The operating temperature in our simulations is uniform for all catalyst and absorbent beds; therefore, this temperature should be appropriate for both catalyst and absorbent. As the working temperature range for Ru catalyst is from 270 to 470 ˚C [76], the operating temperature should not be lower than 270 ˚C. Meanwhile, if the operating temperature is higher than 300 ˚C, the ammonia absorption capacity of magnesium chloride would reduce from (ammonia: magnesium chloride) 2:1 to 1:1. Therefore, to achieve a higher absorption capacity

while the catalyst still have high activity, the operating temperature of the multi-bed absorptive reactor was chosen to be 300 °C.

The equilibrium temperature and pressure of the reversible ammonia absorption ($Mg(NH_3)_2Cl_2$) are shown in a Clausius-Clapeyron diagram [164]. When the temperature is 300 °C, the equilibrium pressure of ammonia absorption is about 33 bar. Therefore, the operating pressure should be higher than the absorption equilibrium pressure. If the operating pressure of ammonia synthesis is only 50 bar at 300 °C, then, the partial pressure of ammonia after production would reach about 20 bar [132], which is lower than the absorption equilibrium pressure. Therefore, the operating pressure was set to 100 bar, for which the partial pressure of ammonia could reach to about 50 bar that higher than the equilibrium pressure. A pressure higher than 100 bar can also be workable, but considering that this would be very energy-intensive, we assume a 100 bar operating pressure for our simulations.

For the multi-bed configuration, each absorbent bed preceding the catalyst bed will drive the reaction to the right in the next catalyst bed as the ammonia produced in the previous bed is absorbed. Therefore, the per-pass conversion of the reactor will increase, and the absorptive reactor for ammonia synthesis will achieve a higher per-pass conversion than in the conventional Haber-Bosch reactor. To find the improved reactor design, the configuration of the absorptive reactor, including the length of each bed and the number of beds, is investigated.

In this chapter, the multi-bed absorptive reactor was also modelled with ANSYS Fluent to simulate the effect of absorbents. A two-dimensional geometric model was set up to study the effect of different internal configurations on the per-pass conversion in absorptive reactors. The configuration of the reactor affects its final performance, i.e. its conversion to ammonia. The laminar Navier-Stokes equations were used with constant temperature through the flow field. Governing equations were solved numerically, and the results were evaluated. For example, the contours of the species mole fractions in the reactor were analysed. The results indicate that the multi-bed absorptive reactor can increase the ammonia per-pass conversion to a quite high level, almost 100%, and therefore, make the reaction more efficient than in a conventional Haber-Bosch reactor.

6.2 Methodology

A two-dimensional computational fluid dynamics model, developed in ANSYS Fluent v. 19.0, was used to investigate the performance of the multi-bed absorptive reactor of ammonia synthesis. Uniform operating conditions were used in the multi-bed absorptive reactor, especially the operating temperature. The vessel to be constructed for a pilot-scale fixed bed consisted of multiple catalyst and absorbent beds with the same amount of catalyst (1 cm length), but different amounts of absorbent (1 and 2 cm length). Regarding four-bed absorptive reactors, for example, the CFD simulation was conducted with two different configurations: (i) 1-cm catalyst bed with 1-cm absorbent bed alternately, which is expressed as 1-1-1-1 configuration, and (ii) 1-cm catalyst bed with 2-cm absorbent bed alternately, referred to as a 1-2-1-2 configuration. The schematic diagram of the multi-bed absorptive reactor is illustrated in Figure 6.1. The catalyst bed in Figure 6.1 is referred by 'C' and the absorbent bed by 'A'.

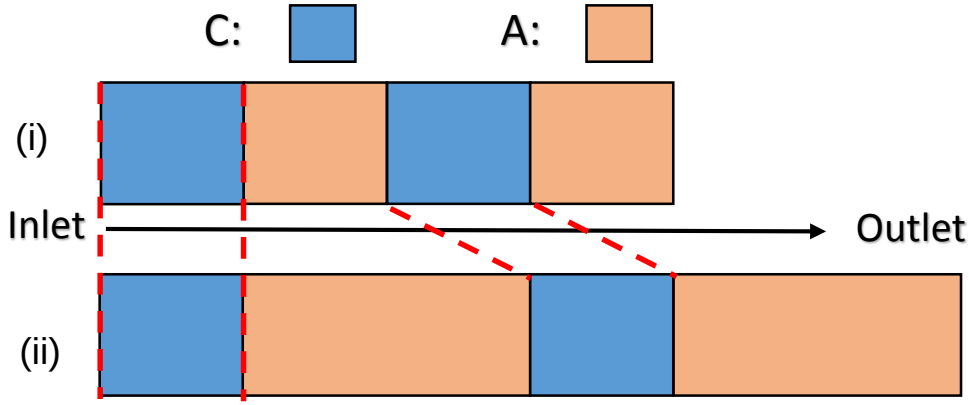

Figure 6.1. The schematic of two configurations of the multi-bed absorptive reactor.

The working fluid was a mixture of nitrogen and hydrogen at the feed. The properties of the hydrogen, nitrogen and ammonia were imported from the Fluent database. Since the reactor operates under constant temperature, the density, viscosity, thermal conductivity, and diffusion coefficient for each species were constant. Furthermore, the porous medium model was applied for the fixed beds. The assumptions considered in this CFD simulation were in

agreement with those in the adjacent-coupling absorptive reactor model in Chapter 5. These two kinds of configuration were compared to investigate the improved per-pass conversion of a multi-bed absorptive reactor.

6.3 Governing equations

Given the operating conditions of 300 ºC and 100 bar, the density of the gas mixture is about 60 kg · m^{-3} and its viscosity 2.9×10^{-5} Pa · s [155]. The diameter of the particles in the fixed bed is assumed to be 2×10^{-4} m and the inlet velocity of the fluid 0.01 m · s^{-1}. The voidage of the fixed bed is assumed to be 0.5, and so the flow in the fixed beds of the ammonia synthesis reactors was laminar with a Re = 8.3, which is suitably described by the laminar Navier-Stokes equations, same as the equations used in Section 5.3.

However, the kinetic rates of ammonia synthesis and absorption are different from those in Chapter 5 as the operating conditions are different. The pressure is 100 bar in this simulation, which is ten times the pressure in Chapter 5 and temperature is 300 °C, lower than that in Chapter 5. Based on the rate equation of ammonia synthesis:

$$R_{r,NH_3} \propto p_{N_2} {p_{H_2}}^3 {p_{NH_3}}^{-2} \tag{6.1}$$

And when the ideal gas law is applied, $pV = nRT$, we have the effect of pressure on the synthesis rate:

$$\frac{{R_{r,NH_3}}^1}{{R_{r,NH_3}}^2} = \left(\frac{p_1}{p_2}\right)^2 \tag{6.2}$$

Therefore, the synthesis rate at 300 °C and 100 bar can be estimated. The mole fraction of ammonia at equilibrium under 300 °C and 100 bar is 52%, obtained from Figure 5.3.

As for the absorption rate, it can be calculated through Equations (5.17) and (5.18). The approximate diffusion coefficients required at 300 °C are listed in Appendix C, Table C.2.

6.4 Numerical procedures

6.4.1 Geometric model and meshes

The multi-bed absorptive reactor consisted of alternating fixed beds of catalyst and absorbent inside a horizontal tube. This absorptive reactor was investigated with a one-centimetre diameter and four-centimetre or six-centimetre length. The flow domain of the absorptive reactor was discretised into a finite set of control cells, developed via ANSYS ICEM CFD®. Governing equations were then solved for each cell to calculate the mole fraction of each species. In this case, the structured grids had a rectangular shape with a minimum orthogonal quality equal to 1. Based on the grid-independence analysis in Chapter 5, the global maximum grid size was selected to be fixed at 0.01 cm. The numbers of nodes, faces, and elements in the mesh are displayed in Table 6.1.

Table 6.1. Fluent mesh statistics.

Type	**Number**	
	4-cm configuration	**6-cm configuration**
Cells	40,000	60,000
Faces	80,800	120,700
Nodes	40,798	60,701
Cell zones	4	6
Face zones	13	19

6.4.2 Boundary and initial conditions

The boundary conditions required for the multi-bed absorptive ammonia reactor were similar to those of the adjacent coupling absorptive reactor in Chapter 5: inlet, outlet, and two walls. The inlet to the computational domain applied the setting of ‘velocity inlet’; at the outlet, ‘pressure outlet’; while the ‘wall’ boundary condition describes others. The ‘velocity inlet’ boundary condition allowed the application of a uniform velocity field of 0.01 m/s at the inlet of

the computational area, with the velocity set normal to the boundary. The stationary walls were defined with the no-slip condition and a zero-gradient condition for all species. The temperature within the reactor was uniform and set to 300 ˚C. The pressure at the initial point was set as 100 bar. The boundary and initial conditions are detailed in Table 6.2.

Table 6.2. Operating parameter values used for model simulation

Parameter	**Value**
Hydrogen inlet to the absorptive reactor	75 mol%
Nitrogen inlet to the absorptive reactor	25 mol%
Ammonia inlet to the absorptive reactor	0 mol%
Initial pressure	100 bar
Gas inlet velocity	0.01 m/s
Temperature	300 ˚C
Viscous model	Laminar
Initial temperature of the reactor column	300 ˚C
Initial $N_2/H_2/NH_3$ ratio in the reactor column	1 : 3 : 0

6.4.3 Numerical methods

The Navier-Stoke equations were solved with the SIMPLE algorithm. The models of catalyst and absorbent beds have a lot in common with Chapter 5, as they were also represented by the porous media and volumetric reactions were considered using a user defined function (UDF) code. Furthermore, the unsteady-state calculation solver and the second-order discretisation scheme were still applied in the simulation, however, with a time step size of 0.01 s in this chapter.

6.5 Simulation results and discussion

The low per-pass conversion in the conventional ammonia synthesis reactor is caused by the reversibility of the reaction. The reaction equilibrium limits its continuous progression. However, the absorption of ammonia can efficiently separate the product of reaction, which drives the reaction to the right. Based on the results of previous chapters, absorption can indeed increase the per-pass conversion. However, the improved conversion is still below the equilibrium level. Furthermore, the diffusion in the mixture takes a minor part in the species transport, which results in the adjacent coupling absorptive reactor having a limited role on the improvement of conversion. Therefore, a multi-bed absorptive reactor was proposed, and the number of beds and length of each bed become the objects of study for achieving a per-pass conversion close to 100%.

To determine the improved design of a multi-bed absorptive reactor, boundary conditions and parameters were the same for the different configurations. Results, including contour and XY plots, are presented and analysed in this section. The contours of ammonia mole fractions were compared for different configurations, as well as the XY plots of ammonia mole fraction at the central longitudinal axis of the reactors. XY plots are a more detailed and direct display of the results. The curves in the XY plots are not smooth as calculations are based on the finite control volume method and the size of the volume cannot be infinitesimal, thus there is always some fluctuation.

With operating conditions of 300 $^{\circ}$C and 100 bar, the contour plots of ammonia mole fraction for the 1-2-1-2 configuration vessel are displayed in Figure 6.2. As the reactor was laid horizontally, the gas flow entered from the left to the right of the column, as the arrow points in the direction from inlet to outlet. The reaction occurs when the hydrogen and nitrogen flow through the catalyst zone. Therefore, the nitrogen is consumed and ammonia is produced in the catalyst bed (black block), as illustrated in Figure 6.2. It is observed that, after the catalyst bed, the mole fraction of ammonia decreased to zero as ammonia is fully absorbed when passing through the absorbent bed (red block).

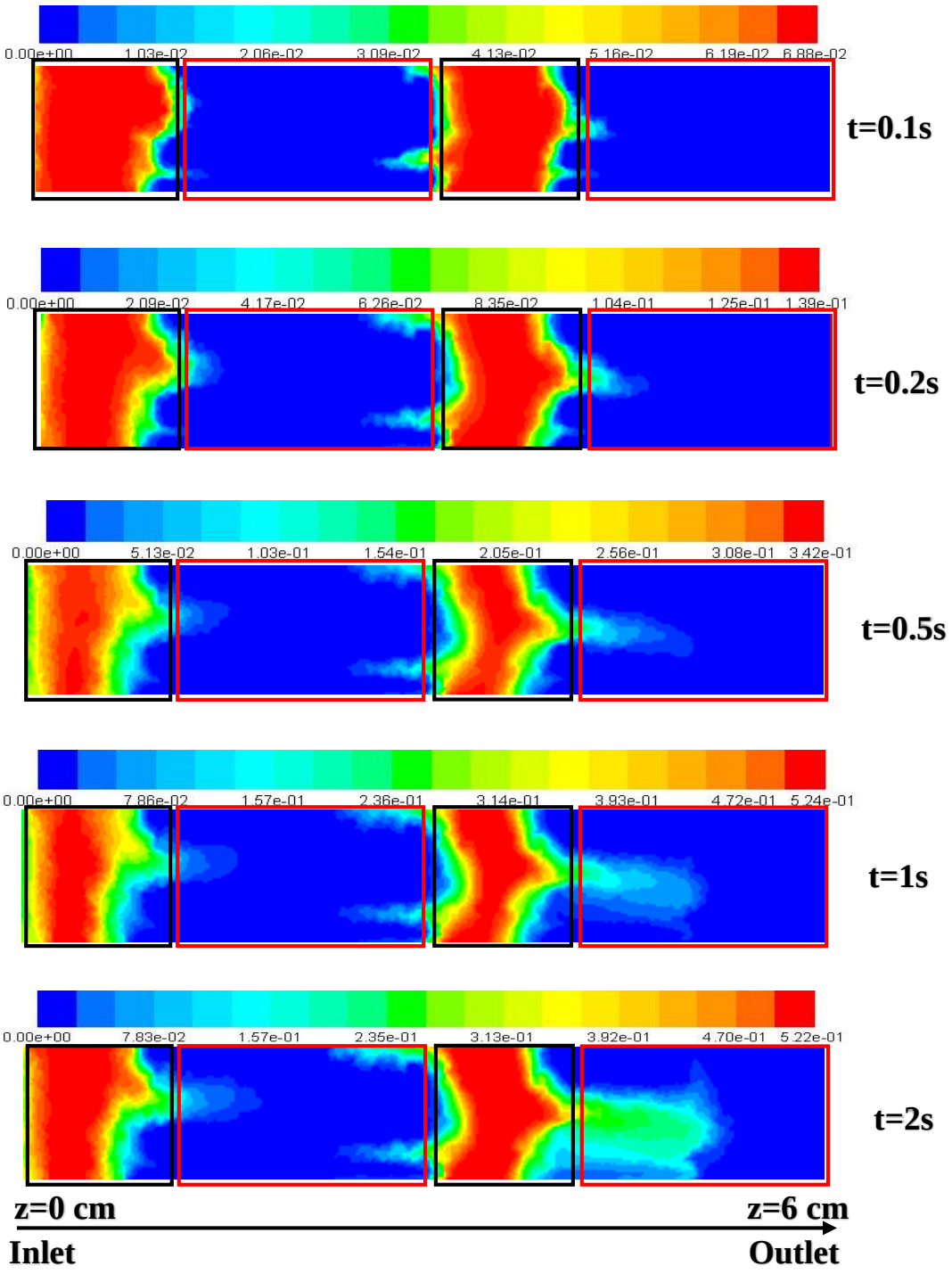

Figure 6.2. Contour plots of ammonia mole fraction (1) in the 1-2-1-2 configuration absorptive reactor at time intervals of 0.1, 0.2, 0.5, 1.0, and 2.0 seconds. The colormaps of the mole fraction ranges are different for each of the cases and are aligned at the top of each case.

To facilitate analysis, a line was located at the central longitudinal axis of the absorptive reactor. The mole fraction of ammonia on this line was analysed to investigate the reactor performance, and is plotted in Figure 6.3. Each line demonstrates that the mole fraction of ammonia had an increasing trend in the catalyst bed and a decreasing trend in the absorbent bed, which forms two peaks. The value of these peaks increase gradually as time increases and reaches a steady level, 52%, after 1 s. The mole fraction of ammonia in the outlet of the absorptive reactor was zero.

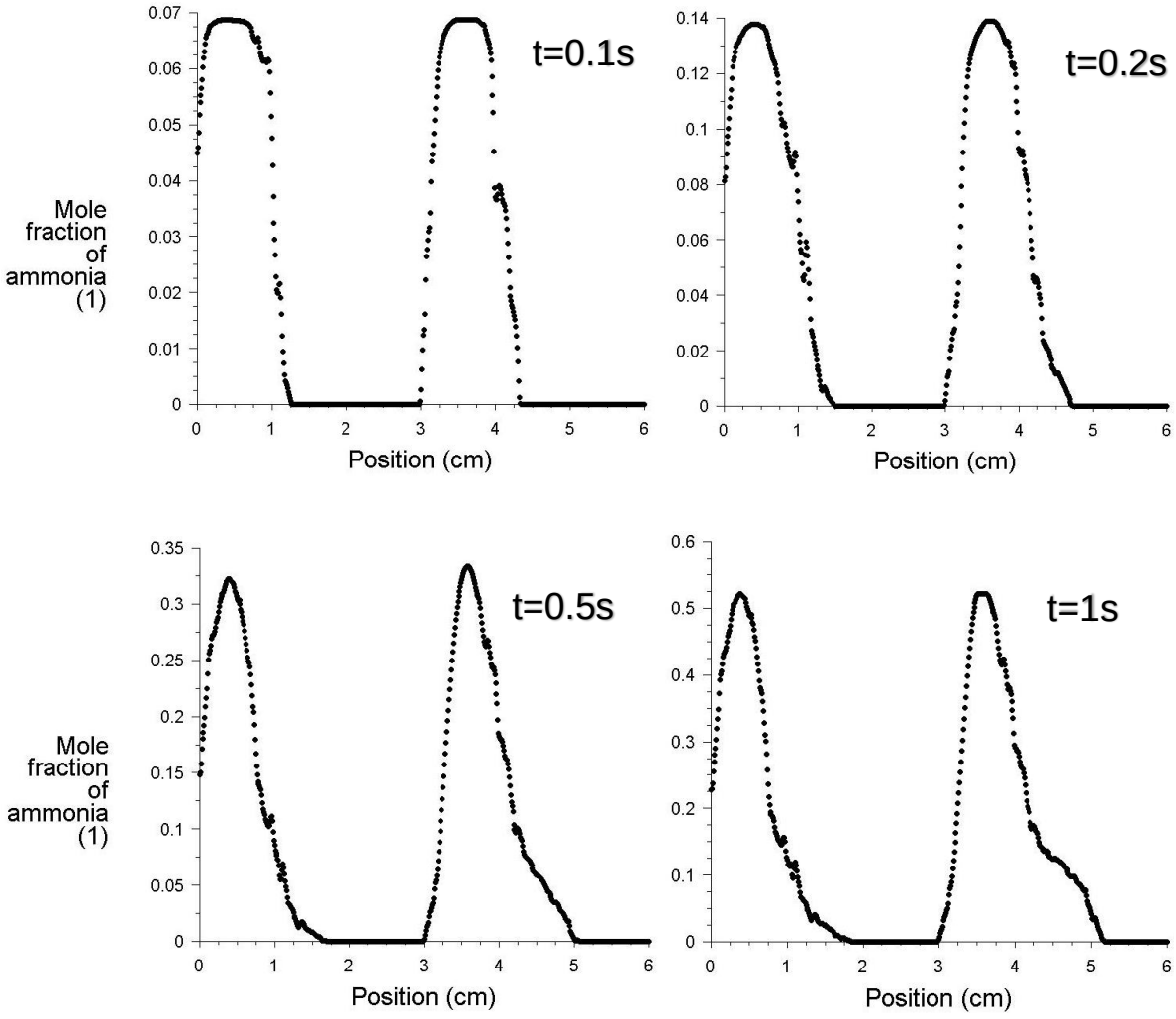

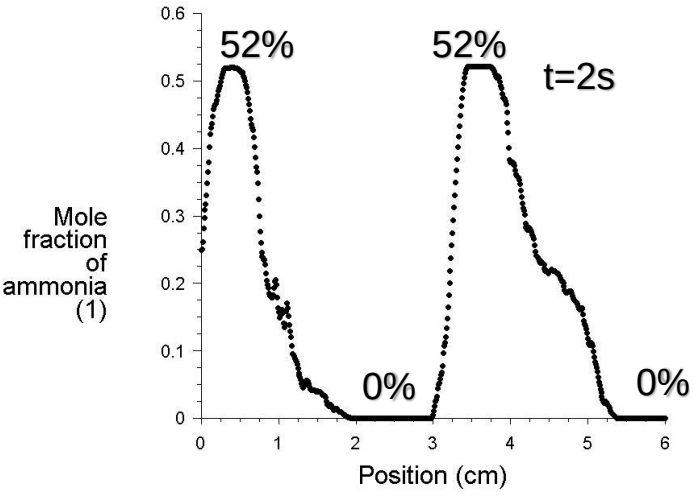

Figure 6.3. Mole fraction of ammonia for the 1-2-1-2 configuration at the central longitudinal axis of the reactor vessel at time intervals of 0.1, 0.2, 0.5, 1.0, and 2.0 seconds.

Next, the contour plots of ammonia mole fraction in the 1-1-1-1 configuration are displayed in Figure 6.4. A similar trend for the mole fraction of ammonia can be observed, as it increased in catalyst zones and declined in absorbent zones. Figure 6.5 also illustrates two peaks in each line for the 1-1-1-1 configuration, however, they are less steep than for the 1-2-1-2 configuration. Because the length of the absorbent bed is shorter than that in the 1-2-1-2 configuration, ammonia cannot be fully absorbed in this case. Take the running time at 2 s in Figure 6.5 as an example: the synthesis in the third bed (second catalyst bed) starts to form a situation where ammonia already exists in the fluid with a proportion of 26%. This directly led to a low-efficiency synthesis rate in this catalyst bed as the mole fraction of ammonia reaches only 46%. To compare the performance of these two kinds of reactors, the overall per-pass conversion is computed. In the multi-bed absorptive reactor, the overall per-pass conversion is a sum of all catalyst beds. In the 1-2-1-2 absorptive reactor configuration, the conversion is 68.4% for each catalyst bed, calculated in Appendix C. Therefore, the per-pass conversion (X) of the whole reactor is:

$$X = 0.684 + (1 - 0.684) \times 0.684 = 90\%$$

However, for the 1-1-1-1 configuration absorptive reactor, the conversion of the third bed (second catalyst bed) is only 37%, calculated in Table C.4 of Appendix C, as ammonia was not totally separated by the absorbent bed. Therefore, the per-pass conversion of the whole reactor is only:

$$X = 0.684 + (1 - 0.684) \times 0.37 = 80\%$$

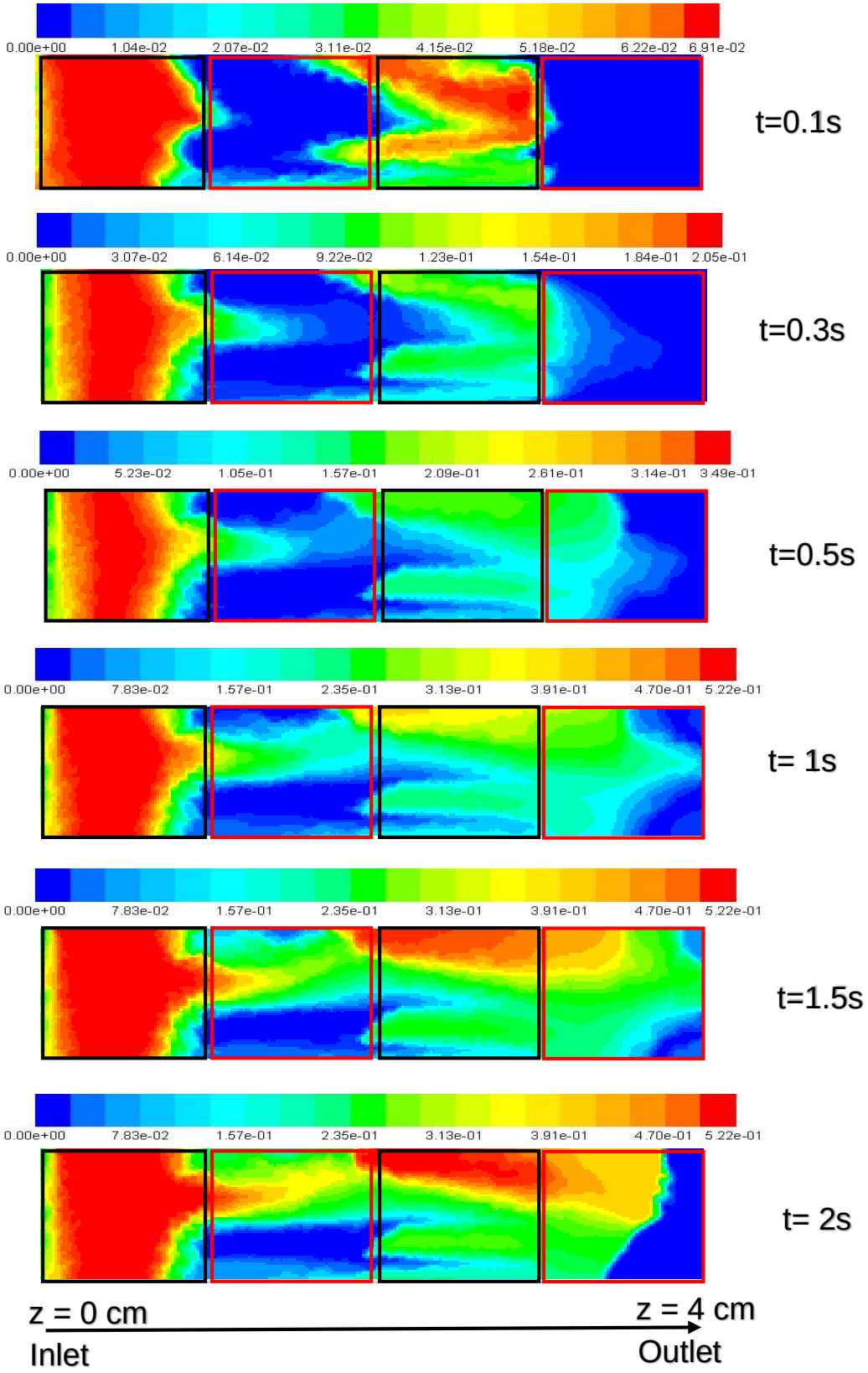

Figure 6.4. Contour plots of ammonia mole fraction (1) in the four-bed absorptive reactor (1-1-1-1) at time intervals of 0.1, 0.3, 0.5, 1.0, 1.5, and 2.0 seconds. The colormaps of the mole fraction ranges are different for each of the cases and are aligned at the top of each case.

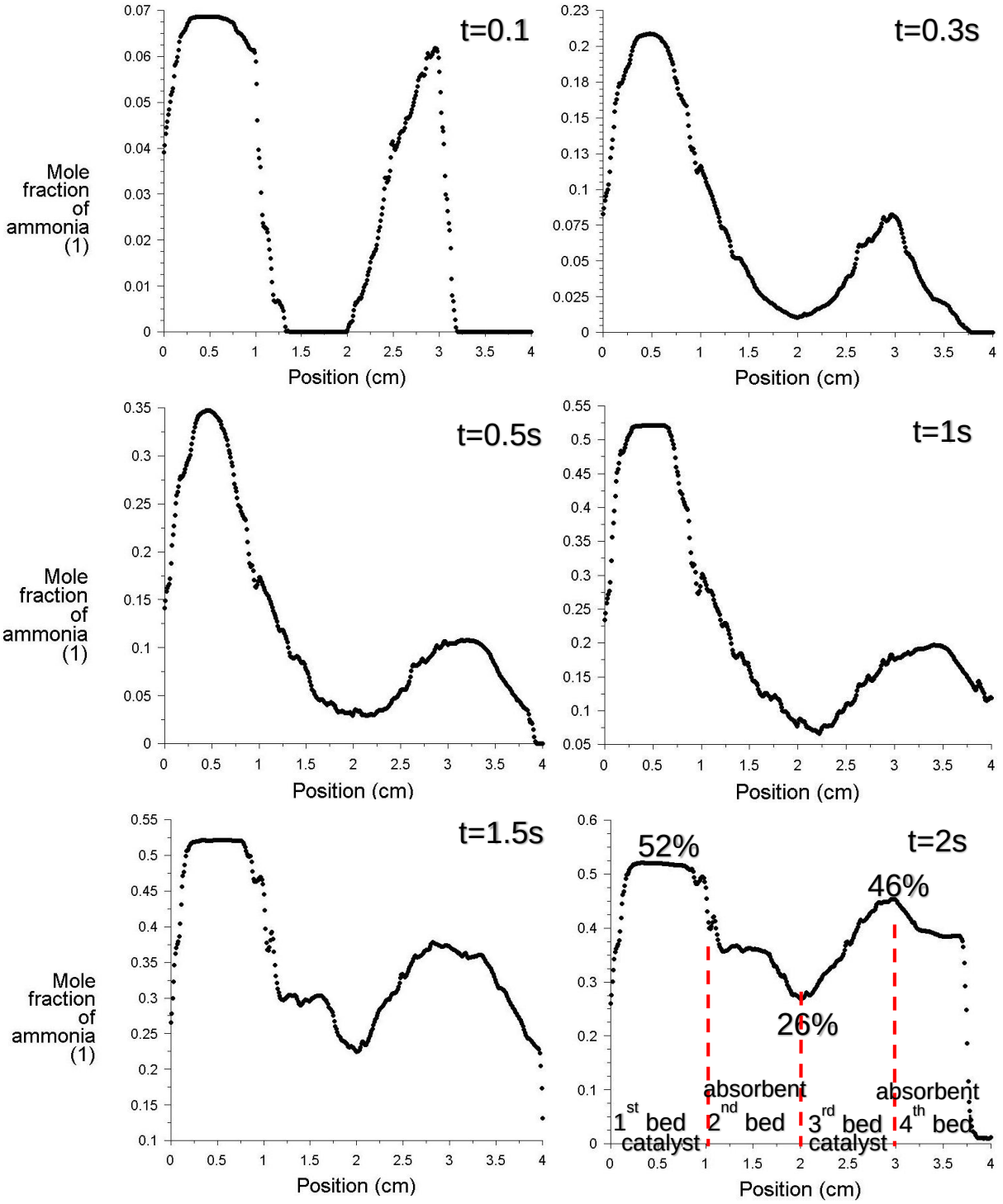

Figure 6.5. Mole fraction of ammonia for the four-bed (1-1-1-1) configuration at the central longitudinal axis of the reactor vessel at time intervals of 0.1, 0.3, 0.5, 1.0, 1.5, and 2.0 seconds.

If the number of beds increased to six (1-2-1-2-1-2 configuration), the per-pass conversion would be further improved. The schematic diagram of the six-bed absorptive reactor is

illustrated in Figure 6.6. Similarly, the catalyst bed in Figure 6.6 is referred by ‘C’ and the absorbent bed by ‘A’.

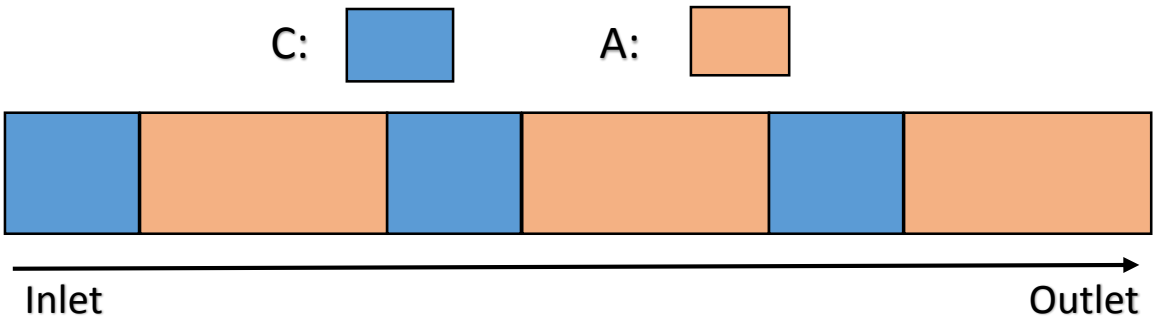

Figure 6.6. The schematic of 1-2-1-2-1-2 configuration of the six-bed absorptive reactor.

Therefore, the per-pass conversion of the six-bed absorptive reactor is:

$$X = 0.684$$

$$+(1-0.684)\times 0.684$$

$$+(1-0.684+(1-0.684)\times 0.684)\times 0.684 = 97\%$$

The per-pass conversion of the 1-2-1-2 four-bed absorptive vessel is 90%, while of the 1-1-1-1 four-bed absorptive vessel is 80%. Therefore, it can be concluded that the multi-bed absorptive reactor performs better when ammonia can be fully separated in the absorbent bed, which leads to a higher conversion with the same amount of catalyst. Meanwhile, if the number of beds increases, e.g. with six catalyst and absorbent beds (1-2-1-2-1-2 configuration), the per-pass conversion can reach 97%, close to 100%. It may prove to be uneconomical to recycle the unreacted hydrogen and nitrogen as only small amounts are left. In consequence, the multi-bed reactor can achieve the goal of improving the per-pass conversion of the Haber-Bosch reactor.

Superficial velocity can be expressed as:

$$u_s = \frac{Q}{A}$$

where u_s is the superficial velocity (m/s), Q is the volume flow rate (m^3/s), A is the cross sectional area (m^2). When the ideal gas law is applied, $pQ = nRT$, the effect of changed moles on the volume flow rate is linear. When the conversion of nitrogen reaches 97%, the total moles amount will be reduced 50% at the end of catalyst bed. Therefore, the superficial velocity at end of catalyst bed will be reduced by half. Furthermore, the superficial velocity will be even lower at end of the absorbent bed - only 3% of the initial velocity - due to ammonia absorption. In such cases, the simplifying assumption of a constant superficial velocity could lead to greater errors, therefore the results should be treated with caution.

Both ammonia synthesis and absorption are highly exothermic. Near isothermal operation may be maintained in a lab-scale unit, but it would be unlikely for an industrial scale process. In a scaled-up multi-bed system such as those to be encountered in industrial applications, the amounts of ammonia produced and absorbed, and heat released are huge. Therefore, the reaction mixture should be cooled using heat exchangers placed between the catalyst and absorbent beds, whereby the hydrogen and nitrogen could be preheated to reaction temperature, as shown in Figure 6.7. The absorptive reactor in Figure 6.7 has four alternating beds of catalyst and absorbent [165]. This design of an absorptive reactor is an attempt to meet the industrial scale temperature control requirements in the future.

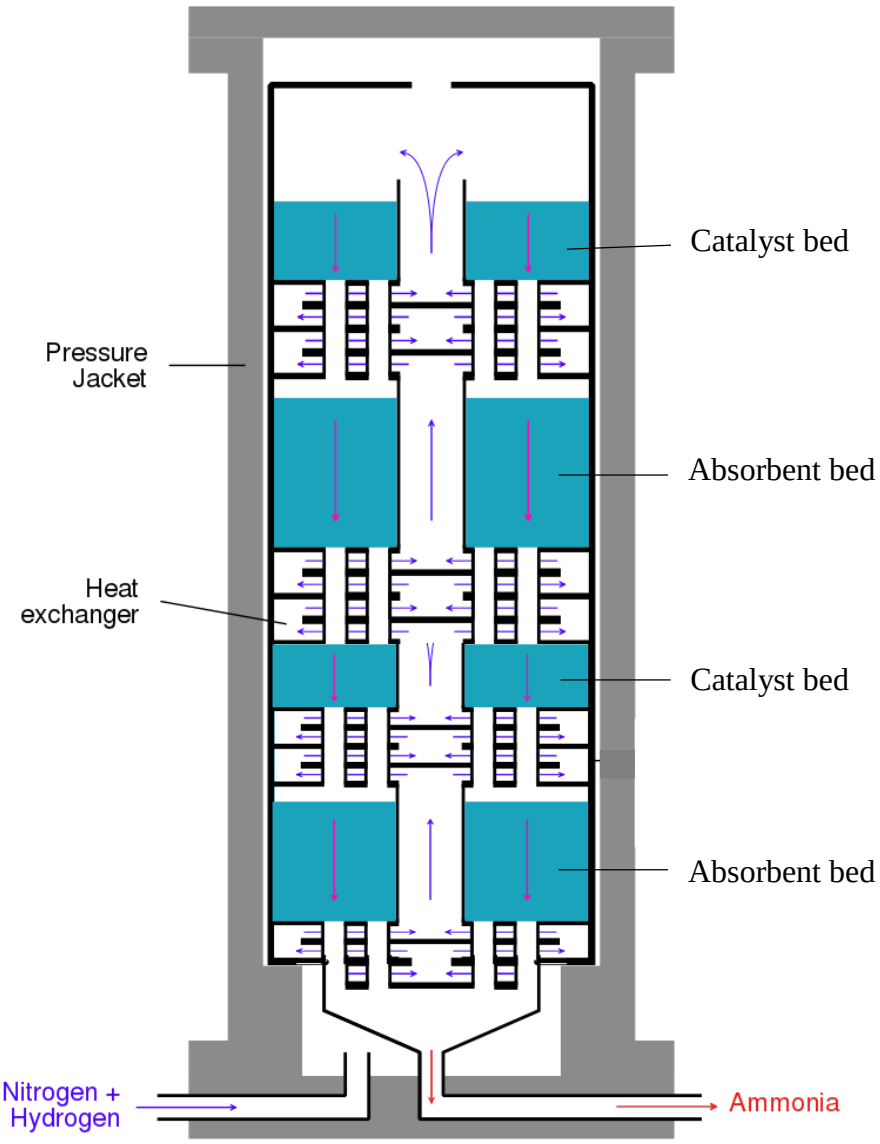

Figure 6.7. Schematic of one kind of multi-bed absorptive reactor [165].

6.6 Conclusion

This chapter presented a study of the multi-bed ammonia absorptive reactor through a computational fluid dynamics approach. The simulation has evaluated the effects of reactor configuration on the per-pass conversion of ammonia synthesis using ANSYS Fluent. The main focus was to develop and validate appropriate configurations, which could improve the multi-bed reactor performance. The results indicate that the configuration in the multi-bed absorptive reactor can indeed influence its performance and, when the ammonia can be fully absorbed, it leads to a higher per-pass reaction conversion compared with when ammonia is

only partially separated. 97% conversion can be reached when there are six beds in the absorptive reactor. The simulation time needed for ammonia synthesis to reach equilibrium in this case was about 2 s, while in Chapter 5 it was about 10 s. This difference was because that the operating conditions for ammonia reaction were different. The operation under higher pressure reaches equilibrium faster than that in lower pressure, which were physically correct.

The multi-bed absorptive reactors for ammonia synthesis proposed in this research have the following merits: (i) higher per-pass conversion can be realized under mild conditions by using an absorbent to separate ammonia, leading to a lower energy cost as unreacted reactants recycling can be reduced or even eliminated; (ii) the mild operating conditions for synthesis process can emit less CO_2 and efficiently alleviate environmental issues such as global warming.

However, the progress of simultaneous synthesis and absorption faces great obstacles, such as temperature control, especially at industry scale. Unfortunately there is no experimental data that could be used as a reference to verify and support the simulation results in this study. Further research on the multi-bed absorptive reactor has been hampered by a lack of an experimental setup and of basic data of the ammonia production rates. In addition, the high temperatures and the presence of hydrogen may lead potentially to the decomposition of $MgCl_2$. More importantly, current understanding on the fundamental mechanisms of ammonia ab/desorption is still very limited. The reaction rate of Ru catalyst under the condition of 300 ^oC and 100 bar in this simulation was calculated from empirical equation, which may be not consistent with the accurate chemical kinetics. Therefore, more research will be required to see if the multi-bed coupled absorptive reactor could be a valuable attempt to achieve a complete reaction of hydrogen and nitrogen under mild conditions within one vessel in the future.

Chapter 7. Ru catalyst with polar metallic oxide support for mild-condition ammonia synthesis

7.1 Introduction

Based on the requirements of the multi-bed absorptive reactor in Chapter 6, the catalyst needs to perform well under low operating temperatures. It was found that the best performance for ammonia synthesis is provided by Ru catalyst with an average size of 2.1 nm [92]. However, the high operating temperatures required in ammonia synthesis still need to overcome the reaction activation barrier. In this case, the high temperatures provide energy for hydrogen and nitrogen dissociation, and also to overcome the competitive adsorption that exists between hydrogen and nitrogen at the active sites. Hydrogen molecules, compared with nitrogen molecules, can easily adsorb on the surface of the catalyst. Thus, hydrogen blocks the sites for nitrogen dissociation, which triggers the hydrogen poisoning effect in the presence of the un-promoted Ru catalyst [96]. The surface poisoning of Ru sites by competitive hydrogen adsorption limits the overall rate of ammonia production. Therefore, the improved catalyst in this project attempted to minimise the effect of hydrogen poisoning on the ammonia synthesis reaction. The development of a new catalyst for ammonia synthesis under mild conditions, especially for low temperatures, is impactful. By varying the composition of the catalyst, we aim to find an improved catalyst formulation for ammonia synthesis under mild operating temperatures.

In this project, we highlight important progress in morphology-dependent nanocatalysts based on the use of metal oxides with characteristic polar surface features to improve their catalytic performance. Extensive recent studies have demonstrated that controlling the catalyst particle morphology, especially the catalyst supports, allows selective exposure of a larger fraction of the reactive facets, on which the active sites of a catalyst can be enriched. This desirable surface coordination of catalytically active atoms or domains substantially improves catalytic

activity [166]. For example, ZnO has been found to have a shaping effect on the activity of Cu nanoparticle catalysts for the selective hydrogenation of CO_2 to CH_3OH reaction [167].

For ammonia synthesis, hydrogen poisoning limits the overall rate of ammonia production. Therefore, this study focuses on the removal of the hydrogen poisoning effect through the introduction of polar surfaces of oxide supports. The goal is to improve the Ru-based nanocatalysts to reduce hydrogen poisoning through the development of effective non-carbon supports, such as MgO with polar surfaces. These support materials were synthesised and tested. Several metal oxides with polar surfaces were examined in conjunction with Ru catalysts for the ammonia synthesis reaction, such as ZnO, Co_3O_4, and MgO.

This chapter details a study of the development of an improved catalyst for ammonia synthesis under mild conditions. The experiments for catalyst development and testing were run in collaboration with Professor Tsang's group in the Department of Chemistry, University of Oxford. These catalysts were characterised by X-ray diffraction (XRD) and scanning transmission electron microscope (STEM) to gain insight into the effective factors for improving the activity of the synthesis catalyst. XRD and STEM characterisation data of these catalysts were collected from Mr Simson Wu, a member of Tsang's group. This chapter includes a detailed description of the preparation of Ru-based catalysts with different metallic oxide supports, polar and non-polar, prepared by the incipient wetness impregnation method, which is a commonly used technique for the synthesis of heterogeneous catalysts. The catalytic testing facility used to probe the ammonia synthesis reaction is described in this chapter. The principles and analyses of the characterisation techniques performed on these prepared catalysts are also addressed.

7.2 Catalyst preparation

Various methods have been used for the preparation of ruthenium nanocatalysts, including impregnation, precipitation, and in situ reductions [168]. In this project, the incipient wetness impregnation method was used. The average size of the metal particles depends on the

concentration of the solution used, such that high metal loadings tend to give larger particles than low loadings, and the variation in the volumes of individual pores leads to a rather broad size distribution. If the drying step is performed slowly, the salt migrates towards the external surface of the support particle; if a uniform distribution of metal throughout the support is desired, it is better to dry quickly. The final important step in the preparation of a supported metal catalyst is the reduction of the precursor to the metallic state. This calcination is to convert the precursor to the oxide, which is usually the most accessible compound to reduce [72]. In this research, the $Ru_3(CO)_{12}$ precursor was used for the ammonia synthesis catalysts. It is one of the most stable and commercially available and is better than $RuCl_3$, because it is highly dispersed and is free of chlorine, which is poisonous for ammonia synthesis [83]. The precursor was dissolved in Tetrahydrofuran (THF), an organic solvent. Then, the metal-containing solution was added to the catalyst support. The catalyst was then dried and calcined to drive off the volatile components within the solution. Finally, the metal was deposited on the catalyst surface.

7.2.1 Metallic oxide with polar surfaces preparation

7.2.1.1 ZnO synthesis

Zinc acetate dehydrate (6.0 g $Zn[Ac]_2{\cdot}2H_2O$) and 3.84 g hexamethylenetetramine (HMT, $C_6H_{12}N_4$) were dissolved in 48 mL deionised water. After 10 min of stirring, the solution was transferred into a 100 mL Teflon-lined autoclave and maintained at 99 °C for 24 h. It was then naturally cooled to room temperature. The white precipitate was collected by centrifugation at 5,000 rpm for 10 min, after which the supernatant was decanted and discarded. The solid was washed repeatedly with ethanol and water to remove excess precursor. All the ZnO nanoplate was dried in an oven (100 °C) for 12 h and then calcined at 450 °C for 2 h to remove surfactant with a heating rate of 10 °C/min in an air atmosphere [169].

7.2.1.2 Co_3O_4 synthesis

Cobalt acetate tetrahydrate (2.49 g) was dissolved in 30 ml of ethylene glycol, and the mixture was gradually heated to 160 °C. Aqueous 0.2 M Na_2CO_3 solution (100 ml) was then added, and the slurry was further aged for 1 h under vigorous stirring and a continuous flow of nitrogen. After filtration and being washed with water, the obtained solid was dried at 50 °C overnight under a vacuum and calcined at 450 °C for 4 h in air [170].

7.2.1.3 MgO synthesis

$MgCl_2.6H_2O$ (2 g) and benzoic acid (0.12 g) were dissolved in 60 ml deionised water. The mixture was stirred for 1 h. 2M NaOH (20 ml) was then added dropwise into the solution, forming a white precipitate. The slurry was subsequently transferred to a 100 ml autoclave and gradually heated to 180 ˚C and maintained at this temperature for 24 h. The $Mg(OH)_2$ precursor was obtained after filtration followed by washing with water and drying at 80 ˚C under vacuum overnight. MgO(111) nanosheets were obtained after calcination in compressed air at 500 ˚C for 6 h [171].

7.2.2 Incipient wetness impregnation method

The synthesis of Cs-Ru/metal oxides followed the incipient wetness impregnation procedure. Metal oxides (ZnO, Co_3O_4, MgO), polar (made through procedure in Section 7.2.1) and non-polar (commercial products), the powder was evacuated overnight at 70 °C inside a vacuum oven. Afterwards, the active metal precursor, $Ru_3(CO)_{12}$, was sonicated and dispersed in THF and loaded onto the metal oxide powder via the incipient wetness impregnation method. The mixture was left to stir for 4 h, where the solvent was removed by rotary evaporation. The Ru-loaded catalyst was then calcined under flowing Ar at 350 °C for 6 h. The addition of the promoter Cs again followed the impregnation method. $CsNO_3$ was dissolved in distilled water and then impregnated to the calcined Ru/metal oxide powder. Before the catalytic testing, the Cs-Ru/metal oxide powder underwent reduction at 350 °C for 4 h under 5% H_2 in Ar.

7.3 Catalyst testing

A 100 mg sample was placed in the middle of an 8 mm diameter reaction tube sandwiched between two silica wool plugs. Mass-flow controllers were turned on, and the pressure was increased. There was a thermocouple fitted inside the reactor tube. The ammonia produced was trapped by dilute H_2SO_4 and analysed by titration. The other experimental setups employed are the same as that in Chapter 3, except that the absorbent was not added in this chapter. The H_2 flow rate was set to 50 mL min^{-1}, heated to 450 ˚C and held for two hours, then ramped to 400 ˚C, the desired reaction temperature. The backpressure regulator was increased to 10 bar, the desired pressure.

An ion-selective electrode was used for the measurement of dissolved ammonium, which was produced during the reaction and trapped in a mildly acidic solution. The Ion Concentration Measurement was calibrated with 10 to 1,000 ppm calibration solution before measuring the concentration of ammonia.

7.4 Catalyst characterisation

The physical characterisation of supported metal catalysts is a challenging problem, to the solution of which a great many analytical methods have been applied. Many different techniques have been used to probe the properties of heterogeneous catalysts, such as X-ray powder diffraction (XRD), scanning electron microscopy (SEM), transmission electron microscopy (TEM), X-ray photoelectron spectroscopy (XPS) and temperature-programmed reduction (TPR). All of these techniques provide valuable pieces of information, fitting together to build an accurate description of the system. This project focuses on the XRD and STEM techniques.

7.4.1 X-ray diffraction (XRD)

X-ray diffraction (XRD) is routinely used in heterogeneous catalysis, as XRD patterns reveal the identity and crystallite size [172]. Moreover, because XRD patterns yield d-spacing and unit cell information, insight into the atomic constituents of the species can be obtained.

The Scherrer equation can be used to estimate the average crystal size of Ru and the support [173]:

$$B_c = K_1 \lambda_w / d_{cry} \cos\theta$$

where B_c is the line broadening, K_1 is a constant (0.893), λ_w is the wavelength, d_{cry} is the crystallite size, and θ is the Bragg angle. In 1912, W. L. Bragg treated the diffraction of X-rays by crystals, as depicted in Figure 7.1. X-ray diffraction lines shown by particles less than approximately 50 nanometres in size are broadened, and the degree of broadening can be employed to give the average particle size.

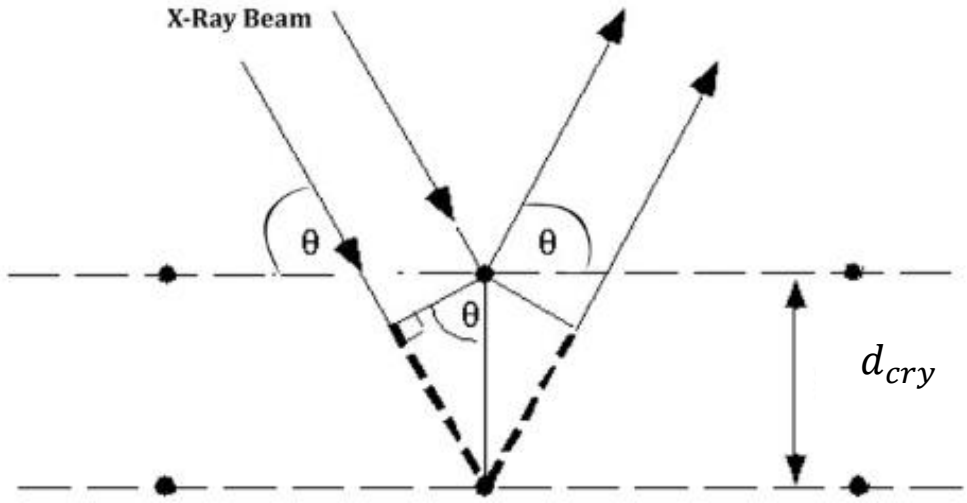

Figure 7.1. Diffraction of X-rays by a crystal [174].

7.4.2 Scanning transmission electron microscope (STEM)

Microscopy is the most direct method to characterise the size and shape of nanostructures. Electron microscopy is a primary analytical tool for the direct observation, manipulation, and

understanding of the building blocks of material. It reveals the surface topology of the heterogeneous catalyst and plays an important role in determining the size of the metal particles to study any size effects on the catalytic reaction. Scanning transmission electron microscopy (STEM) has been used for the study of Ru nanocatalysts in this chapter.

Scanning transmission electron microscopy is mainly used to provide a topographic image of the surface of the sample. A resolution of down to 10 nm is available with most machines. In the present project, the STEM was used in conjunction with XRD for the analysis of the catalyst surfaces. The principle of STEM is a combination of scanning electron microscopy and transmission electron microscopy. This technique uses the information carried by the beam of electrons across the sample in a raster pattern. Interactions between the beam electrons and sample atoms produce a serial signal stream, linked with beam location, to build an image, in which the signal level at any position in the sample is characterised by the grey level at the consistent position in the image [175].

7.5 Results and discussion

Table 7.1 displays the comparative catalytic performance, the ammonia production rate over Ru-based catalysts using different metallic oxide supports with or without polar surface. The table reveals that the activity of catalysts based on magnesium oxide was much higher than catalysts based on zinc oxide or cobaltosic oxide, regardless of the morphologies of the oxides. Furthermore, the use of MgO(111) support with a polar surface yielded the best activity under the same reaction conditions (673 K and 10 bar at N_2/H_2 of 3:1). Ru is one expensive metal. Therefore, controlling the Ru content in the catalyst at a low level while with high synthesis activity will be important. In contrast, the Ru catalysts based on zinc oxide and cobaltosic oxide support demonstrated quite low activities, which is further discussed in this section.

Table 7.1. Comparison of ammonia production rate between Cs-Ru/MgO, Cs-Ru/ZnO, and Cs-Ru/Co_3O_4 at N_2/H_2 = 1/3 under 673 K and 10 bar conditions.

Catalyst	Rate ($\mu mol_{Metal\_\mu mol}^{-1}$ h^{-1})
Cs-Ru/MgO(111)	66.1
Cs-Ru/MgO(commercial)	20.6
Cs-Ru/ZnO	0.002
Cs-Ru/ZnO(commercial)	0.001
Cs-Ru/Co_3O_4	0.03
Cs-Ru/ Co_3O_4(commercial)	0.02

Figure 7.2 presents the XRD results of the metallic oxides with polar surfaces and Ru/Cs loaded catalysts. The data in Figure 7.3 were collected from the literature [169][176][177]. The diffraction angles of metallic oxides in Figure 7.2 are consistent with the angles in Figure 7.3. Therefore, the XRD analysis confirmed that all catalyst supports contained polar surfaces. As for magnesium oxide- and zinc oxide-supported catalysts, the metal oxide revealed diffraction peaks, which match well with the zinc oxide (2Θ from 30° to 60°) and magnesium oxide (2Θ of 44° and 63°) phases. This indicates the existence of polar surfaces on the zinc oxide and magnesium oxide phases in the catalyst sample after the hydrogen pre-treatment and activity testing. However, the polar surface of cobaltosic oxide seems to have been damaged during its loading of Ru and Cs. After the loading of Ru and Cs by the incipient wetness impregnation method, the intensities of the peaks of cobaltosic oxide from the samples were significantly attenuated, and some disappeared. Therefore, the low activity of Cs-Ru/Co_3O_4 was caused by the damage of the oxide support, which led to a low concentration of active phase.

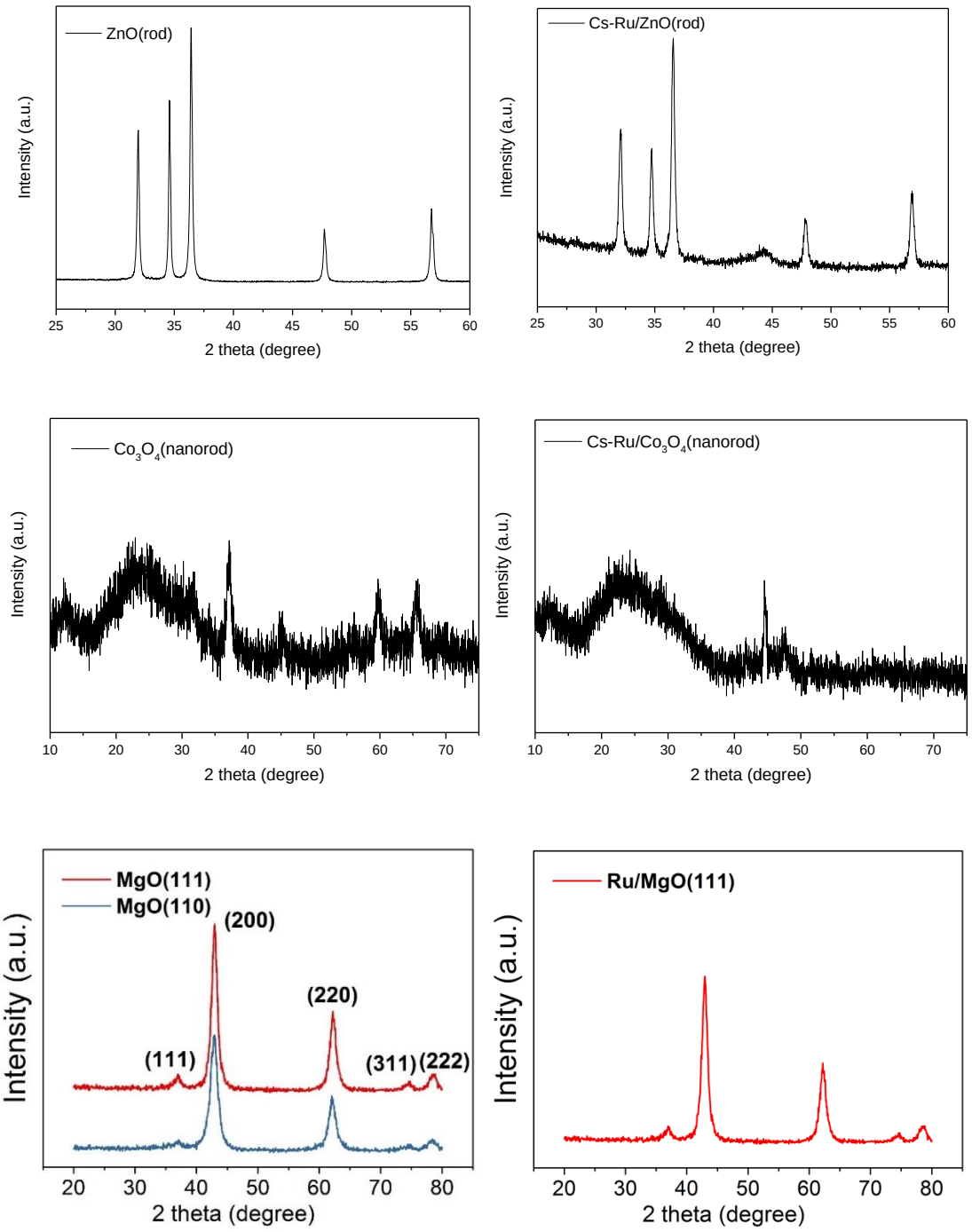

Figure 7.2. XRD results of metallic oxides, ZnO, Co_3O_4, and MgO, and catalysts after loading Ru/Cs by the incipient wetness impregnation method.

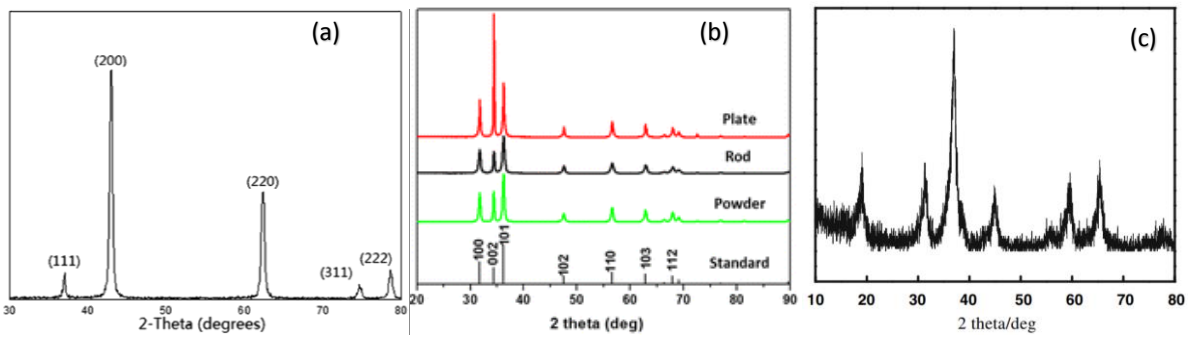

Figure 7.3. XRD pattern of the prepared (a) MgO [176], (b) ZnO [169], and (c) Co_3O_4 [177].

However, the activity of the ruthenium catalyst based on zinc oxide support was still much lower than that based on a magnesium oxide support. The atomic configuration in Figure 7.4 can explain this result. The O^{2-} sites led to the improvement of the catalyst activity, which could remove the H from ruthenium metal to the support surface and therefore inhibit hydrogen poisoning. However, the O^{2-} sites in zinc oxide were not as evenly exposed as in magnesium oxide, as the atomic radius of zinc is much bigger than that of magnesium. Therefore, the O^{2-} sites in a magnesium oxide support perform better than those in a zinc oxide support.

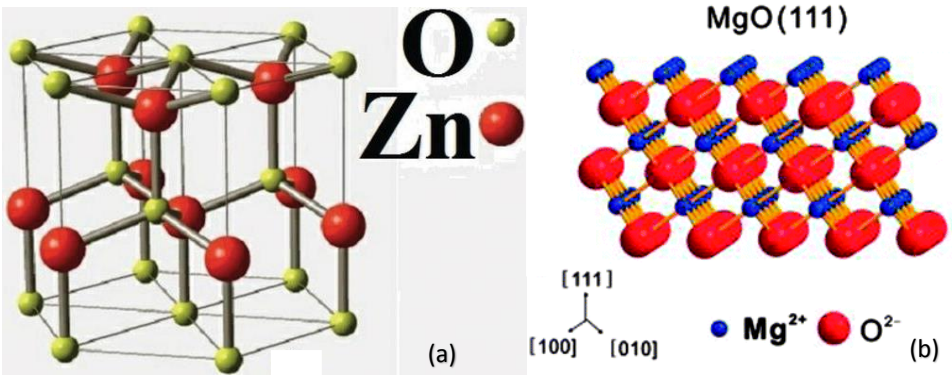

Figure 7.4. Atomic configurations of (a) ZnO [178] and (b) (111) facets for MgO [166].

Therefore, this project ultimately focused on the Cs-Ru/MgO(111) catalyst. Figure 7.5 displays the STEM image of the profile of the Cs-Ru/MgO(111) catalyst, provided by Mr Simson Wu. The white points are the O atoms from the MgO(111) support. The brighter white points in red circles are the Ru nanoparticles, as the lightness depends on the outermost electrons. There are more outermost electrons in Ru than in O atoms. The average particle size of Ru

in the catalyst sample was about two nanometres, with a low concentration on the support, as shown in Figure 7.5. This STEM figure matches the atomic configuration of the (111) facets for magnesium oxide in Figure 7.4(b).

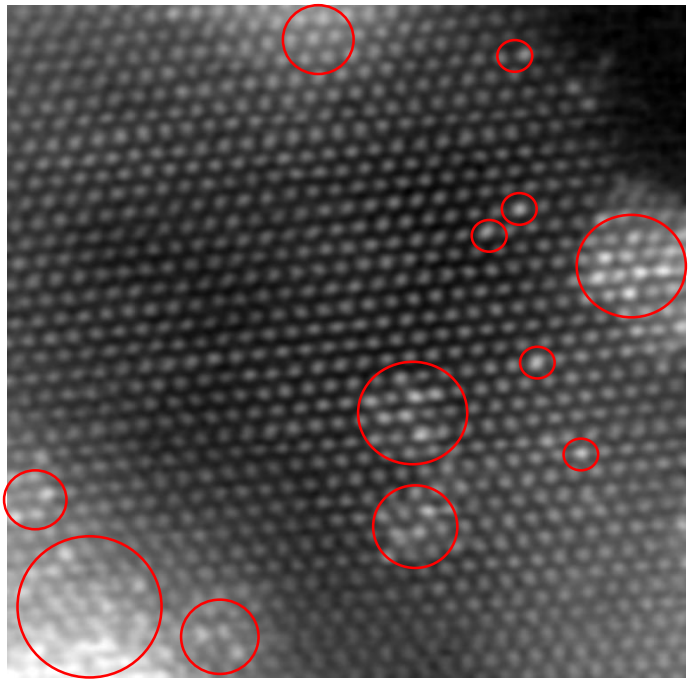

Figure 7.5. Scanning transmission electron microscopy (STEM) image of the catalyst Cs-Ru/MgO(111).

It displays a typical electron micrograph of the ruthenium nanoparticle catalyst with magnesium oxide support, as well as demonstrates the Ru nanoparticles being spread over the MgO(111) support. This sample was mainly composed of (111) planes, which was expected, as the (111) plane is considered to be the most stable phase of magnesium oxide. This also correlates with the sharp 111 peaks in the XRD pattern. The use of magnesium oxide with preferential exposed (111) surface could remove H_2 poisoning on a Ru nanoparticle by facilitating the adsorbed H species to migrate from the Ru surface to the O^{2-} sites [179]. The schematic of how the hydrogen moves is shown in Figure 7.6. This explains the observed enhancement of activity when polar MgO(111) was used as the support.

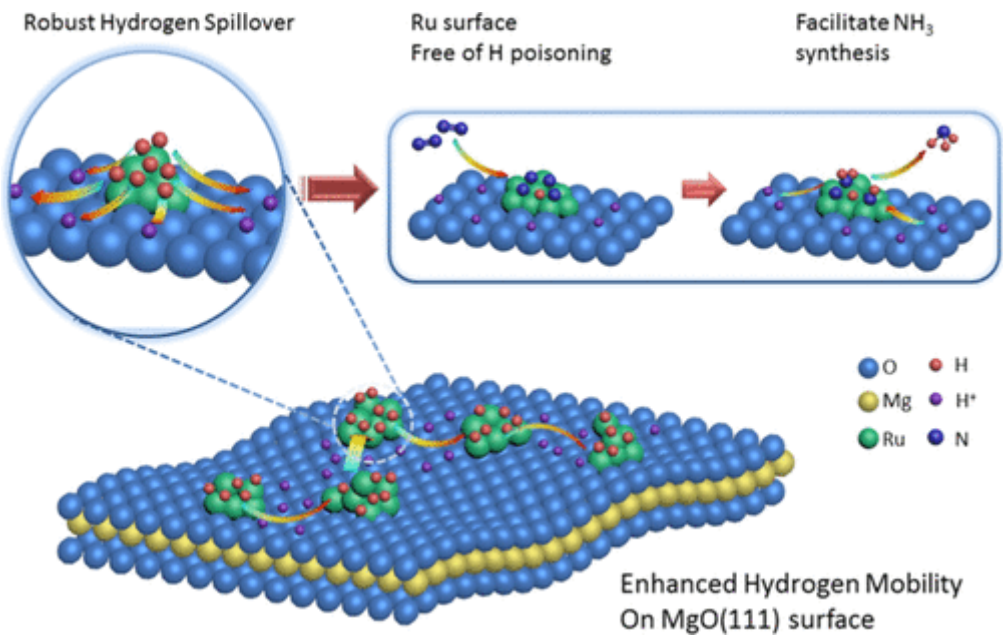

Figure 7.6. Schematic of the enhanced hydrogen mobility on the polar MgO(111) surface [179].

7.6 Conclusion

Since effective catalysts operating under mild conditions are required for the multi-bed coupled absorptive reactor, this chapter gave a direction for the development of ammonia synthesis catalysts. The high temperature required to break the energy barrier for the reaction can be reduced through the use of efficient catalysts. In this research, both the XRD patterns and the STEM images of the products are consistent, confirming that the Ru nanoparticles were synthesised by the incipient wetness impregnation method, and a magnesium oxide support with stable polar surfaces was successfully achieved. Our case employed a polar MgO(111) surface as support for Ru with an observable polarity to alleviate hydrogen poisoning. As the H atom exhibits stronger adsorption than N_2, the removal of the H atom from the active site is essential for the continuous production of ammonia. As a consequence, hydrogen does not block preferentially the sites for nitrogen dissociation. Both H_2 and N_2 molecules can easily adsorb, and less of a competitive adsorption exists between H_2 and N_2 at the active sites. Therefore, the energy needed for continuous ammonia production can be reduced and thus the operating temperature of ammonia synthesis can be reduced. A suitable catalysts for the

multi-bed absorptive reactor could be formulated. It has been observed that the Cs-Ru/MgO(111) catalyst performed best after comparing various prepared catalysts. The catalyst using of MgO(111) support with a polar surface can be regarded as a more effective catalyst for ammonia synthesis than those with non-polar surfaces. In this chapter, the contribution includes a comparison of the different types of polar surface support of Ru catalyst and a reasonable explanation of the different performances of these catalysts. We did see the significant contribution to alleviate the hydrogen poisoning phenomenon for ammonia synthesis when Cs-doped Ru was placed on MgO(111) support. Cs−Ru/MgO has been evaluated as a novel catalyst because of its active Ru on a polar surface support.

Chapter 8. Conclusions and suggestions for future work

8.1 Conclusions of DPhil work

The development of an efficient process for ammonia synthesis has been a long-sought-after goal; therefore, the application of an absorptive reactor for ammonia synthesis may be a game changer, since it allows the reaction to occur under milder conditions and improves the per-pass conversion of ammonia. The experiments in this study measured the improvement in ammonia conversion when absorbent is present in the reactor vessel. Catalyst and absorbent materials can be integrated with different configurations for ammonia synthesis. Various catalyst-absorbent systems have been mentioned in this thesis. In particular, two configurations of the absorptive reactor, adjacent coupling and multi-bed coupled were simulated, and the reason for the improvement in ammonia per-pass conversion was analysed in this study. The multi-bed catalyst-absorbent configuration was simulated and resulted in the highest production of ammonia.

To achieve a high conversion to ammonia with the absorptive reactor it was essential to evaluate the performance of the catalysts. Therefore, this study began, in Chapter 3, with the demonstration of an absorption-enhanced ammonia synthesis process by using industrial catalytic materials. A Ru-based catalyst prepared in our laboratory was then tested and used in Chapter 4. Furthermore, the Ru nanoparticles catalyst were synthesised, in which a magnesium oxide support with stable polar surfaces was successfully developed. As indicated by the experimental results in Chapter 7, the employment of a polar MgO(111) surface as support for Ru works as a more effective catalyst support for ammonia synthesis than traditional nonpolar surfaces.

The adjacent coupling absorptive reactor was simulated with the recycle stream model in Chapter 3 and with the transient backflow cell model in Chapter 4. Chapter 3 constructed a

mathematical model for the performance of an adjacent coupling absorptive reactor under Haber Bosch conditions. The ammonia absorptive reactor was simplified by three main sections operating in simulation: reaction, absorption, and recycle. This simplifed model predicted the performance of the adjacent coupling absorptive reactor and also gave information regarding each section. A hypothetical recycled fluid was proposed to represent the backflow to reproduce the effect on the per-pass conversion results. The catalyst used was stranded industrial iron catalyst, and the kinetics were modelled using a modified Temkin expression. The absorbent separated ammonia from the production mixture, and was simulated through an axial dispersed plug flow model. These three model sections were then combined to constitute the model of an adjacent coupling absorptive reactor for ammonia synthesis. The recycle stream model was focused on the effect of distance between catalyst bed and absorbent bed on the per-pass conversion. The results indicate that distance betweent the catalyst and absorbent beds could lead to a different backflow degree. The closer the absorbent is to the catalyst, the more of an improvement there is on per-pass conversion. The transient backflow cell model hypothesised a backflow between each cell to characterise the backflow in the reactor. The effect of absorption on the per-pass synthesis conversion is further researched via the backflow cell model. In chapter 4, an advanced mathematical model, the transient backflow cell model of the adjacent coupling absorptive reactor was presented. In this model, the catalyst and absorbent beds were not regarded as two separate blocks, but as a single unit. A transient cell model was taken as a reference to identify what role the absorbent plays in the enhancement of synthesis conversion. In this chapter, the optimal length of the absorbent bed is studied to have the best improvement of per-pass conversion. According to the results of these two models, when the absorbent particles are positioned after the catalyst fixed-bed, the enhanced conversion of ammonia synthesis mainly results from the wider residence time distribution and faster reaction rate caused by lower ammonia concentration. Widening the residence time distribution of the reaction leads to a higher conversion when the thermodynamic equilibrium has not been reached.

Furthermore, the effect of the absorbent leads to a lower partial pressure of ammonia (and thus a kinetic acceleration of the reaction). If ammonia synthesis can reach the thermodynamic equilibrium, the addition of an absorbent can drive the equilibrium to the right. A computational fluid dynamics simulation using dispersion model was then developed and described the adjacent coupling absorptive reactor in Chapter 5. The results obtained in Chapter 5 demonstrate that the absorption capacity of the absorptive reactor plays a more crucial role in the increment of per-pass conversion than the wider residence time distribution.

The backflow cell model was used to simulate a tubular adiabatic reactor [146]. It has been shown that the backflow cell model was used for approximation of the dispersion model. While there are differences in qualitative behaviour of simple cell and dispersion models, the backflow cell model gives results which are in agreement with the dispersion model [146].

Under real conditions, the axial mixing cannot be restricted to a single cell, and it was considered worthwhile to make a study of the backflow cell model. The backflow cell model is more flexible and makes it possible to implement all characteristics of the packed bed heat and mass transfer.

In Chapter 6, a reactor with a multi-bed pattern arrangement of catalyst and absorbent was simulated through a two-dimensional mathematical model. The reactor configuration was considered as essential factors, which affect the efficiency of the absorptive reactor. Therefore, the number of beds, and length of each bed on the performance of the reaction were studied. The obtained results demonstrated that when ammonia is fully absorbed leads to a higher reaction conversion, and 97% conversion can be reached when there are six beds in the absorptive reactor.

Based on our simulation results, it is expected that using an absorptive reactor, especially in a multi-bed configuration, could achieve in the future almost 100% per-pass conversion in the ammonia synthesis. There is a limitation of the adjacent coupling absorptive reactor in that the different temperature setting for catalyst and absorbent beds leads to a temperature gradient at their junction because of a finite thermal conduction. Compared with this limitation, the multi-

bed configuration has the advantage of temperature control as a uniform operating temperature is required. However, both configurations perform effectively only when the appropriate catalyst and absorbent material are used, which means that the catalyst can work under mild operating conditions, while the absorbent also performs well under these conditions. We believe that the proposed ammonia reactor model can also be applied to provide technical and systematic guidance for future work and contribute to solving the high energy consumption and low per-pass conversion problems in industrial ammonia production.

The research contributions of this thesis are:

A. The concept of backflow is proposed to explain the effect of adjacent coupling absorption on ammonia per-pass conversion. The backflow process was first hypothesised to explain the observation of an improved ammonia per-pass conversion in the presence of absorbent material, which was adjacent to the catalyst. The backflow was approximated with two different models: the recycle stream model and the transient backflow cell model.
B. The development and implementation of models of ammonia absorptive reactors, focusing on adjacent coupling and multi-bed coupled configurations. Several studies have recently investigated the use of absorbents as a useful technique to separate ammonia, co-locating with the catalysts or not [7][47][180][181]. However, few studies have focused on the mathematical modelling of the absorption-enhanced ammonia synthesis process [48], particularly on the adjacent coupling and multi-bed coupled absorptive reactors. This project focused on MATLAB implementations of the recycle stream model and transient backflow cell model, which were validated with experimental results obtained in collaboration with Prof. Tsang's group in the Department of Chemistry. These simulations supported experimental results, offering the possibility of further improving the absorptive reactor. A computational fluid dynamics model was also set up to model the adjacent coupling and multi-bed coupled absorptive reactors. The two-dimensional dynamic and thermal behaviour of the absorptive reactor was observed and analysed.

C. Development of improved catalytic materials for ammonia synthesis under mild operating conditions. Given that the Haber-Bosch process is energy-intensive, the development of improved catalysts for synthesising ammonia under low temperature and/or low pressure is necessary. This is also suitable for the multi-bed coupled absorptive reactor, as a low temperature for the catalyst is needed to match the operating temperature for absorbents. A number of experiments for the development of catalysts were run in collaboration with the Department of Chemistry. Improved catalytic materials were achieved and tested, and a better composition of the catalyst was determined in this DPhil work.

8.2 Limitations and suggestions for future work

The simulation of the backflow suggested that the effect could be very similar to gas recycling. However, at this stage, our experimental equipment was inadequate to study gas recycling as a verification check. This should be part of a future plan to perform, and verify the simulation data from the experiment. Furthermore, the kinetic expression for the Ru catalyst used as well as the ammonia absorption kinetics should be specifically developed in the future.

It was also acknowledged that the scarcity of experimental data points was due to the difficulty of controlling the temperature of the catalyst and absorbent beds independently. A temperature variation through the reactor exists, which affects the kinetics of both reaction and absorption. Therefore, highly precise and robust temperature control is of utmost importance. The most common form for temperature control of a reactor is a heat-transfer jacket, i.e. where the inner reactor vessel is surrounded by a jacket. The temperature control system would be connected to the reactor jacket and would continuously control the temperature of the jacket and thus the temperature of the reactor. However, a temperature gradient cannot be completely eliminated caused by the limits of thermal conduction. In the future, the influence of heat transfer limitations may be sufficiently minimized with a micro-channel reactor, in which the

temperature variation between the catalyst and absorbent beds could be minimised. Alternatively, a precise temperature measurement device in the fixed-bed absorptive reactor could be installed to obtain the temperature profiles of the absorptive reactor and thus determine the mathematical model parameters more accurately.

Isothermal operation may be able to be maintained for a lab-scale unit, but most likely not for an industrial scale process as ammonia synthesis and absorption are highly exothermic. In a scaled-up multi-bed system as those encountered in industrial applications, the amounts of ammonia produced and heat released are huge. Heat exchangers are required for the cooling of the reaction mixture.

The ammonia absorptive process is a promising technology for high per-pass conversion of ammonia production under mild conditions. However, the regeneration of the saturated absorbent is not covered in this thesis. As the desorption of ammonia from metal ammine complexes can be promoted by increasing the temperature [149], the absorbent bed should be equipped with a thermowell or inner heating wire. Metal ammine complexes decompose into metal chlorides and ammonia by heating at relatively high temperatures and by venting the system to an atmospheric pressure vessel. The desorption behaviour and mechanism of metal chlorides were investigated using temperature-programmed desorption measurements in [182]. Ammonia desorption is best conducted above 650 K [182], where a sufficiently high rate can be achieved and simultaneously a sufficiently low equilibrium ammonia concentration is reached. Considering that the absorbent regeneration occurs in an absorptive reactor, the operating conditions may be more restrictive. For example, the temperature cannot become so high that it may harm the catalyst activity. Furthermore, the required time for full desorption is also important in the operation of a continuous absorptive system for ammonia synthesis. As future work, more experiments and simulation on the desorption process of the absorptive reactor are necessary.

The saturated absorbent in the industrial multi-bed absorptive reactor can be regenerated through high temperature and low pressure. During regeneration, the operating condition maintains a high temperature (400 ˚C), leading to a reduction in the ammonia storage capacity

of the absorbent with ammonia released to the gas phase. In a scaled-up multi-bed system such as those to be encountered in industrial applications, the amounts of ammonia produced and absorbed, and heat released are huge. Some processes are employed to recover such energy as part of an integration process system as well as for heating in local and commercial operations via hot water network. For example, the reaction mixture should be cooled using heat exchangers placed between the catalyst and absorbent beds, whereby the hydrogen and nitrogen could be preheated to reaction temperature. The optimal operating conditions (such as reaction temperature, catalyst-to-gases ratio and weight hourly space velocity) are the factors affecting the overall energy consumption of the industrial design and need to be investigated in the future. Meanwhile, the catalyst/absorbent pellet diameter, reactor diameter as well as physical and chemical properties of the reactants and products could also affect the heat transfer especially in plant scale, which can determine the energy consumption. Such an absorption process can be more complete and hotter than separation via ammonia condensation. Therefore, the energy required for ammonia condensation and the reheating of the unreacted hydrogen and nitrogen can be eliminated.

Though with some limitations, this research is expected to bring some insight to enhancements of Haber Bosch process and to be helpful in further researches of ammonia absorptive reactors. This research has a good potential for improving per-pass conversion of ammonia production allowing for milder operating conditions and leading to reduced energy consumption. Furthermore, the mathematical modelling of ammonia absorptive reactors developed will be useful to provide a theoretical framework for improvement purposes in the future.

Appendix A Parameters used in RSM

Explanation	Equation	Data in Function
Binary acentric factor	$\omega_{ij} = \frac{\omega_i + \omega_j}{2}$	$\omega_{H_2} = -0.220$ $\omega_{N_2} = 0.040$ $\omega_{NH_3} = 0.253$
Binary ratio of the pair-potential energy to the Boltzmann constant	$\frac{\varepsilon_i}{k} = \frac{T_{ci}}{1.2593}$ $\frac{\varepsilon_{ij}}{k} = \left(\frac{\varepsilon_i}{k}\frac{\varepsilon_j}{k}\right)^{0.5}$	$T_{cH_2} = 33.2\ \mathrm{K}$ $T_{cN_2} = 126.2\ \mathrm{K}$ $T_{cNH_3} = 405.5\ \mathrm{K}$
Molecular weight of a binary mixture	$M_{ij} = \frac{2M_iM_j}{M_i + M_j}$	$M_{H_2} = 2\ \mathrm{g/mol}$ $M_{N_2} = 28\ \mathrm{g/mol}$ $M_{NH_3} = 17\ \mathrm{g/mol}$
Binary hard-sphere equivalent diameter	$\sigma_i = 0.809 V_{ci}^{\frac{1}{3}}$ $\sigma_{ij} = \left(\sigma_i\sigma_j\right)^{0.5}$	$V_{c,H_2} = 64.2\ \mathrm{cm^3/mol}$ $V_{c,N_2} = 90.1\ \mathrm{cm^3/mol}$ $V_{c,NH_3} = 69.8\ \mathrm{cm^3/mol}$
Hard-sphere equivalent diameter of a $H_2/N_2/NH_3$ mixture	$\sigma_m{}^3 = \sum_i \sum_j y_i y_j\, \sigma_{ij}{}^3$	
Ratio of the pair-potential energy to the Boltzmann constant for the $H_2/N_2/NH_3$ mixture	$(\varepsilon/k)_m = \frac{\left(\sum_i \sum_j y_i y_j (\frac{\varepsilon_{ij}}{k})\sigma_{ij}{}^3\right)}{\sigma_m{}^3}$	
Molecular weight of the $H_2/N_2/NH_3$ mixture using the Chung et al. mixing rules [127]	$M_m = \left[\frac{\sum_i \sum_j y_i y_j (\frac{\varepsilon_{ij}}{k})\sigma_{ij}{}^2 M_{ij}{}^{0.5}}{(\varepsilon/k)_m \sigma_m{}^2}\right]^2$ $\rho_m = \frac{P}{RT}$ $\rho_{w,m} = \rho_m M_m$	ρ_m is the molar density of the mixture, $\rho_{w,m}$ is the mass density of the mixture, and M_m is the molecular weight of the mixture

Table A.1. Chung et al. coefficients to calculate $E_i = a_i + b_i\omega + c_i\mu_r^4 + d_i\kappa$

i	a_i	b_i	c_i	d_i
1	6.324	50.412	-51.680	1189.0
2	0.00121	-0.001154	-0.006257	0.03728
3	5.283	254.209	-168.48	3898
4	6.623	38.096	-8.464	31.42
5	19.745	7.63	-14.354	31.53
6	-1.9	-12.537	4.985	-18.15
7	24.275	3.45	-11.291	69.35
8	0.7972	1.117	0.01235	-4.117
9	-0.2382	0.0677	-0.8163	4.025
10	0.06863	0.3479	0.5926	-0.727

Table A.2. Values of B_i in $B_i = a_i + b_i\omega + c_i\mu_r^4 + d_i\kappa$

i	a_i	b_i	c_i	d_i
1	2.4166	0.74824	-0.91858	121.72
2	-0.50924	-1.5094	-49.991	69.983
3	6.6107	5.6207	64.760	27.039
4	14.543	-8.9139	-5.6379	74.344
5	0.79274	0.82019	-0.69369	6.3173
6	-5.8634	12.801	9.5893	65.529
7	91.089	128.11	-54.217	523.81

Constants in Equation (3.24):

$$\Omega_v = A(T^*)^{-B} + C\,exp(-DT^*) + E\,exp(-FT^*)$$

A = 1.16145, B = 0.14874, C = 0.52487, D = 0.77320, E = 2.16178, F = 2.43787

Dipole moments: $\eta_{N_2} = 0$ D, $\eta_{H_2} = 0$ D, $\eta_{NH_3} = 1.5$ D

The changes of pressure along the reactor (absorber) are neglected, which has been checked using Ergun equation.

$$\Delta P = \frac{150\eta_{m,f}L}{d_p^2}\frac{(1-\varepsilon)^2}{\varepsilon^3}u_{s,f} + \frac{1.75\rho_{m,f}L}{d_p}\frac{(1-\varepsilon)}{\varepsilon^3}u_{s,f}|u_{s,f}| \approx 230\ Pa$$

where $\eta_{m,f}$ is the fluid viscosity, d_p is the pellet diameter in the fixed bed, ε is the void fraction of the fixed bed, $u_{s,f}$ is the fluid superficial velocity, $\rho_{m,f}$ is the mass density of fluid, and L is the length of the bed. The pressure drop is about 230 Pa along the absorber and can be neglected compared to the operating pressure at 50 bar or 10 bar.

The texture or topography of a surface of absorbent material was not tested in this project. However, the morphology of $MgCl_2$ can be searched from literature. For example, the SEM images of $MgCl_2{\cdot}6H_2O$ and $MgCl_2{\cdot}H_2O$ [183].

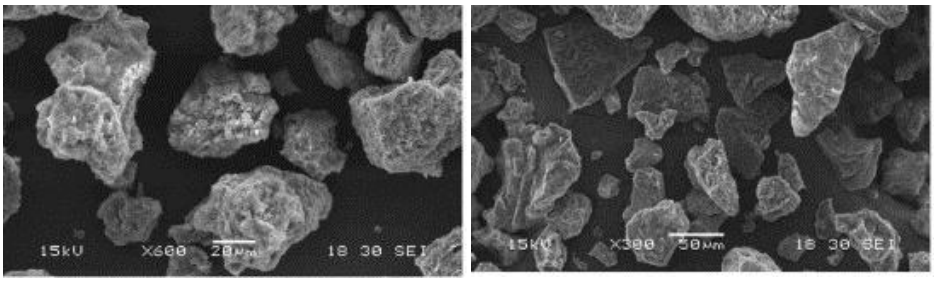

Figure A. SEM images of $MgCl_2{\cdot}6H_2O$ and $MgCl_2{\cdot}H_2O$ [183].

There are some experimental studies for the absorption capacity of ammonia absorbent. The sorbent capacity is calculated based on the cumulative weight of support and salt. Metal halides have extraordinary capacity for ammonia storage. However, achieving equilibrium capacity (maximum capacity) is difficult, and the absorption may take longer to achieve its full capacity. The absorbent capacity can be varied by changing salt chemistry [130].

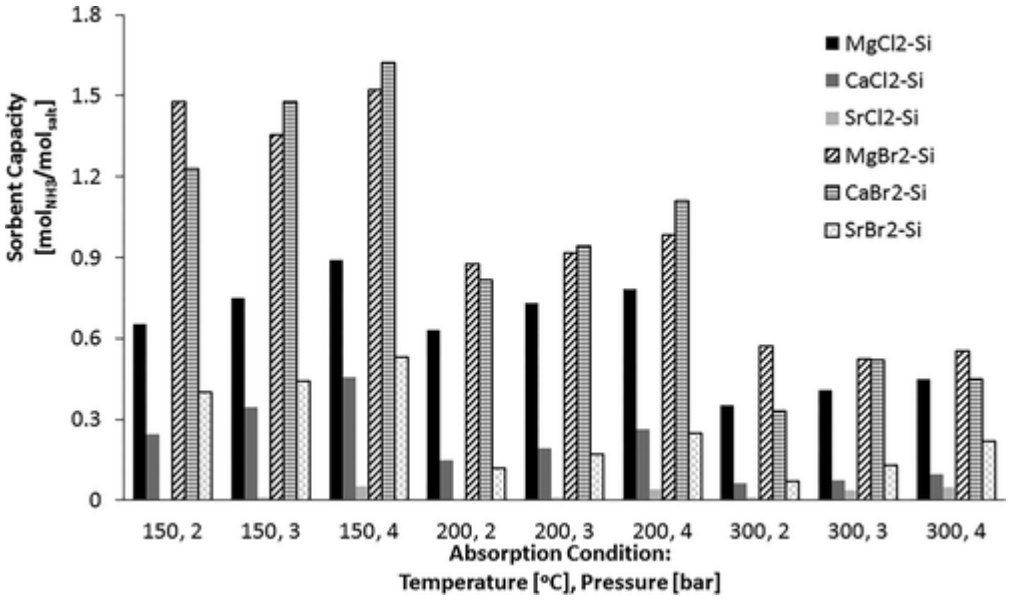

Figure B. Ammonia absorption capacity by different salts [130].

Appendix B Parameters used in BCM

Table B.1. Parameters used in the simulation of the conventional reactor

Input	Value	Explanation
T_cat	673	Temperature (K)
P	10	Pressure (bar)
alpha	0.5	Reaction factor (1)
void	0.4	Fixed bed void (1)
A	5.024×10^{-5}	Cross-sectional area of reactor (m^2)
n_cat_cell	8	Cell number of the catalyst bed (1)

Table B.2. Parameters used in the model of the absorptive reactor

Input	Value	Explanation
T_cat	673	Temperature (K)
T_abs	443	Temperature (K)
P	10	Pressure (bar)
alpha	0.5	Reaction factor (1)
void	0.4	Fixed bed void (1)
A	5.024×10^{-5}	Cross-sectional area of reactor (m^2)
Backflow factor	0.5	Backflow ratio (1)
n_cat_cell	8	Cell number of catalyst bed (1)
n_abs_cell	10	Cell number of absorbent bed (1)

Appendix C Data in Fluent simulation

The concepts of nodes, faces, and cells in the mesh are displayed in Figure C.1.

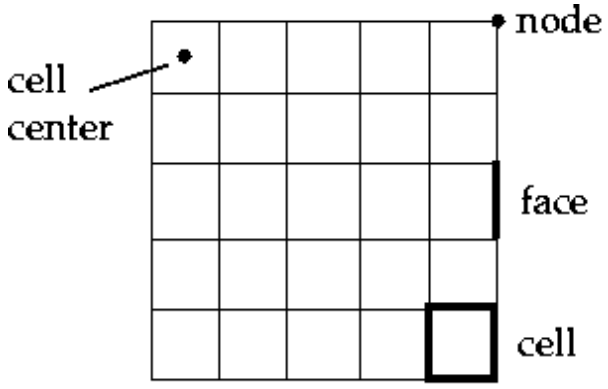

Figure C.1. The schematic of nodes, faces, and cells in the mesh.

Table C.1. Fluent mesh statistics.

Type	**Number**
Cells	24,000
Faces	48,400
Nodes	24,400
Cell zones	2
Face zones	7

Table C.2. Approximate diffusion coefficients of ammonia in magnesium chloride [114]

Temperature (°C)	Partition Coefficient (atm cm^3/mol)	Diffusion Coefficient (cm^2/s)
170	2.2×10^{-2}	2.0×10^{-13}
300	7.5×10^{-4}	5.0×10^{-11}

Solid Phase Heat Capacity (Shomate Equation) of $MgCl_2$ [154]**.**

heat capacity (J/mol*K)

$$Cp = A + Bt + Ct^2 + Dt^3 + \frac{E}{t^2}$$

standard entropy (J/mol*K)

$$S = Aln(t) + Bt + \frac{Ct^2}{2} + \frac{Dt^3}{3} - \frac{E}{2t^2} + G$$

standard enthalpy (kJ/mol)

$$H^0 - H^0_{298.15} = At + \frac{Bt^2}{2} + \frac{Ct^3}{3} + \frac{Dt^4}{4} - \frac{E}{t} + F - H$$

in which $t = \frac{T}{1000}$, T temperature in K.

A	B	C	D	E	F	G	H
78.30	2.43	6.86	-1.73	-0.73	-667.58	179.26	-641.61

The calculation of ammonia synthesis conversion is shown in Table C.3. At the start, the basis moles amount of reactants are taken as 1 mole of nitrogen and 3 moles of hydrogen with zero ammonia. It is assumed that x moles of nitrogen were consumed during the reaction, and therefore, the mole amount of nitrogen, hydrogen and ammonia are 1-x, 3-3x, and 2x respectively at the end.

Table C.3. Calculation of ammonia synthesis conversion.

	N_2 +	$3H_2$ ⇄	$2NH_3$	Total amount
start	1	3	0	4
variation	-x	-3x	2x	-2x
end	1-x	3-3x	2x	4-2x

The mole fraction of ammonia can be obtained from the simulation results in Figure 5.8, 4.92%. Therefore, the equation is:

$$\text{mole fraction of } NH_3 = \frac{moles\ amount\ of\ NH_3}{total\ moles\ amount\ of\ all\ species} = \frac{2x}{4-2x} = 4.92\%$$

We have

$$\text{x} = 0.094\ mole$$

Then, the conversion of ammonia synthesis is (N_2 is the limiting reactant):

$$\text{Conversion} = \frac{moles\ of\ N_2\ reacted}{moles\ of\ N_2\ fed} = \frac{0.094\ mole}{1\ mole} = 9.4\%$$

The mole fraction of ammonia can be obtained from the simulation results in Figure 6.3, 52%. Therefore, the equation is:

$$\text{mole fraction of } NH_3 = \frac{moles\ amount\ of\ NH_3}{total\ moles\ amount\ of\ all\ species} = \frac{2x}{4-2x} = 52\%$$

We have

$$\text{x} = 0.684\ mole$$

Then, the conversion of ammonia synthesis is (N_2 is the limiting reactant):

$$\text{Conversion} = \frac{moles\ of\ N_2\ reacted}{moles\ of\ N_2\ fed} = \frac{0.684\ mole}{1\ mole} = 68.4\%$$

For the four-bed (1-1-1-1) configuration, based on Figure 6.5, the mole fraction after the first bed (catalyst bed) is the same as for the four-bed (1-2-1-2) configuration; However, ammonia was not totally absorbed in the second bed (absorbent bed), the initial mole fraction of ammonia in the third bed (catalyst bed) is 0.26 from Figure 6.5; therefore, assuming that the total amount of species is 1 mole, then the basis moles of ammonia is 0.26 mole, and because of the 1: 3 ratio of nitrogen and hydrogen, their amounts are 0.185 and 0.555 moles respectively. The calculation of ammonia synthesis conversion is shown in the Table C.4:

Table C.4. Calculation of ammonia synthesis conversion.

	N_2 +	$3H_2$ ⇄	$2NH_3$	Total amount
start	0.185	0.555	0.26	1
variation	-x	-3x	2x	-2x
end	0.185-x	0.555-3x	0.26+2x	1-2x

The mole fraction of ammonia after the third bed (catalyst bed) can be obtained from Figure 6.5, 46%. Therefore, the equation is:

$$\text{mole fraction of } NH_3 = \frac{moles\ amount\ of\ NH_3}{total\ moles\ amount\ of\ all\ species} = \frac{0.26 + 2x}{1 - 2x} = 46\%$$

We have

$$\text{x} = 0.0685\ mole$$

Then, the conversion of ammonia synthesis is:

$$\text{Conversion} = \frac{moles\ of\ N_2\ reacted}{moles\ of\ N_2\ fed} = \frac{0.0685\ mole}{0.185\ mole} = 37\%$$

The conversion in the third bed (catalyst bed) is 37%.

References

[1] J. W. Erisman, M. A. Sutton, J. Galloway, Z. Klimont, and W. Winiwarter, “How a century of ammonia synthesis changed the world,” *Nat. Geosci.*, vol. 1, no. 10, pp. 636–639, 2008, doi: 10.1038/ngeo325.

[2] A. Klerke, C. H. Christensen, J. K. Nørskov, and T. Vegge, “Ammonia for hydrogen storage: Challenges and opportunities,” *J. Mater. Chem.*, vol. 18, no. 20, pp. 2304–2310, 2008, doi: 10.1039/b720020j.

[3] A. Bruce and T. Faunce, “Sustainable fuel, food, fertilizer and ecosystems through a global artificial photosynthetic system: Overcoming anticompetitive barriers,” *Interface Focus*, vol. 5, no. 3, pp. 1–9, 2015, doi: 10.1098/rsfs.2015.0011.

[4] M. Appl, *Ammonia : principles and industrial practice*. Weinheim : Wiley-VCH, 1999.

[5] N. Saadatjou, A. Jafari, and S. Sahebdelfar, “Ruthenium Nanocatalysts for Ammonia Synthesis: A Review,” *Chem. Eng. Commun.*, vol. 202, no. 4, pp. 420–448, 2015, doi: 10.1080/00986445.2014.923995.

[6] C. Smith, A. V McCormick, and E. L. Cussler, “Optimizing the Conditions for Ammonia Production Using Absorption,” *ACS Sustain. Chem. Eng.*, vol. 7, no. 4, pp. 4019–4029, 2019, doi: 10.1021/acssuschemeng.8b05395.

[7] D. K. Ojha, M. J. Kale, A. V McCormick, M. Reese, M. Malmali, P. Dauenhauer, and E. L. Cussler, “Integrated Ammonia Synthesis and Separation,” *ACS Sustain. Chem. Eng.*, 2019, doi: 10.1021/acssuschemeng.9b03050.

[8] M. Appl, “Ammonia,” *Ullmann’s Encyclopedia of Industrial Chemistry*. 2006, doi: 10.1002/14356007.a02_143.pub2.

[9] L. Ye, R. Nayak-Luke, R. Bañares-Alcántara, and E. Tsang, “Reaction: ‘Green’ Ammonia Production,” *Chem*, vol. 3, no. 5, pp. 712–714, 2017, doi: https://doi.org/10.1016/j.chempr.2017.10.016.

[10] M. H. Khademi and R. S. Sabbaghi, “Comparison between three types of ammonia synthesis reactor configurations in terms of cooling methods,” *Chem. Eng. Res. Des.*, vol. 128, pp. 306–317, 2017, doi: https://doi.org/10.1016/j.cherd.2017.10.021.

[11] C. J. M. Van Der Ham, M. T. M. Koper, and D. G. H. Hetterscheid, “Challenges in reduction of dinitrogen by proton and electron transfer,” *Chem. Soc. Rev.*, vol. 43, no. 15, pp. 5183–5191, 2014, doi: 10.1039/c4cs00085d.

[12] H. Hirakawa, M. Hashimoto, Y. Shiraishi, and T. Hirai, “Photocatalytic Conversion of Nitrogen to Ammonia with Water on Surface Oxygen Vacancies of Titanium Dioxide,” *J. Am. Chem. Soc.*, vol. 139, no. 31, pp. 10929–10936, Aug. 2017, doi: 10.1021/jacs.7b06634.

[13] M. E. Gálvez, M. Halmann, and A. Steinfeld, “Ammonia Production via a Two-Step Al_2O_3/AlN Thermochemical Cycle. 1. Thermodynamic, Environmental, and Economic Analyses,” *Ind. Eng. Chem. Res.*, vol. 46, no. 7, pp. 2042–2046, 2007, doi: 10.1021/ie061550u.

[14] K. Wagner, M. Malmali, C. Smith, A. McCormick, E. L. Cussler, M. Zhu, and N. C. A. Seaton, “Column absorption for reproducible cyclic separation in small scale ammonia synthesis,” *AIChE J.*, vol. 63, no. 7, pp. 3058–3068, 2017, doi: 10.1002/aic.15685.

[15] V. Kordali, G. Kyriacou, and C. Lambrou, “Electrochemical synthesis of ammonia at atmospheric pressure and low temperature in a solid polymer electrolyte cell,” *Chem. Commun.*, no. 17, pp. 1673–1674, 2000, doi: 10.1039/b004885m.

[16] C. Guo, J. Ran, A. Vasileff, and S.-Z. Qiao, “Rational design of electrocatalysts and photo(electro)catalysts for nitrogen reduction to ammonia (NH_3) under ambient

conditions," *Energy Environ. Sci.*, vol. 11, no. 1, pp. 45–56, 2018, doi: 10.1039/c7ee02220d.

[17] M. A. Shipman and M. D. Symes, "Recent progress towards the electrosynthesis of ammonia from sustainable resources," *Catal. Today*, vol. 286, pp. 57–68, 2017, doi: https://doi.org/10.1016/j.cattod.2016.05.008.

[18] F. Zhou, L. M. Azofra, M. Ali, M. Kar, A. N. Simonov, C. McDonnell-Worth, C. Sun, X. Zhang, and D. R. MacFarlane, "Electro-synthesis of Ammonia from Nitrogen at Ambient Temperature and Pressure in Ionic Liquids," *Energy Environ. Sci.*, vol. 10, Nov. 2017, doi: 10.1039/C7EE02716H.

[19] D. Bao, Q. Zhang, F. Meng, H. Zhong, M. Shi, Y. Zhang, J. Yan, Q. Jiang, and X. Zhang, "Electrochemical Reduction of N_2 under Ambient Conditions for Artificial N_2 Fixation and Renewable Energy Storage Using N_2/NH_3 Cycle," *Adv. Mater.*, vol. 29, no. 3, p. 1604799, Jan. 2017, doi: 10.1002/adma.201604799.

[20] D. Yang, T. Chen, and Z. Wang, "Electrochemical reduction of aqueous nitrogen (N_2) at a low overpotential on (110)-oriented Mo nanofilm," *J. Mater. Chem. A*, vol. 5, no. 36, pp. 18967–18971, 2017, doi: 10.1039/c7ta06139k.

[21] K. Kim, N. Lee, C. Y. Yoo, J. N. Kim, H. C. Yoon, and J. I. Han, "Communication—Electrochemical Reduction of Nitrogen to Ammonia in 2-Propanol under Ambient Temperature and Pressure," *J. Electrochem. Soc.*, vol. 163, no. 7, pp. F610–F612, 2016, doi: 10.1149/2.0231607jes.

[22] J. Jones, H. Xiong, A. T. DeLaRiva, E. J. Peterson, H. Pham, S. R. Challa, G. Qi, S. Oh, M. H. Wiebenga, X. I. P. Hernandez, Y. Wang, and A. K. Datye, "Thermally stable single-atom platinum-on-ceria catalysts via atom trapping," *Science.*, vol. 353, no. 6295, pp. 150 – 154, 2016, doi: 10.1126/science.aaf8800.

[23] W. Qiu, X. Xie, J. Qiu, W. Fang, R. Liang, X. Ren, X. Ji, G. Cui, A. M. Asiri, G. Cui, B.Tang, and X. Sun, "High-performance artificial nitrogen fixation at ambient

conditions using a metal-free electrocatalyst," *Nat. Commun.*, vol. 9, no. 1, p. 3485, 2018, doi: 10.1038/s41467-018-05758-5.

[24] R. Küngas, P. Blennow, T. Heiredal-Clausen, T. H. Norby, J. Rass-Hansen, J. B. Hansen, and P. G. Moses, "Progress in SOEC Development Activities at Haldor Topsøe," *ECS Trans.*, vol. 91, no. 1, pp. 215–223, 2019, doi: 10.1149/09101.0215ecst.

[25] I. Garagounis, A. Vourros, D. Stoukides, D. Dasopoulos, and M. Stoukides, "Electrochemical Synthesis of Ammonia: Recent Efforts and Future Outlook.," *Membranes.*, vol. 9, no. 9, Aug. 2019, doi: 10.3390/membranes9090112.

[26] A. J. Medford and M. C. Hatzell, "Photon-Driven Nitrogen Fixation: Current Progress, Thermodynamic Considerations, and Future Outlook," *ACS Catal.*, vol. 7, no. 4, pp. 2624–2643, Apr. 2017, doi: 10.1021/acscatal.7b00439.

[27] T. Hisatomi, J. Kubota, and K. Domen, "Recent advances in semiconductors for photocatalytic and photoelectrochemical water splitting," *Chem. Soc. Rev.*, vol. 43, no. 22, pp. 7520–7535, 2014, doi: 10.1039/c3cs60378d.

[28] A. Kubacka, M. Fernández-García, and G. Colón, "Advanced Nanoarchitectures for Solar Photocatalytic Applications," *Chem. Rev.*, vol. 112, no. 3, pp. 1555–1614, Mar. 2012, doi: 10.1021/cr100454n.

[29] M. Guan, C. Xiao, J. Zhang, S. Fan, R. An, Q. Cheng, J. Xie, M. Zhou, B. Ye, and Y. Xie, "Vacancy associates promoting solar-driven photocatalytic activity of ultrathin bismuth oxychloride nanosheets," *J. Am. Chem. Soc.*, vol. 135, no. 28, pp. 10411–10417, 2013, doi: 10.1021/ja402956f.

[30] W. Hou and S. B. Cronin, "A Review of Surface Plasmon Resonance-Enhanced Photocatalysis," *Adv. Funct. Mater.*, vol. 23, no. 13, pp. 1612–1619, Apr. 2013, doi: 10.1002/adfm.201202148.

[31] G. N. Schrauzer and T. D. Guth, “Photolysis of Water and Photoreduction of Nitrogen on Titanium Dioxide,” *J. Am. Chem. Soc.*, vol. 99, no. 22, pp. 7189–7193, 1977, doi: 10.1021/ja00464a015.

[32] D. S. Bhachu, S. J. A. Moniz, S. Sathasivam, D. O. Scanlon, A. Walsh, S. M. Bawaked, M. Mokhtar, A. Y. Obiad, I. Parkin, J. J. Tang, and C. J. Carmalt, “Bismuth oxyhalides: Synthesis, structure and photoelectrochemical activity,” *Chem. Sci.*, vol. 7, no. 8, pp. 4832–4841, 2016, doi: 10.1039/c6sc00389c.

[33] S. Linic, P. Christopher, and D. Ingram, “Plasmonic-metal nanostructures for efficient conversion of solar to chemical energy,” *Nat. Mater.*, vol. 10, pp. 911–921, Nov. 2011, doi: 10.1038/nmat3151.

[34] T. Oshikiri, K. Ueno, and H. Misawa, “Plasmon-Induced Ammonia Synthesis through Nitrogen Photofixation with Visible Light Irradiation,” *Angew. Chemie Int. Ed.*, vol. 53, no. 37, pp. 9802–9805, Sep. 2014, doi: 10.1002/anie.201404748.

[35] N. Zhang, A. Jalil, D. Wu, S. Chen, Y. Liu, C. Gao, W. Ye, Z. Qi, H. Ju, C. Wang, X. Wu, L. Song, J. Zhu, and Y. Xiong, “Refining Defect States in $W_{18}O_{49}$ by Mo Doping: A Strategy for Tuning N_2 Activation towards Solar-Driven Nitrogen Fixation,” *J. Am. Chem. Soc.*, vol. 140, no. 30, pp. 9434–9443, Aug. 2018, doi: 10.1021/jacs.8b02076.

[36] J. Adanez, A. Abad, F. Garcia-Labiano, P. Gayan, and L. F. de Diego, “Progress in Chemical-Looping Combustion and Reforming technologies,” *Prog. Energy Combust. Sci.*, vol. 38, no. 2, pp. 215–282, 2012, doi: https://doi.org/10.1016/j.pecs.2011.09.001.

[37] M. E. Gálvez, A. Frei, M. Halmann, and A. Steinfeld, “Ammonia Production via a Two-Step Al_2O_3/AlN Thermochemical Cycle. 2. Kinetic Analysis,” *Ind. Eng. Chem. Res.*, vol. 46, no. 7, pp. 2047–2053, Mar. 2007, doi: 10.1021/ie061551m.

[38] R. Michalsky, A. Avram, B. Peterson, P. H. Pfromm, and A. Peterson, “Chemical looping of metal nitride catalysts: Low-pressure ammonia synthesis for energy storage,” *Chem. Sci.*, vol. 6, May 2015, doi: 10.1039/C5SC00789E.

[39] G. Wenbo, J. Guo, P. Wang, Q. Wang, F. Chang, Q. Pei, W. Zhang, L. Liu, and P. Chen, “Production of ammonia via a chemical looping process based on metal imides as nitrogen carriers,” *Nat. Energy*, vol. 3, Dec. 2018, doi: 10.1038/s41560-018-0268-z.

[40] C. J. Bartel, J. R. Rumptz, A. W. Weimer, A. M. Holder, and C. B. Musgrave, “High-Throughput Equilibrium Analysis of Active Materials for Solar Thermochemical Ammonia Synthesis,” *ACS Appl. Mater. Interfaces*, vol. 11, no. 28, pp. 24850–24858, Jul. 2019, doi: 10.1021/acsami.9b01242.

[41] K. P. Ramaiyan, S.Ozden, S. Maurya, D. Kelly, S. K. Babu, A. Benavidez, F. G. Garzon, Y. S. Kim, C. R. Kreller, and R. Mukundan, “Molybdenum Carbide Electrocatalysts for Electrochemical Synthesis of Ammonia from Nitrogen: Activity and Stability,” *J. Electrochem. Soc.*, vol. 167, no. 4, 2020, doi: 10.1149/1945-7111/ab7097.

[42] F. Ni and H. S. Caram, “Sorption enhanced reaction for high purity products in reversible reactions,” *AIChE J.*, vol. 63, no. 12, pp. 5452–5461, 2017, doi: 10.1002/aic.15943.

[43] S. Rawadieh and V. G. Gomes, “Steam reforming for hydrogen generation with in situ adsorptive separation,” *Int. J. Hydrogen Energy*, vol. 34, no. 1, pp. 343–355, 2009, doi: 10.1016/j.ijhydene.2008.10.038.

[44] A. J. Kodde, Y. S. Fokma, and A. Bliek, “Selectivity Effects on Series Reactions by Reactant Storage and PSA Operation,” vol. 46, no. 11, 2000.

[45] M. Hussainy and D. W. Agar, “Structural and Operational Optimality of Adsorptive Reactors,” *Chem. Eng. Technol.*, vol. 39, no. 11, pp. 2135–2141, 2016, doi: 10.1002/ceat.201600197.

[46] M. P. Elsner, C. Dittrich, and D. W. Agar, “Adsorptive reactors for enhancing equilibrium gas-phase reactions—two case studies,” *Chem. Eng. Sci.*, vol. 57, no. 9, pp. 1607–1619, 2002, doi: https://doi.org/10.1016/S0009-2509(02)00037-4.

[47] M. J. Kale, D. K. Ojha, S. Biswas, J. I. Militti, A. V. McCormick, J. H. Schott, P. J. Dauenhauer, and E. L. Cussler, “Optimizing Ammonia Separation via Reactive Absorption for Sustainable Ammonia Synthesis,” *ACS Appl. Energy Mater.*, 2020, doi: 10.1021/acsaem.9b02278.

[48] M. J. Palys, A. McCormick, E. L. Cussler, and P. Daoutidis, “Modeling and Optimal Design of Absorbent Enhanced Ammonia Synthesis,” *Processes*, vol. 6, no. 7, p. 91, 2018, doi: 10.3390/pr6070091.

[49] E. Cussler, A. McCormick, M. Reese, and M. Malmali, “Ammonia Synthesis at Low Pressure,” *J. Vis. Exp.*, no. 126, p. 55691, 2017, doi: 10.3791/55691.

[50] M. Malmali, M. Reese, A. V McCormick, and E. L. Cussler, “Converting Wind Energy to Ammonia at Lower Pressure,” *ACS Sustain. Chem. Eng.*, vol. 6, no. 1, pp. 827–834, 2018, doi: 10.1021/acssuschemeng.7b03159.

[51] T. Zhang, H. Miyaoka, H. Miyaoka, T. Ichikawa, and Y. Kojima, “Review on Ammonia Absorption Materials: Metal Hydrides, Halides, and Borohydrides,” *ACS Appl. Energy Mater.*, vol. 1, no. 2, pp. 232–242, Feb. 2018, doi: 10.1021/acsaem.7b00111.

[52] H. Leng, T. Ichikawa, S. Hino, N. Hanada, S. Isobe, and H. Fujii, “Synthesis and decomposition reactions of metal amides in metal-N-H hydrogen storage system,” *J. Power Sources*, vol. 156, pp. 166–170, Jun. 2006, doi: 10.1016/j.jpowsour.2005.03.228.

[53] T. D. Elmøe, R. Z. Sørensen, U. Quaade, C. H. Christensen, J. K. Nørskov, and T. Johannessen, “A high-density ammonia storage/delivery system based on $Mg(NH_3)_6Cl_2$ for SCR-DeNOx in vehicles,” *Chem. Eng. Sci.*, vol. 61, no. 8, pp. 2618–2625, 2006, doi: 10.1016/j.ces.2005.11.038.

[54] C. Y. Liu and K. Aika, “Ammonia Absorption into Alkaline Earth Metal Halide Mixtures as an Ammonia Storage Material,” pp. 7484–7491, 2004.

[55] H. Reardon, J. Hanlon, M. Grant, I. Fullbrook, and D. Gregory, “Ammonia uptake and release in the MnX_2-NH_3 (X = Cl, Br) systems and structure of the $Mn(NH_3)nX_2$ (n = 6, 2) ammines,” *Crystals*, vol. 2, p. 193, Apr. 2012, doi: 10.3390/cryst2020193.

[56] J. S. Hummelshøj, R. Z. Sørensen, M. Y. Kustova, T. Johannessen, J. K. Nørskov, and C. H. Christensen, “Generation of Nanopores during Desorption of NH_3 from $Mg(NH_3)6Cl_2$,” *J. Am. Chem. Soc.*, vol. 128, no. 1, pp. 16–17, Jan. 2006, doi: 10.1021/ja0556070.

[57] C. Y. Liu and K. Aika, “Ammonia Absorption on Alkaline Earth Halides as Ammonia Separation and Storage Procedure,” *Bull. Chem. Soc. Jpn.*, vol. 77, no. 1, pp. 123–131, Jan. 2004, doi: 10.1246/bcsj.77.123.

[58] M. Kubota, K. Matsuo, R. Yamanouchi, and H. Matsuda, “Absorption and Desorption Characteristics of NH_3 with Metal Chlorides for Ammonia Storage,” *J. Chem. Eng. JAPAN*, vol. advpub, 2014, doi: 10.1252/jcej.13we294.

[59] T. Aoki, T. Ichikawa, H. Miyaoka, and Y. Kojima, “Thermodynamics on Ammonia Absorption of Metal Halides and Borohydrides,” *J. Phys. Chem. C*, vol. 118, no. 32, pp. 18412–18416, Aug. 2014, doi: 10.1021/jp5049474.

[60] P. Neveu and J. Castaing, “Solid-gas chemical heat pumps: Field of application and performance of the internal heat of reaction recovery process,” *Heat Recover. Syst. CHP*, vol. 13, no. 3, pp. 233–251, 1993, doi: https://doi.org/10.1016/0890-4332(93)90014-M.

[61] S. Wu, T. X. Li, and R. Z. Wang, “Experimental identification and thermodynamic analysis of ammonia sorption equilibrium characteristics on halide salts,” *Energy*, vol. 161, pp. 955–962, 2018, doi: https://doi.org/10.1016/j.energy.2018.07.129.

[62] A. D. Grekova, J. V Veselovskaya, M. M. Tokarev, T. A. Krieger, A. N. Shmakov, and L. G. Gordeeva, “Ammonia sorption on the composites ‘($BaCl_2$+$BaBr_2$) inside

vermiculite pores,'" *Colloids Surfaces A Physicochem. Eng. Asp.*, vol. 448, pp. 169–174, 2014, doi: https://doi.org/10.1016/j.colsurfa.2014.02.025.

[63] G. L. An, L. W. Wang, J. Gao, and R. Z. Wang, "A review on the solid sorption mechanism and kinetic models of metal halide-ammonia working pairs," *Renew. Sustain. Energy Rev.*, vol. 91, pp. 783–792, 2018, doi: https://doi.org/10.1016/j.rser.2018.04.032.

[64] M. Lebrun and B. Spinner, "Models of heat and mass transfers in solid-gas reactors used as chemical heat pumps," *Chem. Eng. Sci.*, vol. 45, no. 7, pp. 1743–1753, 1990, doi: 10.1016/0009-2509(90)87052-T.

[65] B. Jiang and H. Guo, "Prediction of mode specificity, bond selectivity, normal scaling, and surface lattice effects in water dissociative chemisorption on several metal surfaces using the sudden vector projection model," *J. Phys. Chem. C*, vol. 118, no. 46, pp. 26851–26858, 2014, doi: 10.1021/jp5090839.

[66] B. Jackson, F. Nattino, and G.-J. Kroes, "Dissociative chemisorption of methane on metal surfaces: Tests of dynamical assumptions using quantum models and ab initio molecular dynamics," *J. Chem. Phys.*, vol. 141, no. 5, 2014, doi: 10.1063/1.4891327.

[67] T. Liu, B. Fu, and D. H. Zhang, "Validity of the site-averaging approximation for modeling the dissociative chemisorption of H_2 on Cu(111) surface: A quantum dynamics study on two potential energy surfaces," *J. Chem. Phys.*, vol. 141, no. 19, p. 194302, Nov. 2014, doi: 10.1063/1.4901894.

[68] F. Schueth, R. Palkovits, R. Schloegl, and D. S. Su, "Ammonia as a possible element in an energy infrastructure: catalysts for ammonia decomposition," *Energy Environ. Sci.*, vol. 5, no. 4, pp. 6278–6289, Apr. 2012, doi: 10.1039/c2ee02865d.

[69] H. Liu, "Ammonia synthesis catalyst 100 years: Practice, enlightenment and challenge," *Chinese J. Catal.*, vol. 35, no. 10, pp. 1619–1640, 2014, doi: https://doi.org/10.1016/S1872-2067(14)60118-2.

[70] J. R. Jennings, *Catalytic ammonia synthesis, fundamentals and practice*. United States: Plenum Press, 1991.

[71] M. Hara, M. Kitano, and H. Hosono, “Ru-Loaded $C_{12}A_7$:e– Electride as a Catalyst for Ammonia Synthesis,” *ACS Catal.*, vol. 7, no. 4, pp. 2313–2324, Apr. 2017, doi: 10.1021/acscatal.6b03357.

[72] G. C. Bond, *Heterogeneous catalysis : principles and applications*, 2nd ed. Oxford: Clarendon Press, 1987.

[73] Z. Lendzion-Bieluñ, W. Arabczyk, and M. Figurski, “The effect of the iron oxidation degree on distribution of promotors in the fused catalyst precursors and their activity in the ammonia synthesis reaction,” *Appl. Catal. A Gen.*, vol. 227, no. 1–2, pp. 255–263, 2002, doi: 10.1016/S0926-860X(01)00938-3.

[74] K. Aika, H. Hori, and A. Ozaki, “Activation of nitrogen by alkali metal promoted transition metal I. Ammonia synthesis over ruthenium promoted by alkali metal,” *J. Catal.*, vol. 27, no. 3, pp. 424–431, 1972, doi: 10.1016/0021-9517(72)90179-0.

[75] P. Puspitasari and N. Yahya, “Development of ammonia synthesis,” in *2011 National Postgraduate Conference*, 2011, pp. 1–4, doi: 10.1109/NatPC.2011.6136449.

[76] M. Nishi, S.-Y. Chen, and H. Takagi, “A Mesoporous Carbon-Supported and Cs-promoted Ru Catalyst with Enhanced Activity and Stability for Sustainable Ammonia Synthesis,” *ChemCatChem*, vol. 10, no. 16, pp. 3411–3414, Aug. 2018, doi: 10.1002/cctc.201800556.

[77] J. K. Norskov, “Electronic Factors in Catalysis,” *Prog. Surf. Sci.*, vol. 38, no. 2, pp. 103–144, 1991, doi: 10.1016/0079-6816(91)90007-Q.

[78] L. Forni, D. Molinari, I. Rossetti, and N. Pernicone, “Carbon-supported promoted Ru catalyst for ammonia synthesis,” *Appl. Catal. A Gen.*, vol. 185, no. 2, pp. 269–275, 1999, doi: 10.1016/S0926-860X(99)00144-1.

[79] K. Aika, T. Takano, and S. Murata, “Preparation and characterization of chlorine-free ruthenium catalysts and the promoter effect in ammonia synthesis: 3. A magnesia-supported ruthenium catalyst,” *J. Catal.*, vol. 136, no. 1, pp. 126–140, 1992, doi: https://doi.org/10.1016/0021-9517(92)90112-U.

[80] J. Wellenbüscher, M. Muhler, W. Mahdi, U. Sauerlandt, J. Schütze, G. Ertl, and R. Schlogl, “Ruthenium supported on zeolite A: preparation and characterisation of a stable catalyst for ammonia synthesis,” *Catal. Letters*, vol. 25, no. 1, pp. 61–74, 1994, doi: 10.1007/BF00815416.

[81] I. Rossetti, N. Pernicone, and L. Forni, “Promoters effect in Ru/C ammonia synthesis catalyst,” *Appl. Catal. A Gen.*, vol. 208, no. 1–2, pp. 271–278, 2001, doi: 10.1016/S0926-860X(00)00711-0.

[82] B. Lin, Y. Liu, L. Heng, X. Wang, J. Ni, J. Lin, and L. Jiang, “Morphology Effect of Ceria on the Catalytic Performances of Ru/CeO_2 Catalysts for Ammonia Synthesis,” *Ind. Eng. Chem. Res.*, vol. 57, no. 28, pp. 9127–9135, Jul. 2018, doi: 10.1021/acs.iecr.8b02126.

[83] Y. Niwa and K. Aika, “The effect of lanthanide oxides as a support for ruthenium catalysts in ammonia synthesis,” *J. Catal.*, vol. 162, no. 1, pp. 138–142, Aug. 1996, doi: 10.1006/jcat.1996.0268.

[84] Y. Ogura, K. Sato, S. I. Miyahara, Y. Kawano, T. Toriyama, T. Yamamoto, S. Matsumura, S, Hosokawa, and K. Nagaoka, “Efficient ammonia synthesis over a $Ru/La_{0.5}Ce_{0.5}O_{1.75}$ catalyst pre-reduced at high temperature,” *Chem. Sci.*, vol. 9, no. 8, pp. 2230–2237, 2018, doi: 10.1039/C7SC05343F.

[85] Y. Ogura, K. Tsujimaru, K. Sato, S. I. Miyahara, T. Toriyama, T. Yamamoto, S. Matsumura, and K. Nagaoka, “$Ru/La_{0.5}Pr_{0.5}O_{1.75}$ Catalyst for Low-Temperature Ammonia Synthesis,” *ACS Sustain. Chem. Eng.*, vol. 6, no. 12, pp. 17258–17266, Dec. 2018, doi: 10.1021/acssuschemeng.8b04683.

[86] P. Liu, R. Niu, W. Li, S. Wang, and J. Li, “Morphology Effect of Ceria on the Ammonia Synthesis Activity of Ru/CeO_2 Catalysts,” *Catal. Letters*, vol. 149, no. 4, pp. 1007–1016, 2019, doi: 10.1007/s10562-019-02674-1.

[87] M. Kitano, Y. Inoue, Y. Yamazaki, F. Hayashi, S. Kanbara, S. Matsuishi, T. Yokoyama, S. Kim, M. Hara, and H. Hosono, “Ammonia synthesis using a stable electride as an electron donor and reversible hydrogen store,” *Nat. Chem.*, vol. 4, p. 934, Oct. 2012.

[88] K. Aika, “Role of alkali promoter in ammonia synthesis over ruthenium catalysts—Effect on reaction mechanism,” *Catal. Today*, vol. 286, pp. 14–20, 2017, doi: https://doi.org/10.1016/j.cattod.2016.08.012.

[89] P. Wang, F. Chang, W. Gao, J. Guo, G. Wu, T. He, and P. Chen, “Breaking scaling relations to achieve low-temperature ammonia synthesis through LiH-mediated nitrogen transfer and hydrogenation,” *Nat. Chem.*, vol. 9, p. 64, Aug. 2016.

[90] M. Kitano, Y. Inoue, H. Ishikawa, K. Yamagata, T. Nakao, T. Tada, S. Matsuishi, T. Yokoyama, M. Hara, and H. Hosono, “Essential role of hydride ion in ruthenium-based ammonia synthesis catalysts,” *Chem. Sci.*, vol. 7, no. 7, pp. 4036–4043, 2016, doi: 10.1039/C6SC00767H.

[91] R. J. Farrauto and C. H. Bartholomew, *Fundamentals of industrial catalytic processes*. London: Blackie Academic & Professional, 1997.

[92] W. Rarog-Pilecka, E. Miskiewicz, D. Szmigiel, and Z. Kowalczyk, “Structure sensitivity of ammonia synthesis over promoted ruthenium catalysts supported on graphitised carbon,” *J. Catal.*, vol. 231, no. 1, pp. 11–19, Apr. 2005, doi: 10.1016/j.jcat.2004.12.005.

[93] S. Dahl, E. Tornqvist, and I. Chorkendorff, “Dissociative adsorption of N_2 on Ru(0001): A surface reaction totally dominated by steps,” *J. Catal.*, vol. 192, no. 2, pp. 381–390, Jun. 2000, doi: 10.1006/jcat.2000.2858.

[94] Á. Logadóttir and J. K. Nørskov, “Ammonia synthesis over a Ru(0001) surface studied by density functional calculations,” *J. Catal.*, vol. 220, no. 2, pp. 273–279, 2003, doi: https://doi.org/10.1016/S0021-9517(03)00156-8.

[95] S. Shetty, A. P. J. Jansen, and R. A. van Santen, “Active Sites for N_2 Dissociation on Ruthenium,” *J. Phys. Chem. C*, vol. 112, no. 46, pp. 17768–17771, Nov. 2008, doi: 10.1021/jp8085478.

[96] M. Y. Aslan, “Supported Ru based ammonia synthesis catalysts,” October, 2012.

[97] N. Nikačević, M. Jovanović, and M. Petkovska, “Enhanced ammonia synthesis in multifunctional reactor with in situ adsorption,” *Chem. Eng. Res. Des.*, vol. 89, no. 4, pp. 398–404, 2011, doi: 10.1016/j.cherd.2010.08.011.

[98] A. Dashti, K. Khorsand, M. A. Marvast, and M. Kakavand, “Modeling and simulation of ammonia synthesis reactor,” *Pet. Coal*, vol. 48, no. 2, pp. 15–23, 2006.

[99] R. M. M. Mattheij and J. Molenaar, *Ordinary differential equations in theory and practice*. Philadelphia: SIAM, c2002., 2002.

[100] K. W. Morton, *Numerical solution of partial differential equations*. Oxford, 1991.

[101] T. Merder, M. Warzecha, P. Warzecha, and A. M. Hutny, “Optimization of Steel Flow in the Tundish by Modifying its Working Area,” *Archives of Metallurgy and Materials*. Institute of Metallurgy and Materials Science of Polish Academy of Sciences, 2016.

[102] M. Orszulik, A. Fic, and T. Bury, “CFD modeling of passive autocatalytic recombiners,” *Nukleonika*, vol. 60, no. 2, pp. 347–353, 2015, doi: https://doi.org/10.1515/nuka-2015-0050.

[103] S. Y. Sitnikov, L. V Plotnikova, A. F. Dresvyannikov, N. S. Kiselev, and S. P. Mironov, “Modeling the process of convective mass transfer in a tubular electrochemical reactor,” *IOP Conf. Ser. Earth Environ. Sci.*, vol. 288, p. 12118, 2019, doi: 10.1088/1755-1315/288/1/012118.

[104] Y. S. Sanusi and E. M. A. Mokheimer, “Performance analysis of a membrane-based reformer-combustor reactor for hydrogen generation,” *Int. J. Energy Res.*, vol. 43, no. 1, pp. 189–203, Jan. 2019, doi: 10.1002/er.4250.

[105] S. Shwe Hla and M. D. Dolan, “CFD modelling of a membrane reactor for hydrogen production from ammonia,” *IOP Conf. Ser. Mater. Sci. Eng.*, vol. 297, p. 12027, 2018, doi: 10.1088/1757-899x/297/1/012027.

[106] S. Rabbani, M. Sassi, and T. Shamim, “Modeling of hydrodynamics of fine particles deposition in packed-bed reactors,” *J. Comput. Multiph. Flows*, vol. 9, no. 4, pp. 157–168, Jul. 2017, doi: 10.1177/1757482X17716045.

[107] Z. Wen and J. Petera, “Numerical Analysis of The Effect of Hydrodynamics and Operating Conditions on Biodiesel Synthesis in a Rotor-Stator Spinning Disk Reactor,” *Chemical and Process Engineering*, vol. 38. Polish Academy of Sciences Committee of Chemical and Process Engineering, p. 265, 2017.

[108] A. Snegirev, E. Kuznetsov, E. Markus, J. Harris, and B. Moravec, “Performance and calibration of two subgrid extinction models for turbulent diffusion combustion in an under-ventilated enclosure fire,” in *Journal of Physics: Conference Series*, 2018, vol. 1107, no. 4, doi: 10.1088/1742-6596/1107/4/042011.

[109] P. Babitz, D. Choe, and T. Jevremovic, “Feasibility study of the university of Utah TRIGA reactor power upgrade - part II: Thermohydraulics and heat transfer study in respect to cooling system requirements and design,” *Nucl. Technol. Radiat. Prot.*, vol. 28, no. 4, pp. 352–361, 2013, doi: 10.2298/NTRP1304352B.

[110] M. Z. Abdullah and N. A. Mohamed Rashidi, “Mixing analysis of nitrogen and hydrogen gases for ammonia synthesis via magnetic induction in monolithic channel,” *IOP Conf. Ser. Mater. Sci. Eng.*, vol. 458, p. 12059, 2018, doi: 10.1088/1757-899x/458/1/012059.

[111] W. E. Schiesser and G. W. Griffiths, *A compendium of partial differential equation models : method of lines analysis with Matlab*. Cambridge: Cambridge University Press, 2009.

[112] D. M. Fontes Lima and M. Zaiat, “The influence of the degree of back-mixing on hydrogen production in an anaerobic fixed-bed reactor,” *Int. J. Hydrogen Energy*, vol. 37, no. 12, pp. 9630–9635, 2012, doi: 10.1016/j.ijhydene.2012.03.097.

[113] H. Zhu, X. Gu, K. Yao, L. Gao, and J. Chen, “Large-Scale Synthesis of $MgCl_2 \cdot 6NH_3$ as an Ammonia Storage Material,” *Ind. Eng. Chem. Res.*, vol. 48, no. 11, pp. 5317–5320, Jun. 2009, doi: 10.1021/ie900177q.

[114] M. S. Huberty, A. L. Wagner, A. McCormick, and E. Cussler, “Ammonia absorption at haber process conditions,” *AIChE J.*, vol. 58, no. 11, pp. 3526–3532, Nov. 2012, doi: 10.1002/aic.13744.

[115] G. F. Froment, K. B. Bischoff, and J. De Wilde, *Chemical Reactor Analysis and Design*. 2011.

[116] D. C. Dyson and J. M. Simon, “A kinetic expression with diffusion correction for ammonia synthesis on industrial catalyst.,” *Ind. Eng. Chem. Fundam.*, vol. 7, no. 4, pp. 605–610, 1968, doi: 10.1021/i160028a013.

[117] L. J. Gillespie and J. A. Beattie, “The Thermodynamic Treatment of Chemical Equilibria in Systems Composed of Real Gases. I. An Approximate Equation for the Mass Action Function Applied to the Existing Data on the Haber Equilibrium,” *Phys. Rev.*, vol. 36, no. 4, pp. 743–753, Aug. 1930, doi: 10.1103/PhysRev.36.743.

[118] Y. Huang and J. H. Seinfeld, “A note on flow behavior in axially-dispersed plug flow reactors with step input of tracer,” *Atmos. Environ. X*, vol. 1, p. 100006, 2019, doi: https://doi.org/10.1016/j.aeaoa.2019.100006.

[119] D. M. Ruthven, *Principles of adsorption and adsorption processes*. New York : Wiley, 1984.

[120] J. D. Seader and E. J. Henley, *Separation process principles*. Wiley, 1998.

[121] H. Littman, R. G. Barile, and A. H. Pulsifer, “Gas-Particle Heat Transfer Coefficients in Packed Beds at Low Reynolds Numbers,” *Ind. Eng. Chem. Fundam.*, vol. 7, no. 4, pp. 554–561, Nov. 1968, doi: 10.1021/i160028a005.

[122] S. Wang, C. Xu, W. Liu, and Z. Liu, “Numerical study on heat transfer performance in packed bed,” *Energies*, vol. 12, no. 3, 2019, doi: 10.3390/en12030414.

[123] E. Glueckauf, “Theory of chromatography,” *J. Chromatogr. Libr.*, vol. 51, pp. A1–A68, 1992, doi: 10.1016/S0301-4770(08)61562-6.

[124] F. A. Zenz and D. F. Othmer, *Fluidization and fluid-particle systems*. New York: Reinhold, 1960.

[125] B. Bitsch, C. Barner-Kowollik, and S. Zhu, “Modeling the effects of reactor backmixing on RAFT polymerization,” *Macromol. React. Eng.*, vol. 5, no. 1, pp. 55–68, 2011, doi: 10.1002/mren.201000034.

[126] B. A. Finlayson, *Introduction to chemical engineering computing*, Second. Hoboken, New Jersey: Wiley, 2014.

[127] B. E. Poling and J. M. Prausnitz, *Properties of Gases and Liquids*, Fifth Edit. New York, Chicago, San Francisco, Athens, London, Madrid, Mexico City, Milan, New Delhi, Singapore, Sydney, Toronto: McGraw-Hill Education, 2001.

[128] M. W. Chase, “NIST-JANAF Themochemical Tables, Fourth Edition,” pp. 1–1951, 1998.

[129] J. R. Welty, *Fundamentals of momentum, heat, and mass transfer*, Fifth Edit. Hoboken, NJ: Wiley, 2008.

[130] M. Malmali, G. Le, J. Hendrickson, J. Prince, A. V McCormick, and E. L. Cussler, “Better Absorbents for Ammonia Separation,” *ACS Sustain. Chem. Eng.*, vol. 6, no. 5, pp. 6536–6546, May 2018, doi: 10.1021/acssuschemeng.7b04684.

[131] H. Rashid, N. Hasan, M. Nor, and M. Iskandar, “Temperature Peak Analysis and Its Effect on Absorption Column for CO_2 Capture Process at Different Operating Conditions,” *Chem. Prod. Process Model.*, vol. 9, Jan. 2014, doi: 10.1515/cppm-2013-0044.

[132] J. M. Modak, “Haber process for ammonia synthesis,” *Resonance*, vol. 16, no. 12, pp. 1159–1167, 2011, doi: 10.1007/s12045-011-0130-0.

[133] Y. Gao, F. J. Muzzio, and M. G. Ierapetritou, “A review of the Residence Time Distribution (RTD) applications in solid unit operations,” *Powder Technol.*, vol. 228, pp. 416–423, 2012, doi: https://doi.org/10.1016/j.powtec.2012.05.060.

[134] R. B. Bird, W. E. Stewart, and E. N. Lightfoot, *Transport phenomena*, 2nd ed. New York : Wiley, 2002.

[135] H. A. Deans and L. Lapidus, “A computational model for predicting and correlating the behavior of fixed‐bed reactors: I. Derivation of model for nonreactive systems,” *AIChE J.*, vol. 6, no. 4, pp. 656–663, 1960, doi: 10.1002/aic.690060428.

[136] H. A. Deans and L. Lapidus, “A computational model for predicting and correlating the behavior of fixed‐bed reactors: II. Extension to chemically reactive systems,” *AIChE J.*, vol. 6, no. 4, pp. 663–668, 1960, doi: 10.1002/aic.690060429.

[137] A. A. Iordanidis, “Mathematical Modeling of Catalytic Fixed Bed Reactors,” 2002.

[138] M. L. McGuire and L. Lapidus, “On the stability of a detailed packed‐bed reactor,” *AIChE J.*, vol. 11, no. 1, pp. 85–95, 1965, doi: 10.1002/aic.690110120.

[139] J. W. Vanderveen, D. Luss, and N. R. Amundson, “Stability of adiabatic packed bed reactors. Effect of flow variations and coupling between the particles,” *AIChE J.*, vol. 14, no. 4, pp. 636–643, 1968, doi: 10.1002/aic.690140416.

[140] C. V McSwain and L. D. Durbin, “The Backflow-Cell Model for Continuous Two-Phase Nonlinear Mass-Transfer Operations Including Nonlinear Axial Holdup and Mixing

Effects," *Sep. Sci.*, vol. 1, no. 6, pp. 677–700, Jan. 1966, doi: 10.1080/01496396608049474.

[141] J. T. Baldwin and L. D. Durbin, "The backflow cell model of isothermal first order flow reactors with axial dispersion," *Can. J. Chem. Eng.*, vol. 44, no. 3, pp. 151–157, Jun. 1966, doi: 10.1002/cjce.5450440306.

[142] M. H. Roenier and L. D. Durbin, "Transient response and moments analysis of backflow cell model for flow systems with longitudinal mixing," *Ind. Eng. Chem. Fundam.*, vol. 6, no. 1, pp. 120–129, 1967, doi: 10.1021/i160021a021.

[143] B. R. Dickey and L. D. Durbin, "Continuous and discrete time response analysis of the backflow cell model for linear interphase mass transfer on a distillation plate," *Can. J. Chem. Eng.*, vol. 46, no. 5, pp. 369–376, 1968, doi: 10.1002/cjce.5450460516.

[144] M. G. El-Din and D. Smith, "Development of transient Back Flow Cell Model (BFCM) for bubble columns," *Ozone-Sci. Eng.*, vol. 23, no. 4, pp. 313–326, 2001.

[145] C. Tizaoui and Y. Zhang, "The modelling of ozone mass transfer in static mixers using Back Flow Cell Model," *Chem. Eng. J.*, vol. 162, no. 2, pp. 557–564, 2010, doi: 10.1016/j.cej.2010.05.061.

[146] J. Sinkule, V. Hlaváček, and J. Votruba, "Modeling of chemical reactors-XXXI. The one-phase backflow cell model used for simulation of tubular adiabatic reactors," *Chem. Eng. Sci.*, vol. 31, no. 1, pp. 31–36, 1976, doi: 10.1016/0009-2509(76)85005-1.

[147] C. V. Mcswain and L. D. Durbin, "Extraction and absorption column dynamics and backflow cell model simulation," *Pap n 3-D2*, pp. 201–209, 1971.

[148] J. E. Crosby and L. D. Durbin, "Flow forced backflow cell model of a packed bed gas absorber," *Model Simul Proc Annu Pittsburgh Conf*, vol. 7, no. pt 1, pp. 350–355, 1976.

[149] C. Smith, M. Malmali, C. Y. Liu, A. V McCormick, and E. L. Cussler, “Rates of Ammonia Absorption and Release in Calcium Chloride,” *ACS Sustain. Chem. Eng.*, vol. 6, no. 9, pp. 11827–11835, Sep. 2018, doi: 10.1021/acssuschemeng.8b02108.

[150] K. Wang, Y. Wang, and J. Ma, “Transient numerical simulation of gas-liquid two-phase flow in long distance water supply pipeline,” in *IOP Conference Series: Earth and Environmental Science*, 2020, vol. 510, no. 5, doi: 10.1088/1755-1315/510/5/052042.

[151] L. Diana, A. G. Safitra, D. Ichsani, and S. Nugroho, “CFD Analysis of Airflow Through Prism Obstacles Inside Solar Air Heater Channel,” in *Journal of Physics: Conference Series*, 2020, vol. 1577, no. 1, doi: 10.1088/1742-6596/1577/1/012038.

[152] K. Sato, K. Imamura, Y. Kawano, S. Miyahara, T. Yamamoto, S. Matsumura, and K. Nagaoka, “A low-crystalline ruthenium nano-layer supported on praseodymium oxide as an active catalyst for ammonia synthesis,” *Chem. Sci.*, vol. 8, no. 1, pp. 674–679, Jan. 2017, doi: 10.1039/c6sc02382g.

[153] J. Blazek, *Computational fluid dynamics : principles and applications*, Third. Kidlington, Oxford: Butterworth-Heinemann, 2015.

[154] M. W. Chase and Jr., “NIST-JANAF Themochemical Tables.” J. Phys. Chem. Ref. Data, Monograph 9, 1998.

[155] “Engineering Toolbox.” [Online]. Available: https://www.engineeringtoolbox.com.

[156] K. Aika, M. Kumasaka, T. Oma, O. Kato, H. Matsuda, N. Watanabe, K. Yamazaki, A. Ozaki, and T. Onishi, “Support and promoter effect of ruthenium catalyst. III. Kinetics of ammonia synthesis over various Ru catalysts,” *Appl. Catal.*, vol. 28, no. C, pp. 57–68, 1986, doi: 10.1016/S0166-9834(00)82492-6.

[157] P. R. Holzman, W. K. Shiflett, and J. A. Dumesic, “The importance of ammonia pressure in the kinetics of ammonia synthesis over supported Ru,” *J. Catal.*, vol. 62, no. 1, pp. 167–172, 1980, doi: 10.1016/0021-9517(80)90433-9.

[158] K. I. Aika and A. Ozaki, “Kinetics and isotope effect of ammonia synthesis over ruthenium,” *J. Catal.*, vol. 16, no. 1, pp. 97–101, 1970, doi: 10.1016/0021-9517(70)90200-9.

[159] F. Rosowski, A. Hornung, O. Hinrichsen, D. Herein, M. Muhler, and G. Ertl, “Ruthenium catalysts for ammonia synthesis at high pressures: Preparation, characterization, and power-law kinetics,” *Appl. Catal. A Gen.*, vol. 151, no. 2, pp. 443–460, 1997, doi: 10.1016/S0926-860X(96)00304-3.

[160] I. Rossetti, N. Pernicone, F. Ferrero, and L. Forni, “Kinetic Study of Ammonia Synthesis on a Promoted Ru/C Catalyst,” *Ind. Eng. Chem. Res.*, vol. 45, no. 12, pp. 4150–4155, Jun. 2006, doi: 10.1021/ie051398g.

[161] T. Aoki, H. Miyaoka, H. Inokawa, T. Ichikawa, and Y. Kojima, “Activation on Ammonia Absorbing Reaction for Magnesium Chloride,” *J. Phys. Chem. C*, vol. 119, no. 47, pp. 26296–26302, 2015, doi: 10.1021/acs.jpcc.5b07965.

[162] M. Kitano, Y. Inoue, M. Sasase, K. Kishida, Y. Kobayashi, K. Nishiyama, T. Tada, S. Kawamura, T. Yokoyama, M. Hara, and H. Hosono, “Self-organized Ruthenium–Barium Core–Shell Nanoparticles on a Mesoporous Calcium Amide Matrix for Efficient Low-Temperature Ammonia Synthesis,” *Angew. Chemie Int. Ed.*, vol. 57, no. 10, pp. 2648–2652, Mar. 2018, doi: 10.1002/anie.201712398.

[163] H. Zhu, X. Gu, K. Yao, L. Gao, and J. Chen, “Large-Scale Synthesis of $MgCl_2 \cdot 6NH_3$ as an Ammonia Storage Material,” pp. 5317–5320, 2009.

[164] S. A. Hedayat Mofidi and K. S. Udell, “Study of Heat and Mass Transfer in $MgCl_2/NH_3$ Thermo-Chemical Batteries.” 2016, doi: 10.1115/ES2016-59099.

[165] “Haber process.” [Online]. Available: https://en.wikipedia.org/wiki/Haber_process#/media/File:Ammoniakreaktor_MS.svg.

[166] Y. Li and W. Shen, “Morphology-dependent nanocatalysts: Rod-shaped oxides,” *Chem. Soc. Rev.*, vol. 43, no. 5, pp. 1543–1574, 2014, doi: 10.1039/C3CS60296F.

[167] F. Liao, Y. Huang, J. Ge, W. Zheng, K. Tedsree, P. Collier, X. Hong and S. C. Tsang, “Morphology-Dependent Interactions of ZnO with Cu Nanoparticles at the Materials’ Interface in Selective Hydrogenation of CO_2 to CH_3OH,” *Angew. Chemie Int. Ed.*, vol. 50, no. 9, pp. 2162–2165, Feb. 2011, doi: 10.1002/anie.201007108.

[168] Z. Liuming, L. Jianxin, N. Jun, L. Bingyu, W. Rong, and W. Kemei, “Preparation Methods of Ruthenium Catalysts for Ammonia Synthesis,” *Prog. Chem.*, vol. 23, no. 11, pp. 2225–2232, Nov. 2011.

[169] Y. K. Peng, L. Ye, J. Qu, L. Zhang, Y. Fu, I. F. Teixeira, I. J. McPherson, H. He, and S. C. Tsang, “Trimethylphosphine-Assisted Surface Fingerprinting of Metal Oxide Nanoparticle by ^{31}P Solid-State NMR: A Zinc Oxide Case Study,” *J. Am. Chem. Soc.*, vol. 138, no. 7, pp. 2225–2234, Feb. 2016, doi: 10.1021/jacs.5b12080.

[170] X. Xie, Y. Li, Z.-Q. Liu, M. Haruta, and W. Shen, “Low-temperature oxidation of CO catalysed by Co_3O_4 nanorods,” *Nature*, vol. 458, p. 746, Apr. 2009.

[171] Y. Li, Y. K. Peng, L. Hu, J. Zheng, D. Prabhakaran, S. Wu, T. J. Puchtler, M. Li, K. Y. Wong, R. A. Taylor, and S. C. Tsang, “Photocatalytic water splitting by N-TiO_2 on MgO (111) with exceptional quantum efficiencies at elevated temperatures,” *Nat. Commun.*, vol. 10, no. 1, p. 4421, 2019, doi: 10.1038/s41467-019-12385-1.

[172] J. Y. Ying and T. Sun, “Research needs assessment on nanostructured catalysts,” *J. Electroceramics*, vol. 1, no. 3, pp. 219–238, Nov. 1997, doi: 10.1023/A:1009931726749.

[173] V. G. Komvokis, M. Marti, A. Delimitis, I. A. Vasalos, and K. S. Triantafyllidis, “Catalytic decomposition of N_2O over highly active supported Ru nanoparticles (<= 3 nm) prepared by chemical reduction with ethylene glycol,” *Appl. Catal. B-Environmental*, vol. 103, no. 1–2, pp. 62–71, Mar. 2011, doi: 10.1016/j.apcatb.2011.01.009.

[174] “Role of Bragg's Law in X-Ray Diffraction Studies.” [Online]. Available: http://xrd.co/role-braggs-law-x-ray-diffraction-studies/.

[175] “An Introduction to Electron Microscopy The Scanning Transmission Electron Microscope,” *2019*. [Online]. Available: https://www.fei.com/introduction-to-electron-microscopy/stem/#gsc.tab=0.

[176] L. Chen, P. Bai, H. Fan, W. Yu, H. Guo, and W. Li, “Morphology and structure of nano MgO prepared by a novel nitrogen-protective pressurization method,” *RSC Adv.*, vol. 5, no. 56, pp. 44778–44782, 2015, doi: 10.1039/C5RA02874D.

[177] L. Cui, J. Li, and X. G. Zhang, “Preparation and properties of Co_3O_4 nanorods as supercapacitor material,” *J. Appl. Electrochem.*, vol. 39, no. 10, p. 1871, Sep. 2009, doi: 10.1007/s10800-009-9891-5.

[178] S. Pyshkin, *Optoelectronics - Advanced Device Structures.* S.l.: InTech., 2017.

[179] S. Wu, Y. Peng, T. Chen, J. Mo, A. Large, I. McPherson, H. Chou, I. Wilkinson, F. Venturini, D. Grinter, P. F. Escorihuela, G. Held, and S. C. Tsang, “Removal of Hydrogen Poisoning by Electrostatically Polar MgO Support for Low-Pressure NH_3 Synthesis at a High Rate over the Ru Catalyst,” *ACS Catal.*, vol. 10, no. 10, pp. 5614–5622, May 2020, doi: 10.1021/acscatal.0c00954.

[180] M. Malmali, Y. Wei, A. McCormick, and E. L. Cussler, “Ammonia Synthesis at Reduced Pressure via Reactive Separation,” *Ind. Eng. Chem. Res.*, vol. 55, no. 33, pp. 8922–8932, 2016, doi: 10.1021/acs.iecr.6b01880.

[181] H. H. Himstedt, M. S. Huberty, A. V. McCormick, L. D. Schmidt, and E. L. Cussler, “Ammonia Synthesis Enhanced by Magnesium Chloride Absorption,” *AIChE J.*, vol. 61, pp. 1364, 2015, doi: 10.1002/aic.

[182] R. Z. Sørensen, J. S. Hummelshøj, A. Klerke, J. B. Reves, T. Vegge, J. K. Nørskov, and C. H. Christensen, “Indirect, Reversible High-Density Hydrogen Storage in Compact Metal Ammine Salts,” *J. Am. Chem. Soc.*, vol. 130, no. 27, pp. 8660–8668, Jul. 2008, doi: 10.1021/ja076762c.

[183] Q. Huang, G. Lu, J. Wang, and J. Yu, “Thermal decomposition mechanisms of $MgCl_2 \cdot 6H_2O$ and $MgCl_2 \cdot H_2O$,” *J. Anal. Appl. Pyrolysis*, vol. 91, no. 1, pp. 159–164, 2011, doi: https://doi.org/10.1016/j.jaap.2011.02.005.